From Strong Field Ionization to the Generation of Attosecond Laser Pulses

ISBN-10 90-77209-11-5
ISBN-13 978-90-77209-11-0

Typesetting MiKTEX, WinShell for LATEX
Printing PrintPartners Ipskamp B.V., the Netherlands

From Strong Field Ionization to the Generation of Attosecond Laser Pulses

EEN WETENSCHAPPELIJKE PROEVE OP HET GEBIED VAN
DE NATUURWETENSCHAPPEN, WISKUNDE EN INFORMATICA

PROEFSCHRIFT

ter verkrijging van de graad van doctor
aan de Radboud Universiteit Nijmegen
op gezag van de Rector Magnificus prof. dr. C.W.P.M.Blom,
volgens besluit van het College van Decanen
in het openbaar te verdedigen op maandag 30 oktober 2006
des namiddags om 1.30 uur precies
door

Yongfeng Ni

geboren in 1976

te Jingjiang, Jiangsu, China

Promotor:	Prof. dr. M.J.J. Vrakking(FOM-AMOLF)
Manuscriptcommissie:	Prof. dr. D.H. Parker Prof. dr. A. L'Huillier(Lund Institute of Technology) Prof. dr. H.G. Muller(FOM-AMOLF)

The work described in this thesis has been performed at:

FOM Institute for Atomic and Molecular Physics
Kruislaan 407
1098 SJ Amsterdam, The Netherlands
www.amolf.nl

FOM Institute for Plasma Physics
Edisonbaan 14
3439 MN Nieuwegein, The Netherlands
www.rijnhuizen.nl

Department of Physics, Lund Institute of Technology
Professorsgatan 1
S-223 62 Lund, Sweden
www-atom.fysik.lth.se

Max-Planck-Institut für Quantenoptik
Hans-Kopfermann-Str. 1
D-85748 Garching, Germany
www.mpq.mpg.de

This work is part of the research program of the "Stichting voor Fundamenteel Onderzoek der Materie (FOM)", which is financially supported by the "Nederlandse organisatie voor Wetenschappelijk Onderzoek (NWO)". It has been partially supported by the Marie Curie Research Training Network XTRA(MRTN-CT-2003-505138) within the 6th European Community Framework Programme.

To my parents
and Qun

This thesis is partially based on the work described in the following publications

Control of Atomic Ionization by Two-Color Few-Cycle Pulses
S. Zamith, Y. Ni, A. Gürtler, L.D. Noordam, H.G. Muller, and M.J.J. Vrakking
Optics Letters **29**, 2303, 2004 (Chapter 3)

Above-Threshold Ionization in a Strong DC Electric Field
Y. Ni, S. Zamith, F. Lépine, T. Martchenko, M. Kling, O. Ghafür, H.G. Muller, G. Berden, F. Robicheaux and M.J.J. Vrakking
To be submitted to Physical Review Letters, 2006 (Chapter 4)

Above-Threshold Ionization by Few-Cycle Infrared Laser Pulses
Y. Ni, M. Kling, A.J. Verhoef, J.I. Khan, M. Schultze, F. Krausz, and M.J.J. Vrakking
In preparation, 2006 (Chapter 5)

Attosecond Angle-Resolved Photoelectron Spectroscopy
S.A. Aseyev, Y. Ni, L. J. Frasinski, H.G. Muller, and M.J.J. Vrakking
Physical Review Letters **91**, 223902, 2003 (Chapter 6)

Characterization of Attosecond Laser Pulses Using Angle-Resolved Photoelectron Spectroscopy
S.A. Aseyev, Y. Ni, L.J. Fransinski, H.G. Muller, and M.J.J.Vrakking
Proceedings of international conference on Ultrafast Optics IV edited by F. Krausz, G. Korn, P. Corkum, and I. Walmsley, p293, Springer, New York, 2004 (Chapter 6)

Attosecond Electron Wave Packet Interferometry
T. Remetter, P. Johnsson, J. Mauritsson, K. Varjú, Y. Ni, F. Lépine, E. Gustafsson, M. Kling, J. Khan, R. López-Martens, K.J. Schafer, M.J.J. Vrakking, and A. L'Huillier
Nature Physics **2**, 323, 2006 (Chapter 7)

Angularly Resolved Electron Wave Packet Interferences
K. Varjú, P. Johnsson, J. Mauritsson, T. Remetter, T. Ruchon, Y. Ni, F. Lépine, M. Kling, J. Khan, K.J. Schafer, M.J.J. Vrakking, and A. L'Huillier
J. Phys. B: At. Mol. Opt. Phys. **39**, 3983, 2006 (Chapter 7)

Publications to which the author also contributed but not discussed in this thesis

Control of the Production of Highly Charged Ions in Femtosecond-Laser Cluster Fragmentation
S. Zamith, Y. Ni, S.A. Aseyev, E. Springate, and M.J.J. Vrakking
Proceedings of VIth international conference on femtochemistry and femtobiology edited by M. Martin and J.T. Hynes, p119, Elsevier, 2004

Control of the Production of Highly Charged Ions in Femtosecond-Laser Cluster Fragmentation
S. Zamith, T. Martchenko, Y. Ni, S.A. Aseyev, H.G. Muller, and M.J.J. Vrakking
Physical Review A **70**, 011201(R), 2004

Response of Polyatomic Molecules to Ultrastrong Laser- and Ion-Induced Fields
T. Schlathölter, R. Hoekstra, S. Zamith, Y. Ni, H.G. Muller, and M.J.J. Vrakking
Physical Review Letters **94**, 233001, 2005

Experimental Study of Photodetachment in a Strong Laser Field of Circular Polarization
Boris Bergues, Yongfeng Ni, Hanspeter Helm, and Igor Yu. Kiyan
Physical Review Letters **95**, 263002, 2005

Sub-femtosecond Control of Electron Localization in Molecular Dissociation
M.F. Kling, Ch. Siedschlag, A.J. Verhoef, J.I. Khan, M. Schultze, Th. Uphues, Y. Ni, M. Uiberacker, M. Drescher, F. Krausz, and M.J.J. Vrakking
Science **312**, 246, 2006

Short XUV Pulses to Characterize Field-free Molecular Alignment
F. Lépine, M. Kling, Y. Ni, J. Khan, O. Ghafür, T. Martchenko, E. Gustafsson, P. Johnsson, K. Varjú, T. Remetter, A. L'Huillier and M.J.J. Vrakking
Accepted, J. Modern Optics, 2006

Contents

Preface

Light is everywhere around us. The majority of human information is obtained through vision, where light acts as the carrier of the information. Coherent light sources like the laser[1] play a vital role in acquiring, recording, propagating, saving and presenting information in our everyday life.

For scientists, ultrashort pulse pump-probe laser spectroscopy has enabled studies of fast events like nuclear motion inside a small molecule, such as the dissociation of a water molecule, which occurs at a time scale of about 10 femtoseconds[2]. Electrons play a fundamental role in many physical and chemical processes. Thus it is very important to study electron motion. However, electrons move a hundred or a thousand times faster than nuclei. Pulses shorter than a femtosecond, i.e. attosecond[3] pulses are needed to probe the motion of electrons.

Light not only carries information but also energy. Ultrashort laser pulses not only offer scientists a fast shutter, but also act as powerful energy sources by concentrating energy in a very short time interval. The unprecedented evolution of intense ultrashort laser technology during the last decade, described in Chapter 2, has pushed the achievable laser intensity to a level where electrons can easily be removed from atoms or molecules. The electrons can be freed by absorbing large number of low-frequency photons from the laser field in a process called multi-photon ionization, which is a departure from Einstein's well-known photoelectric effect, where one photon frees exactly one electron. In intense field multi-photon ionization, atoms commonly absorb more photons, and hence, more energy, than the minimum required to reach the ionization threshold, in a process called above-threshold ionization.

Atoms not only absorb multiple photons to free electrons, they can also convert the energy contained in the low energy photons into a single high energy photon in a process called high-order harmonic generation. Attosecond laser

[1] LASER-Light Amplification by Stimulated Emission of Radiation

[2] $1 femtosecond = 1 \times 10^{-15} second$

[3] $1 attosecond = 1 \times 10^{-18} second$

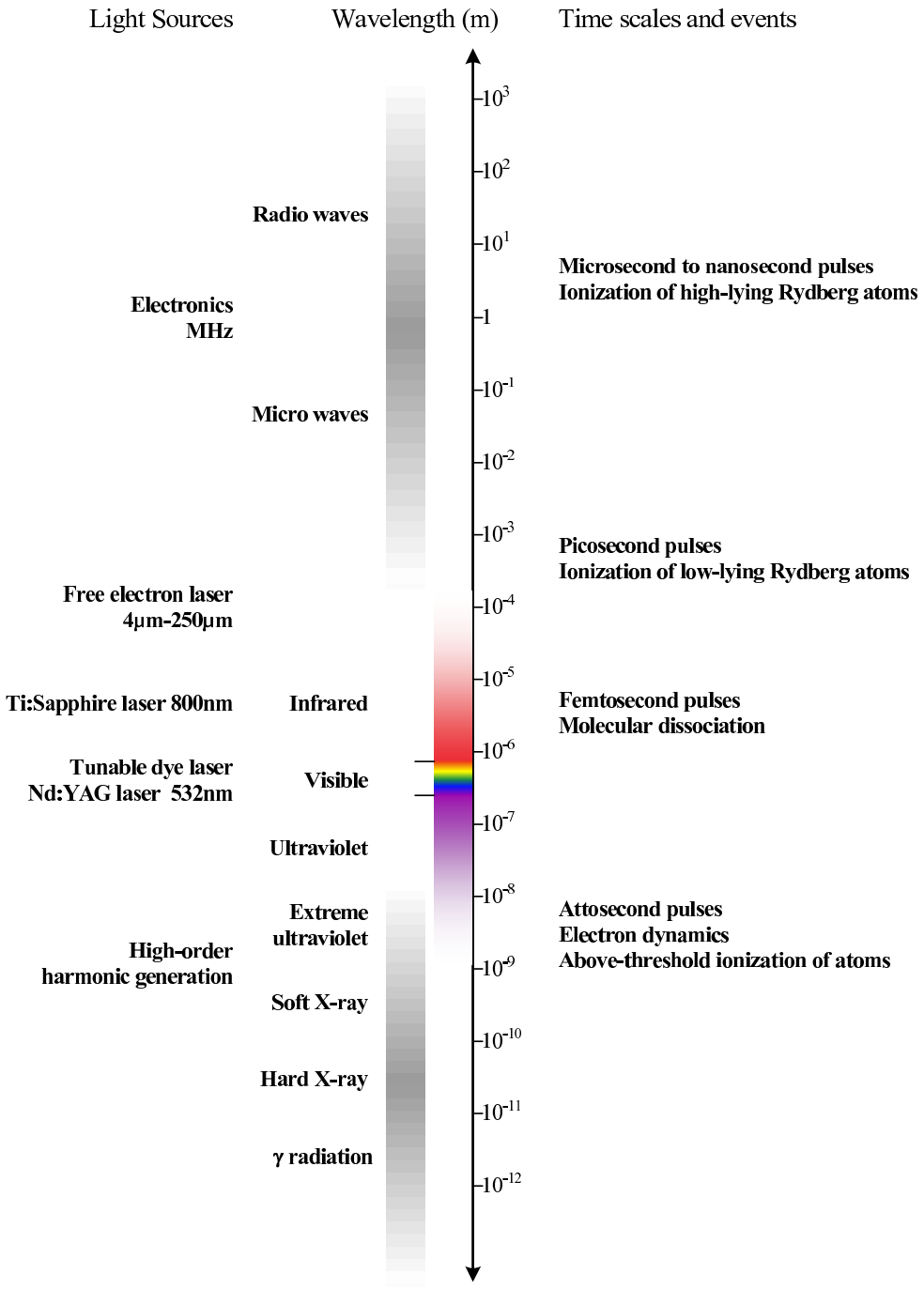

Figure 1: Schematic electromagnetic spectrum. Different electromagnetic radiation sources range from microwave to extreme-ultraviolet, and support pulses ranging from microseconds to attoseconds. Relevant light sources used and physical phenomena studied in this thesis are shown in the figure.

pulses can be generated through this process. This then in turn allows people to study the electron motions inside atoms or molecules. The physics of high harmonic generation lies at the basis for the generation of attosecond laser pulses, and a general introduction will be given in Chapter 1.

To characterize the generated attosecond laser pulses, a cross-correlation technique between the XUV attosecond laser pulses and the infrared laser pulses that are used for their generation has been developed and implemented in many labs. It is based on the analysis of electrons with specific kinetic energies that require the presence of both the XUV and an infrared laser. However, this technique may encounter problems when one wants to measure a single attosecond laser pulse. We have therefore extended this technique into a 2D scheme by using a velocity mapping electron spectrometer, which allows us to simultaneously measure the kinetic energy distribution and the angular distribution of the ejected photoelectrons. This technique holds the possibility of characterizing single attosecond laser pulses and will be discussed in Chapter 6. In our experiment, we have observed that attosecond laser pulses generated using Xenon as generation medium show a remarkable timing difference compared to Argon and Krypton. The ionization processes in the different rare gases are believed to be responsible for this difference.

Motion of electrons on the time scale of the optical cycle of light is at the basis of high harmonic generation and the production of attosecond laser pulses. At the wavelengths where high-order harmonic generation and attosecond pulse formation experiments are carried out, the very short (just a few femtoseconds) optical cycle of the light makes it difficult to follow the motion of the electron on timescales that are short compared to the optical cycle. In order to gain a better understanding of the ionization process that is crucial in high harmonic generation, we have performed a series of experiments where we have scaled down the physics by using a very low-frequency field (far-infrared to radio-frequency) to ionize Rydberg atoms. Though not yet part of this thesis, these systems allow one to probe sub-cycle electron dynamics with readily available femtosecond or nanosecond laser pulses (See Figure 1 for an overview of the wavelengths and timescales of the light sources used in the experiments covered in this thesis). Chapter 3 and chapter 4 describe experiments performed with radio-frequency and far-infrared fields. In Chapter 3 we have observed that the ionization events critically depend on the carrier-envelope phase and the shape of the field cycle. We have also shown that a two-color many-cycle driving field can generate single attosecond laser pulses. In chapter 4, we present experiments showing that ionization processes can occur in two regimes where the frequency, respectively the field-strength of the laser source are of crucial importance and we show that

electron trajectories play an important role during the ionization process.

As will be discussed in Chapter 1 the processes of high-order harmonic generation and above-threshold ionization are intimately related. In an above-threshold ionization experiment in the infrared wavelength range, we have observed interesting features in the angular distribution of electrons which are ionized with short laser pulses with a duration ranging between 20 femtosecond and 6 femtoseconds. These experiments are presented in chapter 5. Interference between electrons ionized at different times is believed to lead to the observed features. In the same chapter, the dependence of the ionization process on the carrier-envelope phase of few-cycle laser pulses (describing the phase of the oscillation of the electric field of the laser with respect to the envelope of the pulse) will also be discussed.

Having reliably produced attosecond laser pulses, see Chapter 6, we have used them to prepare attosecond electron wavepackets and have performed an electron wavepacket interference experiment which is the topic of chapter 7. With this interferometric method, the initial phase of the electron wave function can be retrieved.

Light has enabled people to understand the macroscopic world where we live since early ages. Much of the knowledge obtained during the past few decades at the atomic and molecular level has also been made possible by light. Light will soon allow us to explore the micro-world inside atoms and molecules.

Part I

Introduction

Chapter 1

The physics behind attosecond laser pulses

Attosecond laser pulses (1 *attosecond* $= 1 \times 10^{-18}$ *second*) are similar to pulses generated by traditional lasers in the sense that they are coherent light pulses. However, their generation mechanism is fundamentally different from traditional lasers where light is amplified in a resonator cavity. Attosecond laser pulses are formed through Fourier synthesis of high-order harmonics resulting from the interaction of atoms with ultrashort intense lasers. To get a deep understanding of attosecond laser pulses, we shall first discuss in this chapter the general physics of light-matter interactions, in particular, the interaction of ultrashort intense laser with atoms, followed by a short review on the current status of the generation and characterization of attosecond laser pulses.

1.1 Intense laser field interactions with atoms

While some people may think that sophisticated modern laser spectroscopy has already answered the fundamental question of how atoms and molecules interact with coherent light, the development of intense ultrashort laser technology has led to the realization that much remains to be learned about light-matter interactions. State-of-the-art laser systems can routinely deliver very short laser pulses with a pulse duration of tens of femtoseconds ($1\ femtosecond = 1\times10^{-15}\ second$) and a peak power at the Terawatt ($1\ terawatt = 1\times10^{12}\ watt$) level. The focused laser intensity can easily exceed the Coulomb electric field that binds electrons to the nuclei. This extremely high intensity has opened a new regime of light-matter interactions, where many unusual phenomena have been discovered [1, 2, 3, 4, 5].

The relationship between the laser intensity I, and the electric field strength E, is given by

$$I = \frac{1}{2}\varepsilon_0 c E^2, \tag{1.1}$$

where ε_0 is the permittivity of free space and c the speed of light. When I is expressed in W/cm^2, and E in V/cm, then $I = 1.33\times10^{-3}E^2$ or $E = 27.4\sqrt{I}$. The Coulomb electric field in a hydrogen atom is about $5\times10^9 V/cm$, corresponding to an equivalent intensity of $3.51\times10^{16}W/cm^2$. In the following subsections, several strong field processes in atoms and molecules at moderate intensity ($10^{12}\sim10^{14}W/cm^2$) will be summarized.

1.1.1 General multi-photon ionization mechanism

Shortly after the invention of the laser in the $1960s$, multi-photon transitions and multi-photon ionization were studied intensively. Multi-photon ionization (MPI) investigations were pioneered around 1965 by Delone *et al* in Moscow [6] and intensively studied by Mainfray and Manus in Saclay [7]. Atoms can be ionized in a low frequency radiation field, where the photon energy is smaller than the ionization potential, by absorbing multiple photons. The photoelectrons appear with energy

$$E = n\hbar\omega - I_p, \tag{1.2}$$

where n is the minimum number of photons needed to exceed the ionization potential I_p. (see Figure 1.1(a))

Early multi-photon ionization was accurately modelled by lowest-order perturbation theory (LOPT), the n-photon ionization rate being given by $R_n = \sigma_n I^n$, where I is the laser intensity and σ_n is the generalized cross section.

As the laser intensity increases, many other new experimental phenomena have been observed. Among these was the first observation of above-threshold ionization(ATI) in 1979 by Agostini [8] in Saclay, where atoms were ionized by absorbing more photons than the minimum amount necessary for ionization. A series of photoelectron peaks separated by the photon energy appeared in the photoelectron energy spectrum. The energy of these peaks was given by

$$E_s = (n + s)\hbar\omega - I_p, \tag{1.3}$$

where s is called the number of excess or above-threshold photons carried by the electron.

Perturbation theory breaks down for laser intensities above 10^{13} W/cm^2 since the higher-order correction terms become comparable to the nth-order term, which makes the calculation rather difficult and unreliable. At these intensities, the bound states of an atom can be shifted under the influence of the laser field in an oscillatory way. This shift is called the dynamic or AC-Stark shift. The magnitude of the shift depends on the coupling between the atomic states and the laser field, which is larger for weakly bound states. Some states can sweep into resonance. By including higher-order correction terms perturbation theory can still explain, although with difficulties, some of the observed experimental results, when near resonant or (AC-Stark induced) resonant effects have to be taken into account. Calculations in the perturbative regime for above-threshold ionization of Hydrogen have been given by Gontier and Trahin in 1980 [9].

If the laser intensity is very strong, the atomic potential is strongly distorted by the external laser field and a potential barrier is formed, with a local maximum that is called the saddle point (see Figure 1.1(b)). If the frequency of the laser field is low enough, then, within a quasi-stationary approximation, the electron can escape from the atom by tunnelling through the potential barrier. The tunneling ionization rate may be calculated in the framework of the quasi-static strong field approximation. There are two main approaches for the analytic calculation of ionization rates, namely the Keldysh-like theory [10, 11, 12] and the Ammosov-Delone-Krainov(ADK) theory [13]. The Keldysh-like theory underestimates the ionization rates since it neglects the effect of the Coulomb potential, while ADK tunneling theory fits very well with experimental data in the tunneling regime [14].

At even higher laser intensity, the potential barrier is lowered until the ground state is no longer bound. This enables so-called over-the-barrier ionization (see Figure 1.1(c)). The critical field for over-the-barrier ionization is obtained by equating the saddle-point energy induced by the laser field to the electron binding

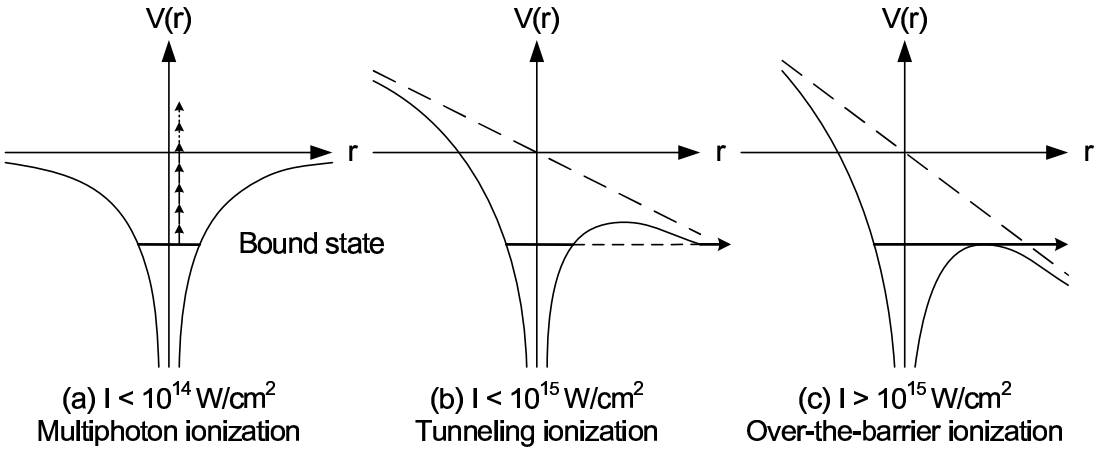

Figure 1.1: Schematic diagram showing different photoionization mechanisms. The atomic potential in the presence of a static electric field is plotted as a function of the distance of the electron from the core. As the laser intensity increases, the atomic potential is distorted, and the dominant ionization process evolves from (a)Multi-photon ionization at low intensity to (b) Tunneling ionization at moderate intensity, and (c) Over-the-barrier ionization at higher intensity.

energy. The corresponding intensity is

$$I_{OTBI}[W/cm^2] = 4 \times 10^9 \frac{(I_P[eV])^4}{Z^2}, \tag{1.4}$$

where Z is the charge state of the relevant atom or ion. For the ground state of hydrogen this occurs at $1.4 \times 10^{14}\ W/cm^2$, while for neutral Xenon, this happens at $8.6 \times 10^{13}\ W/cm^2$.

An adiabaticity parameter γ defined by Keldysh in 1965 is frequently used to distinguish the different ionization processes. It is given by

$$\gamma = \sqrt{\frac{I_p}{2U_p}}, \tag{1.5}$$

where U_p is the cycle-averaged kinetic energy of a free electron oscillating in an ac field of intensity I, given by

$$U_p = \frac{e^2 E^2}{4m\omega^2}, \tag{1.6}$$

where e is the charge of the electron, E the amplitude of the electric field, m the mass of the electron and ω the angular frequency of the laser field. U_p is also called the ponderomotive or quiver energy of the electron. Using practical units, it

becomes $U_p[eV] = 9.33 \times 10^{-14} I[W/cm^2]\lambda^2[\mu m]$. For a low intensity and/or a high frequency laser field where $\gamma > 1$, multi-photon ionization dominates, while for a high intensity and/or a low frequency laser field where $\gamma < 1$, tunneling ionization or over-the-barrier ionization will be most significant. Mevel *et al* [15] have observed the evolution from multi-photon to tunneling ionization experimentally in 1993.

In real experiments, where the ionization rate has to be integrated over the laser pulse time history and the spatial distribution in the interaction region, the target atoms can be depleted before the laser field completely vanishes. This is called saturation of ionization. For a given laser pulse, this saturation happens at a particular intensity, I_{sat}, which is the maximum intensity an atom can withstand. The measured I_{sat} for Xenon atoms driven by a 36 ps pulse in the experiment done by L'Huillier *et al* in 1992 [16] was about 2.5×10^{13} W/cm^2, which is lower than 8.6×10^{13} W/cm^2. This means no Xenon atoms can survive the slow intensity rise to I_{OTBI}. All the target atoms will be ionized well before this by normal multi-photon ionization.

Due to the high nonlinearity of the ionization process, electrons are released within an optical cycle around peaks of the laser field. In the time domain, this means an electron wave packet is produced in a small portion of the laser period where the field reaches a maximum. For the widely used Ti:Sapphire laser operating at 800 nm, the optical period is about 2.7 $femtoseconds$. This implies that the electron wave packet generated by tunneling ionization is so compact that the temporal width can be shorter than 1 $femtosecond$, thus entering a new *attosecond* regime.

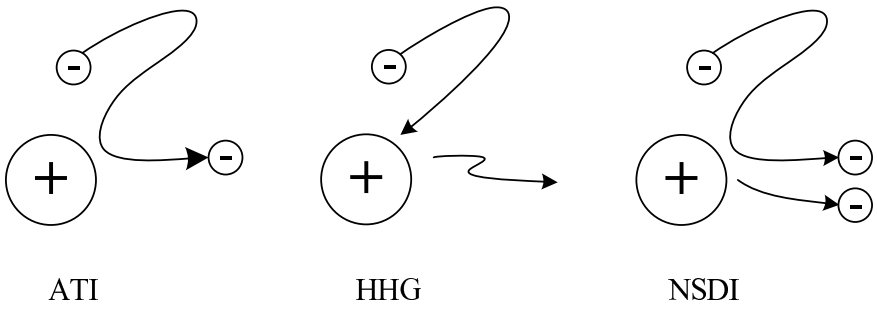

Figure 1.2: Schematic pictures for above-threshold ionization(ATI), high-order harmonic generation(HHG) and non-sequential double ionization(NSDI).

Once ionized by tunneling through the potential barrier, the freed electron acts as a classical point charge in the laser field. The electron is first strongly accelerated away from the ion and after about one half of an optical cycle driven

back when the laser field changes its sign. If the electron returns to the vicinity of its parent ion, it can recombine to the ground state and the energy it carries can be emitted as a high energy photon. This process is often called high-order harmonic generation (HHG), since the photons that are produced in this way are harmonics of the fundamental driving laser filed. The electrons can also be elastically scattered from the ion, by absorbing extra ionizing laser photons, in a process called high-order above-threshold ionization(HATI). They can also be inelastically scattered by transferring part of their energy to another electron, thus promoting this electron to the continuum. This is often called non-sequential double ionization (NSDI) [17, 18, 19, 20]. These three processes are illustrated in Figure 1.2.

This simple re-collision model, developed by Corkum [21], Kulander *et al* and Schafer *et al* [22] in 1993 based on an earlier simple-man's theory first developed by Muller and van Linden van den Heuvell at AMOLF in 1988 [23], not only unifies the three important processes of high-order harmonic generation, high-order above-threshold ionization, and non-sequential double ionization in one framework, but also reveals the importance and the possibility of controlling the electron dynamics on *attosecond* time scales.

In the following subsections, above-threshold ionization and high-order harmonic generation will be discussed in detail, since they form the basis for the understanding of many strong field processes and the generation of attosecond laser pulses.

1.1.2 Above-threshold ionization

As the first characteristic phenomenon in intense laser field interactions with atoms, above-threshold ionization has been intensively studied since its first observation by Agostini *et al* [8] in 1979. The invention of the magnetic-bottle electron spectrometer by Kruit *et al* [24] at AMOLF in 1983 made it possible to measure high resolution spectra at high laser intensities. The disappearance of lower order ATI peaks due to the ponderomotive energy shift of atomic states was first observed by Kruit *et al* [24]. The AC-Stark shift of the ionization potential is roughly given by the ponderomotive energy U_p, since electrons in highly excited states respond to the oscillating laser field in the same way as a free electron.

If the laser pulse is long enough for the electron to leave the laser focus while the laser is still on, then the electron is accelerated by the gradient of the field. The quiver motion is then converted into radial motion away from the focal volume, increasing the kinetic energy by U_p and exactly canceling the energy lost

due to the shift of the ionization potential. The electron energies are then still given by Equation 1.3. However, if the energy shift of the continuum, i.e. U_p, exceeds the photon energy, the lower ATI peaks disappear from the spectrum. No electron is observed with energy less than U_p, and the strongest ATI peak moves to higher order as the intensity increases. This is often called peak shifting or channel closure. A semi-classical calculation [21] indicates that the maximum energy that the electrons can gain from the laser field is $2U_p$, thus the measured electron energy in long laser pulses ranges from U_p to $3U_p$, see Figure 1.3(a).

If the laser pulse is short enough (typically $< 1ps$), the field turns off before the electron can escape from the focal volume. The quiver energy is then returned to the field and the observed electron energy exhibits a shift in the spectrum towards the lower-energy end [25]. The measured electron energy ranges from 0 to $2U_p$, see Figure 1.3(b). The energy shifts have been observed in conjunction with an enhancement in the fine structure of each ATI peak. The appearance of the fine structure has been attributed to the resonant increase in ionization as the atomic levels sweep into resonance (Freeman resonances [26]). These resonances also occur in long pulse experiments but are masked there by the fact that each electron regains its exact energy loss from the field as it escapes the laser pulse.

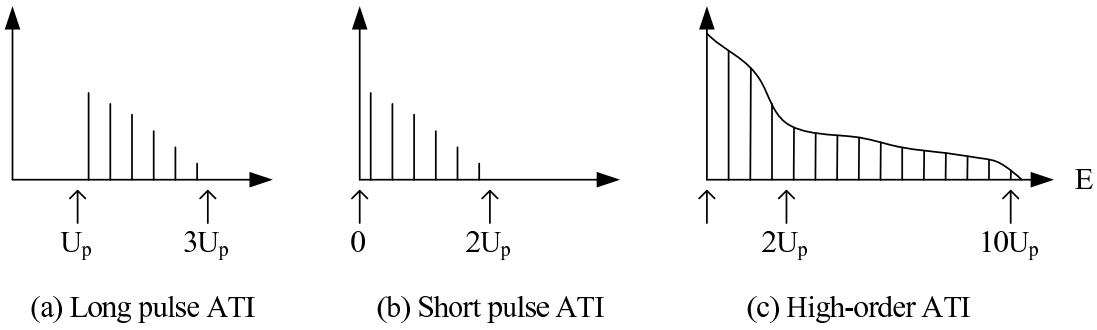

Figure 1.3: Schematic pictures for above-threshold ionization under different conditions. $U_p > \hbar\omega$ is assumed in all cases. In long laser pulses (a) the ATI spectrum ranges between U_p and $3U_p$, whereas in short laser pulses (b) electron energy ranges from 0 to $2U_p$. In high-order ATI re-collision leads to the production of electrons with kinetic energies up to $10U_p$.

A new generation of ATI experiments started in the mid 90's concentrating on the high kinetic energy electrons in the ATI spectrum; these experiments were mainly triggered by the development of high intensity and few-cycle laser pulses [5]. A large plateau extending to about $10U_p$ was observed by Paulus *et al* [27], and scattering rings in the electron angular emission at the edge of the plateau were observed by Yang *et al* [28] and Paulus *et al* [29]. The ATI

plateau and scattering rings are interpreted, in the framework of the re-collision model discussed above, in term of rescattering of the electrons on the parent ions [30, 31]. Van Woerkom *et al* [32] and Muller *et al* [33] both observed resonant-like enhancement and detailed substructure in the plateau region. This was attributed by Muller *et al* [34, 35, 36, 37] to resonances through Rydberg states above the saddle point. Becker *et al* and Paulus *et al* attributed the ATI plateau and the fine structures to constructive and destructive interference of different electron trajectories [38, 39, 40]. The exact mechanism is still under debate. Above-threshold ionization by few-cycle pulses has recently been performed by Grasbon *et al* [41].

In part II of this thesis, we will discuss above-threshold ionization experiments done with a radio frequency field (Chapter 3), a far infrared field (Chapter 4) and a few-cycle infrared laser field (Chapter 5). These studies will help to achieve a deep understanding of the atomic photoionization process in strong fields, and will be helpful to improve the high-harmonic generation and the attosecond laser pulse generation.

1.1.3 High-order harmonic generation

High-order harmonic generation by atoms in intense laser fields has drawn considerable attention since the end of the 80's. When an intense laser pulse interacts with an atomic gas, the atoms respond in a nonlinear way, emitting coherent radiation at frequencies that are integral multiples of the laser frequency. Due to the inversion symmetry of the atom, only odd harmonics of the fundamental are emitted. The total harmonic signal results from coherently adding contributions from different atoms feeling different laser intensities and phases. Only harmonics that can fulfill a phase-matching condition survive through constructive interference. Generally, the harmonic strengths fall off for the first few orders, followed by a broad plateau of nearly constant amplitude, and then a rather sharp cut-off(see Figure 1.4). Semi-classical calculations give a maximum returning kinetic energy of the electron of $3.17U_p$. This energy occurs for electrons that are ionized at a phase of 17^o or 197^o with respect to the maximum of the envelope of the laser field. Thus, the highest energy which can be radiated as a harmonic is $I_p + 3.17U_p$. The spatial beam profile of the harmonics depends on the focusing geometry and how phase-matching condition is realized [42, 43].

Prior to the development of high-harmonic generation, the principal source of (in)coherent X-rays had been synchrotron radiation produced by an accelerator. But such accelerator facilities are typically very expensive, and for cost-effective operation the facilities must be shared by many researchers. High-order harmonic

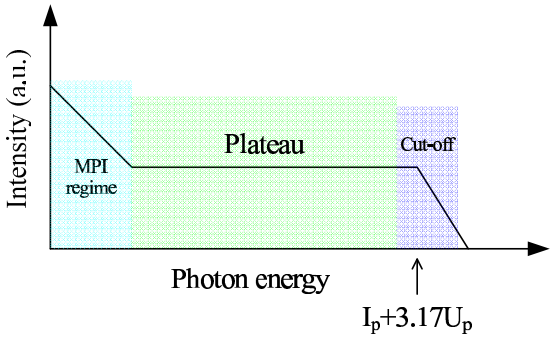

Figure 1.4: Schematic picture of a typical harmonic spectrum. At relatively low laser intensity, harmonics are generated through multi-photon excitation/ionization and their strengths fall off rapidly. At higher laser intensity, plateau and cut-off harmonics are generated through tunnelling ionization or over-the-barrier ionization followed by recollision with the parent ion. Harmonics in the plateau and cut-off region are referred to as high-order harmonics.

generation provides a source of bright, ultra-short, coherent radiation in the extreme ultraviolet (XUV/EUV) and soft X-ray regime [44, 45, 46] with a table-top device. However, the low efficiency of the high-harmonic generation process has thus far limited the applications of harmonic sources.

A lot of efforts have been devoted to increasing the conversion efficiency from the driver laser to the harmonics, and to shortening the wavelength towards the water window where coherent ultrashort x-ray pulses may find very important applications in biology. By changing the interaction length, gas density and spatial profile of the pump beam, the conversion efficiency and quality of high harmonic radiation has been greatly increased [47]. Kazamias *et al* [48] systematically studied high-order harmonic generation with a laser beam truncated by an iris (as opposed to a standard Gaussian profile); harmonic efficiencies as a function of aperture size show a characteristic peaked shape independent of gas species and harmonic order. Nisoli *et al* [49, 50] showed that the use of a truncated zero-order Bessel beam can significantly improve the spatial quality of the harmonic beam. A loosely focusing geometry has been used by groups in Saclay [51] and RIKEN [52, 53] to increase the energy of harmonics to the micro joule level(10^{-5} conversion efficiency). By using shorter driving laser pulses and atomic species with a larger ionization potential, harmonics of 4.37nm and 2.7nm have been generated by Krausz *et al* and Chang *et al*, respectively, in 1997. More recently, Krausz *et al* have generated kiloelectronvolt (keV) X-ray radiation by using a few-cycle Terawatt femtosecond laser [54, 55].

The group of Kapteyn and Murnane has intensively studied phase-matched high-order harmonic generation in hollow waveguides [56, 57, 58] and quasi-phase-matched harmonic generation in modulated hollow waveguides [59, 60]. Both conversion efficiency (by a factor of 10^3) and harmonic cut-off (up to $4.4nm$) are reported to be significantly increased. Kazamias *et al* [61] have shown that harmonic generation in freely propagating and guided-wave geometries becomes equivalent in the long focusing limit. Both techniques rely on the partial ionization of the gas and the geometrical configuration to fulfill phase-matching conditions. Constant *et al* [62] studied high-order harmonic generation in the general case of an absorbing and dispersive atomic gas media. They found that for ultrashort laser pulses, the harmonic conversion efficiency tends to a limit that is mainly imposed by harmonic re-absorption in the gas. This limit, independent of the gas density, is the same for both the case of a loosely focused beam or a beam guided in a gas-filled hollow-core fiber. Under optimum conditions, they measured the highest conversion efficiency to date (4×10^{-5}) for the $15th$ harmonic generated in Xenon using a $40fs, 1.5mJ, 800nm$ pulse at a $1kHz$ repetition rate.

Evolutionary algorithms have been used to optimize harmonic generation. The mechanism relies on carefully tailoring the temporal shape of the driving laser pulse [63, 64, 65, 66], thus controlling the electron dynamics in the strong laser field on *attosecond* time scales. Kapteyn and Murnane [63] have shown that by using a deformable mirror and an adaptive optimization algorithm the efficiency of x-ray generation can be improved by an order of magnitude in hollow waveguides. However, a similar optimization hasn't been successfully done when a gas jet is used for the harmonic generation.

High-order harmonic generation has also been done with lasers operating at long wavelengths. Sheehy *et al* [67] reported high harmonic generation in alkali metal vapors using a mid-infrared(3–$4\mu m$) pump laser. This enables high-order harmonic generation in the visible or near ultra-violet wavelength range, which makes full characterization of the harmonics relatively easy. Using the fact that the ponderomotive energy scales with the inverse of the square of the photon frequency, Shan *et al* [68, 69] reported an efficient extension of the high-order harmonic cut-off generated in rare gases by using a 1.2–$1.5\mu m$ pump laser. The cut-off was extended from 64 to 160eV in Argon. Both experiments were based on nonlinear optical frequency generation, thus making the high-order harmonic generation tunable and allowing new wavelength regions to be explored.

In practice, soft x-ray radiation from high-order harmonic generation has already been used in ultrafast time-resolved X-ray spectroscopy in the gas phase [70] and in sub-micron extreme ultraviolet imaging [71]; it may find further applica-

tions in studies of ultrafast structural dynamics in semiconductors, or surfaces etc., this being areas where x-ray radiation from synchrotron facilities has thus far extensively been used. Ultrafast x-ray microscopy is on the way to real applications in *in vivo* biology, as is EUV lithography.

Another very promising consequence of high-order harmonic generation is the generation of *attosecond* laser pulses, which is the key topic of this thesis. By combining a set of plateau harmonics, sub-femtosecond or attosecond pulses can be generated, which makes it possible to probe and control electron dynamics on attosecond time scale.

1.2 Attosecond laser pulses

Time resolved studies of atomic and molecular processes with femtosecond lasers have provided an enormous wealth of understanding in physics and chemistry. The 1999 Nobel Prize for Chemistry was awarded to Ahmed Zewail for his contributions to femtochemistry. However, fundamental electronic processes which are responsible for atomic ionization, chemical bond formation etc. occur at sub-femtosecond or attosecond time scales. New light sources and suitable time-resolved techniques are therefore required to access this time regime.

The shortest laser pulse generated in a Ti:Sapphire laser is about 3.8 fs from adaptive compression of a cascaded hollow fiber supercontinuum [72], see Chapter 2 subsection 2.1.3 very close to a single optical cycle (2.7 fs) at 800 nm. Since electromagnetic pulses have to extend over at least one complete oscillation cycle to be able to propagate, it is not possible to further shorten the pulse duration at infrared wavelengths. To overcome this limitation and obtain attosecond pulses it is thus necessary to move to a shorter wavelength regime.

At attosecond time scales, essentially all nuclear motions are frozen, which allows people to directly probe the evolution of electron wave functions. This promises tremendous fundamental and practical breakthroughs in atomic physics, chemistry and material science. Such pulses could address important questions about the evolution of complex wave packet states, electron transfer in the condensed phase, and fast electronic processes in solids. The ability to control the motion of electrons, which is the basic component in the structure of any material, allows the possibility of producing new states of matter and new materials. A brand-new field of attosecond science and technology is just emerging.

1.2.1 Generation of attosecond laser pulses

Trains of attosecond laser pulses

The main approach for the generation of sub-femtosecond or attosecond laser pulses is based on a key idea analogous to mode-locked lasers. By coherently superimposing a broad bandwidth of frequencies very short light bursts can be produced in the time domain. This is called Fourier synthesis, and the pulse duration is inversely proportional to the frequency bandwidth. See Figure 1.5 for a schematic illustration.

This approach was first proposed by Farkas and Toth in 1992 [73] and Harris *et al* in 1993 [74] based on high-order harmonic generation by an intense infrared laser. Attosecond pulses can be produced by coherently superposing a broad band of harmonics from the plateau region where all harmonics have nearly equal amplitudes. Antoine *et al* [75] have shown that the harmonics in the plateau region are phase-locked, and the time-dependent single atom emission consists of a train of ultrashort pulses, with two dominant pulses per half cycle, corresponding to the two main electron trajectories giving rise to harmonic emission. The intensity of the total signal emitted by N selected harmonics is

$$I(t) \propto \frac{sin^2(N\omega t)}{sin^2(\omega t)}. \tag{1.7}$$

I(t) is a period function with periodicity $T_L = 2\pi/\omega$, and consists of a series of short light bursts with full width at half maximum

$$\Delta t = \frac{T_L}{2N}, \tag{1.8}$$

where T_L is the optical period of the fundamental laser beam. For an $800nm$ Ti:Sapphire laser, $T_L = 2.7fs$ and $270as$ pulses can be produced by selecting only 5 plateau harmonics. A number of calculations and experiments [44, 76, 77, 78] have shown that the two trajectories, called short trajectory and long trajectory, correspond to different ionizing and returning times, which implies that the high-order harmonic generation happens at a different intensity and thus that the two contributions have a different intensity dependent phase. This phase variation would destroy the attosecond temporal structure. Proper phase-matching through propagating in the generating gas medium and spatial filtering making use of the spatial separation of the high-order harmonics from the two trajectories can serve as a way to select only the short trajectory.

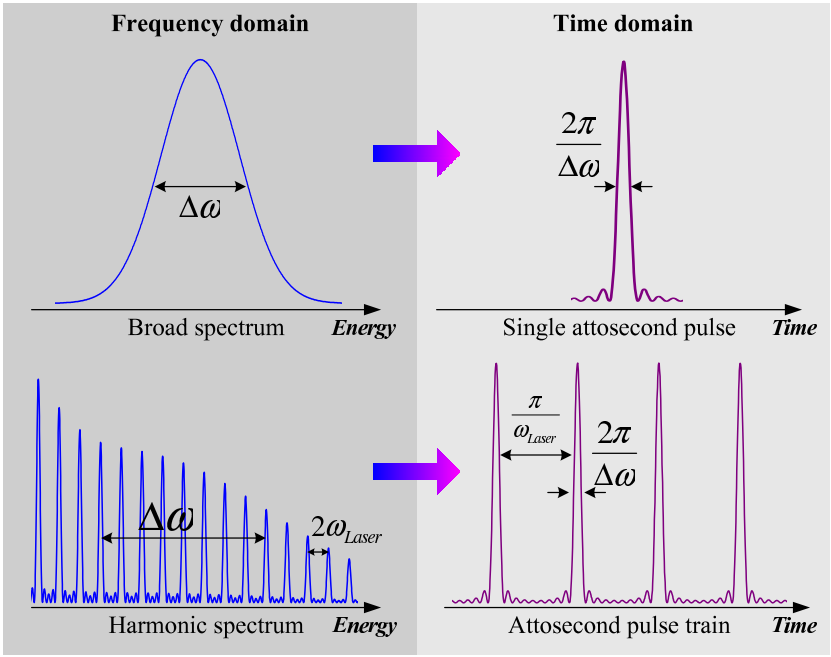

Figure 1.5: Attosecond laser pulse generation in the frequency and time domain. The upper panel schematically presents the principle of the generation of single attosecond laser pulses (right) from a broadband spectrum (shown on the left). The lower panel illustrates the generation of a train of attosecond laser pulses from a selected set of plateau harmonics. The temporal widths of the individual attosecond laser pulses are in both cases inversely proportional to the total frequency bandwidth. Pulses in the attosecond laser pulse train are separated by half of the optical period of the driving laser which is used to generate the harmonics.

Single attosecond laser pulses

In many pump-probe spectroscopic applications, a single attosecond pulse is needed. Making use of the fact that harmonic generation can only occur for linear polarization (since it requires the possibility of an electron-ion recollision) Ivanov *et al* [79] proposed a clever way to generate single attosecond pulses. Using two driving laser fields of controllable circular polarization a laser field with a time-dependent degree of ellipticity can be formed, with a linear polarization within a very short time interval around the temporal maximum of the field. Under this condition the harmonic generation only occurs with one half-cycle, thus producing a single attosecond pulse. This so-called polarization gating technique offers a feasible way of producing single attosecond pulses from relatively

long driving pulses and has been considered in many theoretical calculations and implemented in a number of experiments [80, 81, 82, 83, 84, 85].

Another scheme for generating single attosecond pulse relies on using only the cut-off harmonics and a very short driving laser field [86, 87]. The cut-off region contains harmonics of the highest energy which are generated only near the peak of the laser field. It has a continuous spectrum since it has no harmonic contribution from neighboring cycles, while the plateau harmonics normally contain contributions from different optical cycles. Interference between these contributions gives the discrete harmonic structure. This time-frequency property also guarantees that attosecond pulses formed with cut-off harmonics, where all harmonics are generated within a single half-cycle, have better coherence than those formed with plateau harmonics, where the pulse contains harmonics generated at different time instances. By selecting the cut-off harmonics with a metal filter and using a few-cycle driving laser pulse, single attosecond pulses have been produced [88, 89]. For reliable single attosecond pulse generation, a phase-stabilized few-cycle driving pulse is preferable [90]. Phase-stabilized few-cycle laser pulses will be discussed in detail in Chapter 2.

1.2.2 Characterization of attosecond laser pulses

Due to the extreme short pulse duration and short wavelength, the characterization of attosecond pulses has been a great challenge. Well-established femtosecond metrology techniques can not simply be transferred to the attosecond field due to the lack of nonlinear optical materials in the XUV and soft X-ray range. Although there are field [91] and intensity [92, 93] autocorrelation measurements, they are either not completely straightforward (the former) or of limited use in practice due to the weak intensity of the attosecond light source (the latter).

Most of the current characterization techniques are based on cross-correlation between the attosecond pulse and the fundamental driving laser field. They can be divided into two classes, i.e. characterization of attosecond pulse trains in the perturbative regime and characterization of single attosecond pulses in the framework of the strong field approximation. Both techniques utilize photoionization of atoms by the XUV or soft X-ray light pulse to produce electron wave-packets in the continuum.

Characterization of attosecond laser pulse trains

The weak-field characterization technique for attosecond pulse trains is detailed by Muller in reference [94]. It is often referred to as RABBITT: Reconstruction of

Attosecond harmonic Beating By Interference of Two-photon Transitions. This technique will be discussed in detail in Chapter 7. In essence, it is a two-color XUV+IR photoionization technique where the measured photoelectron spectrum contains peaks corresponding to harmonics and sidebands due to absorption and emission of additional infrared photons. In the low-intensity limit, only the first order process contributes to the sidebands. The intensity variation of the sidebands as a function of the time delay between the harmonic pulses and the infrared pulses contains the information about the phase difference between adjacent harmonics.

The first measurement of attosecond pulse trains was done by Paul *et al* [95] in 2001. They discovered in their experiment that the selected plateau harmonics were indeed phase-locked.Through Frouier synthesis as discussed in the previous pages, a train of 250 *attosecond* pulses was formed in the time domain.

Since then this technique has been extensively used and extended for characterizing attosecond pulse trains in a number of laboratories. Dinu *et al* [96] measured the absolute timing of the attosecond pulse train with respect to the optical cycle of the fundamental laser field. In their measurement the attosecond pulses were found to occur at a delay of $190 \pm 20as$ after the field maxima. Mairesse *et al* [97] found that a linear chirp existed over a wide range of plateau harmonics (which is often called the attochirp), since the generation of different harmonics depends on the time that electrons spend in the laser field before they recollide with their parent ionic core. Lopez-Martens *et al* [98] pointed out that shorter attosecond pulses can be achieved by compensating the positive chirp of the attosecond pulses that are generated with a thin aluminum filter.

Another technique called XUV-FROG [99, 100, 85] has been developed in Lund based on two-color ionization to estimate the harmonic chirp (the variation of the XUV frequency over the length of the attosecond pulse train) by measuring the energy shift of the sidebands as a function of XUV-IR delay.

However, most of these techniques are limited for attosecond laser pulse trains, since the sidebands cannot be distinguished from harmonic peaks for single attosecond pulses that have a very broad bandwidth. At AMOLF, we have extended the RABBITT technique into a 2D scheme [101] where both the kinetic energy and the angular distributions of the photoelectrons is measured. Our results show that the phase information is not only encoded in the sideband intensities but also in the angular distribution of the ejected photoelectrons. As such, this technique holds potential for characterization of single attosecond pulses. This will be discussed in detail in Chapter 6.

Characterization of single attosecond laser pulses

For characterizing single attosecond pulses, a method based on the strong field approximation is often utilized. Consider an electron freed by a single XUV attosecond pulse of central frequency Ω_X in a strong linearly polarized infrared laser field $E_L(t) = E_0(t)cos\phi_i = E_0(t)cos(\omega_L t + \phi)$ of central frequency ω_L and whose initial kinetic energy $W_0 = \hbar\Omega_X - I_p$ fulfills $W_0 \gg U_p \gg \hbar\omega_L$. The final kinetic energy of the electron is given by [102]

$$W_f = W_0 + 2U_p cos2\theta_i sin^2\phi_i \pm \sqrt{8W_0U_p}cos\theta_i sin\phi_i, \tag{1.9}$$

where θ_i is the angle between the final electron velocity and the laser polarization. Drescher *et al* [88] realized that the last term vanishes when measuring only electrons emitted at $\theta = 90^o$. The photoelectron spectrum then oscillates as a function of the initial phase ϕ_i at twice the laser frequency. With this technique, Hentschel *et al* [89] and Kienberger *et al* [103] measured a single soft x-ray pulse of 650 *attoseconds*.

Also based on this strong field approximation approach, XUV-SPIDER has been proposed by Quéré *et al* [104] and by Mauritsson *et al* [105] in 2003 and implemented by Cormier *et al*[106] for complete characterization of attosecond pulse trains and single attosecond pulses in 2005. Attempts trying to unify these two approaches have also been pursued by Mairesse and Quéré [107, 108].

When measuring electrons emitted along the laser polarization and for $W_0 \gg U_p$, the electron wave-packets launched by an XUV attosecond pulse actually follow the oscillation of laser field (Equation 1.9). The measured photoelectron spectra as a function of the initial phase ϕ_i (i.e. the delay between attosecond pulse and the laser field) thus allows to reconstruct the laser field itself. Goulielmakis *et al* [109] have beautifully performed this measurement with a 250 as XUV pulse and a carrier-envelope phase stabilized 5 fs infrared laser pulse.

Chapter 2

Experimental tools for the generation, detection and use of attosecond laser pulses

Due to their very short pulse duration and very high peak power, ultrashort intense lasers have become essential research tools in many laboratories in the fields of physics, chemistry and biology. Attosecond laser pulses are generated through the interaction of atoms with ultrashort intense lasers, more specifically, femtosecond intense lasers($1\ femtosecond = 1 \times 10^{-15}\ second$). A precise knowledge about these femtosecond lasers is a prerequisite for performing many strong-field experiments and generating attosecond laser pulses. We shall discuss the generation, characterization and manipulation of ultrashort/femtosecond intense laser technology in this chapter. A powerful velocity-map imaging setup, which is used to study the electron dynamics in the experiments, will also be discussed in this chapter.

2.1 Ultrashort intense laser technology

Ultrashort laser technology has developed rapidly over the past decade since the first demonstration of Kerr-lens mode-locking in a Ti:Sapphire solid state laser. The application of the chirped pulse amplification(CPA) [110] technique to solid state lasers and the development of techniques for optical pulse compression have made the generation of extremely energetic femtosecond laser pulses possible. Nowadays, femtosecond light sources are turn-key devices in many labs. Pulses as short as 3.8 fs as well as pulses with peak intensity higher than a Petawatt(10^{15} $Watt/cm^2$) [111] have been generated. The extremely short pulse duration has enabled people to study a variety of ultrafast processes. The work on dissociation dynamics of molecules and more complex chemical reaction dynamics was rewarded with a Nobel prize in chemistry for A. H. Zewail in 1999. Pulse shaping techniques further enable people to manipulate and control a lot of physical and chemical processes towards a pre-defined target.

2.1.1 Generation of ultrashort laser pulses

Ultrashort pulses are generated by mode-locked lasers. By combining in phase a number of distinct longitudinal modes of a laser, a short pulse is formed through constructive interference between all the modes, with a characteristic repetitive pulsed nature. Mode-locking can be implemented both actively and passively. Active mode locking uses a modulator in the laser cavity whereas passive schemes use a saturable absorber, often a thin semiconductor film, to lock the relative phases. Modern solid-state mode-locked lasers use a scheme called Kerr-lens mode-locking(KLM).

When a laser beam of sufficient intensity I(r,t) passes through an optical material, the index of refraction of the material can be altered by the intensity of the laser beam:

$$n = n_0 + n_2 I, \tag{2.1}$$

where n_0 is the normal index of refraction, and n_2 is the intensity-dependent nonlinear index. This effect is often referred to as the optical Kerr effect. The nonlinear index of refraction is very small. For example, in fused silica $n_2 \approx 3 \times 10^{-16} cm^2/W$ around 800nm. The optical Kerr effect can induce both transverse(spatial) and longitudinal(temporal) intensity-dependent index modulations.

If we consider a laser beam of Gaussian spatial profile, then the central part of the beam will experience a higher index of refraction than the edge, thus creating a lens which in turn slightly focuses the beam within the material. This is often

called self-focusing (SF). Kerr-lens mode-locking uses the self-focusing effect to preferentially select the pulsed mode-locked set of modes that generate short pulses rather than a single steady-state cw mode. The first Kerr-lens self-mode-locked Ti:Sapphire laser was demonstrated by Sibbett and his group in 1990. It is now routine to generate pulse durations as short as $10fs$ directly from a Ti:Sapphire oscillator by introducing intra-cavity dispersion compensation with chirped mirrors.

If we consider a laser pulse of Gaussian temporal profile, then different parts of the pulse will experience a different index of refraction, thus creating a phase change across the pulse. This is often called self-phase modulation (SPM). SPM can broaden the frequency spectrum. This allows the pulses to be further compressed to a much shorter duration than what could normally be achieved with a mode-locked laser.

Ti:Sapphire (titanium-doped sapphire) is now the most common laser material for the generation of ultrashort pulses. Developed in the mid-1980s, Ti:Sapphire has a very broad gain bandwidth from 700 to $1100nm$ with a peak around $800nm$. It also has a broad absorption bandwidth with a maximum around 500nm, which makes it ideal for frequency-doubled YAG pump lasers. Its extremely good thermal conductivity, high energy storage density approaching $1J/cm^2$ and the long lifetime of the excited state make it very suitable for amplification to very high power.

2.1.2 The AMOLF Terawatt femtosecond laser system

Typical Kerr-lens mode-locked lasers deliver pulse energies of approximately $5-10nJ$ at a repetition rate around $100MHz$. They have been widely used in many fields like optical communication [112], laser micro-machining [113], optical coherence tomography [114] etc. However, for many nonlinear and high-field physics experiments, the megawatt power from the oscillator is not sufficient. Chirped-pulse amplification (CPA) which originated from the work of Strickland and Mourou in 1985 [110] has been progressing into a standard method to achieve a peak power on the order of a Terawatt ($10^{12}W/cm^2$) [115] from a lab-size multi-stage laser system, and even Petawatts ($10^{15}W/cm^2$) [111] from a large-scale laser facility.

The AMOLF Terawatt laser system [116] is also based on the CPA technology. Our Ti:Sapphire oscillator (Kapteyn-Murnane Laboratories L.L.C, Model TS) produces $5nJ$ pulses at a $91MHz$ repetition rate, with a central wavelength of 800nm and a bandwidth of $41nm$ which supports a pulse duration as short as $20fs$.

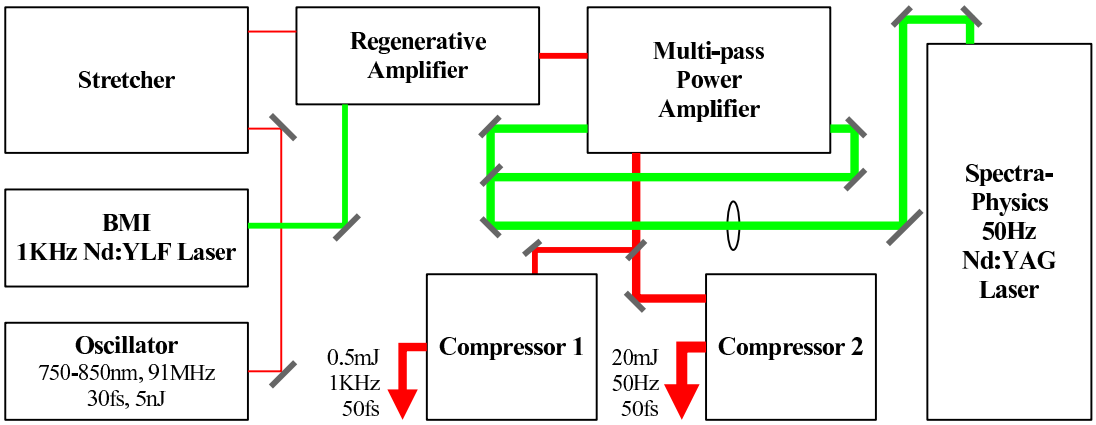

Figure 2.1: The AMOLF Terawatt laser system

These pulses are first stretched to about 400 picoseconds in an all-reflective aberration-free Öffner triplet grating stretcher [117]. The stretcher is designed so that the shorter wavelength (higher frequency) components of the pulse must travel along a longer path than the long-wavelength (low-frequency) components. Pulses emerging from the stretcher thus have low-frequency components in the leading edge and higher frequencies in the trailing edge. This frequency sweep across the pulse is called a 'frequency-chirp'. It is called a positive chirp when the frequency increases as a function of time. Stretching the pulses means that the peak intensity is lowered. This enables the pulses to be amplified to high energies without damaging the amplifiers. The nonlinear phase shift accumulated in the amplifier due to self-phase modulation can be approximated as

$$\phi_{NL} = \frac{2\pi}{\lambda} \int_0^L n_2 I(l,t) dl, \tag{2.2}$$

where the integral runs over all the material encountered by the laser. The value of this expression is also known as the B integral of the amplifier system. As a rule of thumb in the design of high-power laser systems, the B integral must be kept as low as possible. The value that leads to severe damage to the amplifier rod is approximately 3 to 5.

The stretched pulses are amplified in a home-built regenerative amplifier. The regenerative amplifier is pumped by a frequency-doubled $1KHz$ Nd:YLF laser (B.M.Industries) . The typical output from the regenerative amplifier is about 1mJ for a pump power of $11mJ$/pulse and for 11 round-trips inside the cavity. This output is further amplified to $40mJ$ in a 5-pass amplifier, pumped by a $50W$ Nd:YAG laser (Spectra-Physics) operating at $50Hz$.

Amplified pulses are then compressed in a compressor consisting of a pair of parallel gratings. The chirp introduced in the stretcher and during the amplification stages is compensated by adjusting the angular orientation of the grating pairs and the separation between the two gratings. By choosing a different groove density for the gratings in the compressor($1500 lines/mm$) and in the stretcher($1200 lines/mm$), the fourth-order dispersion can be minimized, thus producing shorter pulses with better contrast, which is important in many high-field experiments. After compression we have $20mJ$ in a $50fs$ pulse ($0.4 Terawatt$).

2.1.3 Generation of high power few-cycle laser pulses

Although laser pulses as short as $10fs$ can be routinely generated in many labs, they are limited to low energies(nJ). On the other hand, high-power laser systems using chirped-pulse amplification always suffer from the problem of gain narrowing, which reduces the final spectral bandwidth and typically limits the shortest pulse duration to several tens of femtoseconds after the multiple amplification stages.

Self-phase modulation in single-mode fibers has been used to broaden the spectrum and further compress ultrashort laser pulse down to $5fs$, however, the output energy is limited to tens of nJ due to both material damage and high-order nonlinearities. In 1996, Nisoli *et al* found a new way to broaden the spectrum by propagating the laser pulses through a hollow-core fiber waveguide filled with rare gas [118]. As we discussed in the first subsection, a laser pulse with a Gaussian temporal profile will experience a phase shift

$$\Delta\phi(t) = \frac{2\pi n_2 I(t) L}{\lambda}, \tag{2.3}$$

and thus creates new frequencies with a linear chirp around zero time

$$\Delta\omega(t) = -\frac{d(\Delta\phi(t))}{dt}. \tag{2.4}$$

After compression using chirped mirrors, where different wavelengths penetrate into different depths (thus experiencing different phase changes), $5fs$ pulse with $0.5mJ$ energy can be generated. Recently, the same group also reported the shortest light pulse of $3.8fs$ in the infrared wavelength regime by cascading hollow-core fiber ultra-broadband continuum generation [72]. For many years, hollow-core fiber spectral broadening has been a standard method to get mJ level few-cycle laser pulses. Terawatt few-cycle laser pulses have been generated in the group of Krausz by further amplifying these few-cycle pulses [119].

However, the hollow-core fiber compression technique has some limiting factors. The output energy is limited to about $0.5mJ$, the beam pointing of the incoming laser beam dramatically affects the output laser pulses, and the compression performance critically depends on the quality of the hollow fiber. Optical parametric chirped pulse amplification (OPCPA) technology has been extensively pursued in many labs to overcome these limitations The generation of few-cycle pulses from OPCPA systems remains to be done. Another alternative approach has been introduced by Hauri *et al* in 2004 [120]. In their experiment, optically formed filamentation in a transparent gas tube is used to serve as a self-guiding channel and induce self-phase modulation for spectral broadening. $5.7fs$, $0.38mJ$ pulses with an excellent spatial beam profile have been reported. This technique is believed to hold the potential for generating even shorter pulses up to the single cycle limit.

For a laser pulse $E_L(t) = E_0(t)cos(\omega_L t + \phi_0)$ consisting of many optical cycles, the carrier-envelope phase ϕ_0 does not play measurable role, however, it becomes crucial for few-cycle pulses. This is the case since the laser intensity changes dramatically from cycle to cycle in few-cycle laser pulses, and strong field phenomena are an extremely nonlinear function of laser intensity. Figure 2.3 shows two laser pulses with a different carrier-envelope phase. ϕ_0 has to be taken into account when performing strong field experiments with few-cycle laser pulses. Pioneering experiments [39, 121] by Paulus *et al* have shown that the ratio of ionization parallel and anti-parallel to the electric field depends on the carrier-envelope phase. A new angle-resolved strong field ionization experiment with phase-stabilized few-cycle laser pulses will be discussed in Chapter 5.

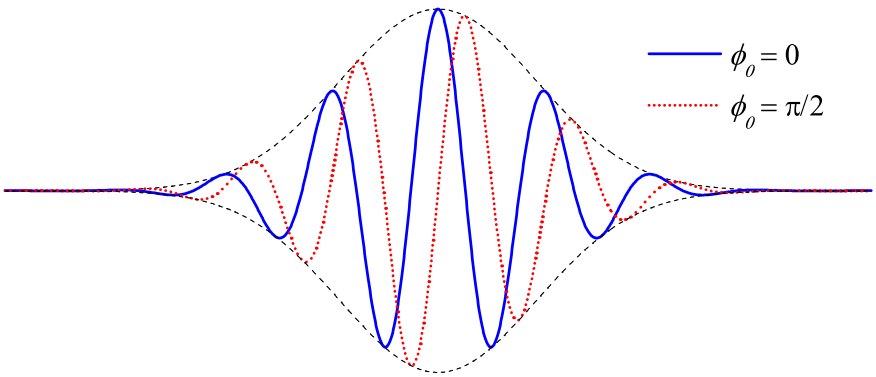

Figure 2.2: Two few-cycle pulses with the same carrier frequency and envelope, but different carrier-envelope phase $\phi_0 = 0$(solid line) and $\phi_0 = \pi/2$(dotted line).

2.1.4 Carrier-envelope phase stabilization

Consider a femtosecond pulse in Kerr-lens mode-locked femtosecond oscillator. Due to the intra-cavity dispersion, the carrier travels at the phase velocity while the envelope travels at the group velocity. This means that the carrier-envelope phase ϕ_0 will evolve while the pulse circulates inside the laser cavity. A phase shift $\Delta\phi_0$ is accumulated every time when the pulse inside the cavity finishes its round trip and finally couples out the laser cavity. In the absence of perturbations to the laser, the carrier-envelope phase ϕ_0 shifts by this fixed amount $\Delta\phi_0$ between successive pulses. In reality, however, without active stabilization $\Delta\phi_0$ slowly changes in a random manner from pulse to pulse due to its sensitivity to perturbations. As a result, ϕ_0 evolves in a manner that can not be predicted over long time intervals.

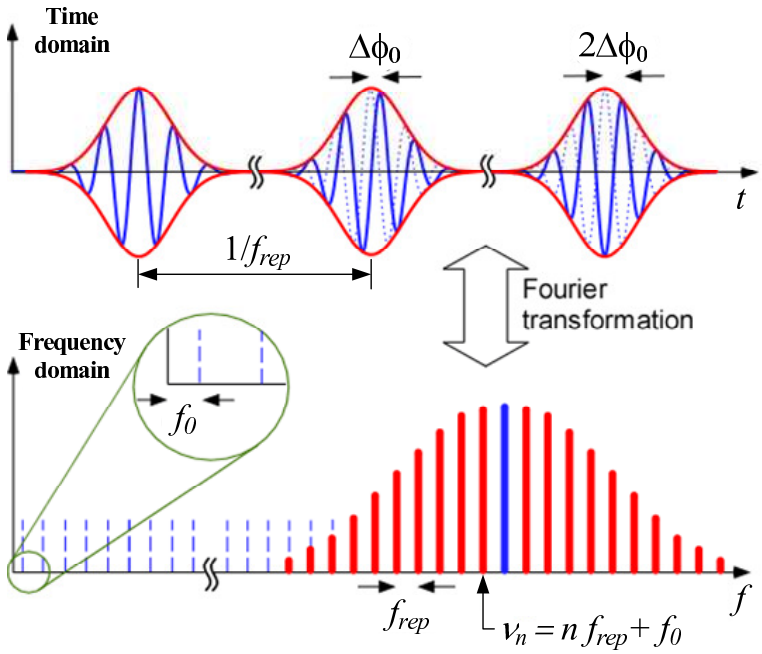

Figure 2.3: Three consecutive pulses of the pulse train emitted by a mode locked laser and the corresponding spectrum. The pulse-to-pulse phase shift $\Delta\phi_0$ results in an offset frequency f_0 [122].

Based on the frequency comb technology [123, 124], which is part of Hansch's work that led to his Nobel prize in Physics in 2005, scientists have been able to stabilize the carrier-envelope phase. The output of a mode-locked femtosecond laser contains a train of identical laser pulses, separated by fixed interval $\tau = 1/f_{req}$. The spectrum contains a comb of regularly spaced frequencies, where the

comb spacing is inversely proportional to time between pulses, i.e., the repetition rate of the laser f_{rep}. Fourier analysis also tells us that a phase shift in time domain corresponds to a shift in the frequency domain. Thus the frequencies of the comb lines can be written as $\nu_n = nf_{rep} + f_0$. The comb offset f_0 is connected to the pulse-to-pulse phase shift $\Delta\phi_0$ by

$$f_0 = \frac{1}{2\pi} f_{rep} \Delta\phi_0. \tag{2.5}$$

Stabilization of the pulse-to-pulse carrier envelope phase slip $\Delta\phi_0$ is thus accomplished if the offset frequency f_0 is locked to an external clock.

The f-to-2f interferometer is one of the most common and simplest way to measure the offset. For this, a broad spectrum over an octave is needed. This spectrum can be easily obtained by using the self-phase modulation effect of the femtosecond laser pulses in a microstructure fiber. The heterodyne beat between the second harmonic of the low frequency end and the high frequency end of the fundamental yields the difference frequency

$$2\nu_n - \nu_{2n} = 2(nf_{rep} + f_0) - (2nf_{rep} + f_0) = f_0. \tag{2.6}$$

A feedback signal is from the interferometer is used to control the dispersion inside the laser cavity in order to stabilize the carrier-envelope phase. This can be done either by rotating the end cavity mirror on which the laser spectrum is dispersed to control the group and phase velocity difference or, empirically, by adjusting the pump power. In amplified laser systems, a second f-to-2f interferometer is used to control the long term drift of the carrier-envelope phase in the amplifier [90].

2.1.5 Characterization of ultrashort laser pulses

There are no electronic devices fast enough to measure femtosecond laser pulses directly, although some streak cameras can resolve picosecond or hundreds of femtosecond temporal events. Most of the measurement techniques are based on the correlation of two beams of femtosecond pulses. In practice, an incoming laser beam $E_L(t) = \Re[E_0(t)e^{i[\omega_L t + \phi(t)]}]$ is split into two. One beam goes through a fixed optical path, and the other through an optical delay line which introduces a time delay τ. Both beams are then recombined and focused onto a nonlinear crystal to produce second-harmonic radiation. The detected second-harmonic intensity as a function of delay is

$$I(\tau) = \int_{-\infty}^{+\infty} |[E_0(t)e^{i[\omega_L t + \phi(t)]} + E_0(t-\tau)e^{i[\omega_L (t-\tau) + \phi(t-\tau)]}]^2|^2 dt. \tag{2.7}$$

Multiplying out the integrand in Equation 2.7, three frequency components can be distinguished that are located around $\omega = 0$, ω_L and $2\omega_L$. If the two beams are recombined non-collinearly, the cross terms with phase information $\phi(t)-\phi(t-\tau)$ disappear due to interference of two beams. Equation 2.7 then reduces to an intensity autocorrelation, which can measure only the pulse duration. If the two beams are recombined collinearly and a high-pass filter is used to select the cross term oscillating at $2\omega_L$, an interferometric autocorrelation can be constructed, which can measure not only the pulse duration but also the chirp. However, it can not tell the sign of the chirp. By measuring the autocorrelation as a function of both time delay and frequency in a noncllinear configuration, the so-called frequency-resolved optical gating(FROG) [125] technique is obtained, that can be used to determine the pulse duration, the chirp and its sign simultaneously. Since FROG uses an iterative algorithm to search for the correct pulse shape, it is sometimes very time-consuming for complex laser pulses.

Based on Fourier transform spectral interferometry, Iaconis and Walmsley [126, 127] proposed a novel self-referencing interferometric technique for complete characterization of femtosecond laser pulses in 1998. Again, a laser beam is split into two replicas with a fixed time delay. These replicas are combined with a chirped pulse in a nonlinear crystal. The chirped pulse is stretched such that each frequency occurs at a different time. Due to the time delay between the replicas, sum-frequency generation with the chirped pulse introduces a frequency shear $\delta\omega$ in the output. The frequency-converted pulse pairs are then sent to a spectrometer, where the recorded interferogram is given by

$$I(\omega) = |E(\omega)|^2+|E(\omega+\delta\omega)|^2+2|E(\omega)E(\omega+\delta\omega)|cos[\phi(\omega+\delta\omega)-\phi(\omega)+\omega\tau]. \quad (2.8)$$

The last term contains the information needed for reconstruction of the pulse. Since it uses a direct Fourier inversion routine to retrieve the phase information, this spectral phase interferometry for direct electric-field reconstruction (SPIDER) technique can perform real-time measurement and has been used to improve high power CPA femtosecond laser systems in many labs. SPIDER is very useful particularly for few-cycle optical pulses. Gallmann *et al* [128] have measured $sub-6fs$ pulses with the SPIDER technique. In our group, a SPIDER setup has also been constructed. As a test we used it to measure the second-order dispersion of a femtosecond laser pulse passing through a $1cm$-thick BK7 plate. A $\phi'' = -500fs^2$ is obtained, which is in good agreement with the calculated value $-452.7fs^2$.

2.1.6 Ultrashort laser pulse shaping

Shaping of ultrashort optical pulses into arbitrarily desired waveforms gives the ability to coherently control many fundamental processes in physics, chemistry, biology and engineering, particularly when it is combined with a learning algorithm to look for a target pulse shape that performs a designed function in a huge search space. Most experimental implementations rely on imposing phase and/or amplitude modulation on the spatially dispersed frequency components of the laser pulse

$$E_{out}(\omega) = E_{in}(\omega)H(\omega)e^{i\phi(\omega)} \tag{2.9}$$

by using a liquid-crystal spatial light modulator (LC-SLM), an acoustic-optical modulator (AOM) or deformable mirrors [129].

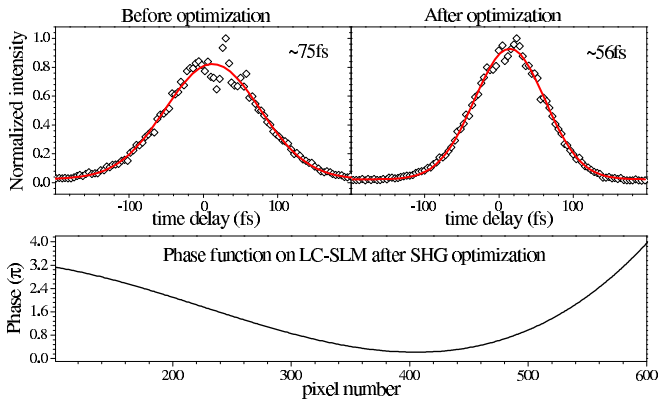

Figure 2.4: Intensity autocorrelation traces of the output from our regenerative amplifier. The upper panel shows measurements before and after optimization. The lower panel shows the phase function accumulated in the liquid crystal pulse shaper after optimization

In our group, a phase-only LC-SLM is used for shaping our femtosecond laser pulses. As a first test, we have used this setup to optimize the properties of our laser system. Figure 2.4 shows the result of an adaptive pulse compression with our pulse shaper using a genetic algorithm and the generation of second harmonic as a learning feedback. The laser pulses coming from our regenerative amplifier contain mainly second-order phase variation and a small third-order term. After the optimization procedure, pulses are compressed from $\sim 75fs$ to $\sim 56fs$. We have also performed experiments on optimization of highly charged ions in femtosecond laser-cluster interactions [130] with our pulse shaping setup. Representative results from this experiment are shown in Figure 2.5

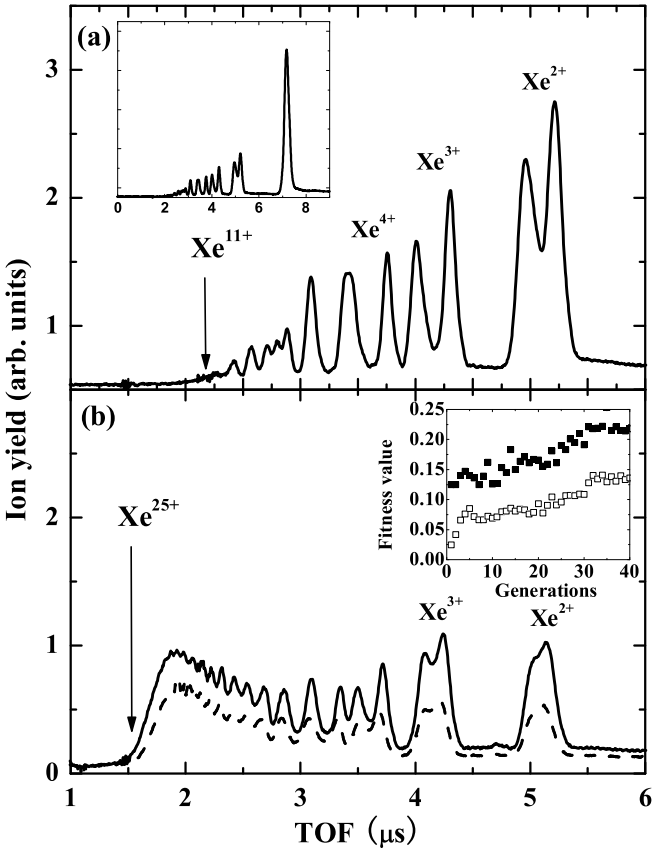

Figure 2.5: Time-of-flight (TOF) traces for the interaction of Xenon clusters ($N_{avg} \approx 1.6 \times 10^4$) (a) with a Fourier-transform-limited $100fs$, $800nm$, $10^{15}W/cm^2$ laser pulse (The inset shows the complete TOF trace); (b) with the best pulse found by a Genetic Algorithm in an 80-parameter unrestricted optimization (dashed line) and the best pulse found in a restricted 3-parameter optimization (solid line). The best pulse found be the GA consists of a sequence of two $120fs$ pulses, separated by $500fs$. The inset in (b) shows the evolution of the fitness value for the 80-parameter optimization (full squares, maximum fitness; open squares, average fitness).

2.2 Velocity-map imaging

Ion imaging techniques have proven to be of great importance in studies of chemical reaction dynamics [131], and have also been applied in atomic physics [132, 133]. Three-dimensional velocity distributions of electrons or ions are projected onto a two-dimensional detector normally consisting of a microchannel plate (MCP) and a phosphor screen. The image on the phosphor screen is then recorded by a charge-coupled device (CCD) camera. A very intuitive

illustration is shown in Figure 2.6. In 1997, Eppink and Parker [134] improved the traditional ion imaging technique by applying electrostatic lenses instead of commonly used grid electrodes. This improvement makes Velocity-Map Imaging possible, where all particles with the same initial velocity vector are mapped onto the same point on the detector, thus significantly improving the spatial resolution of the recorded images.

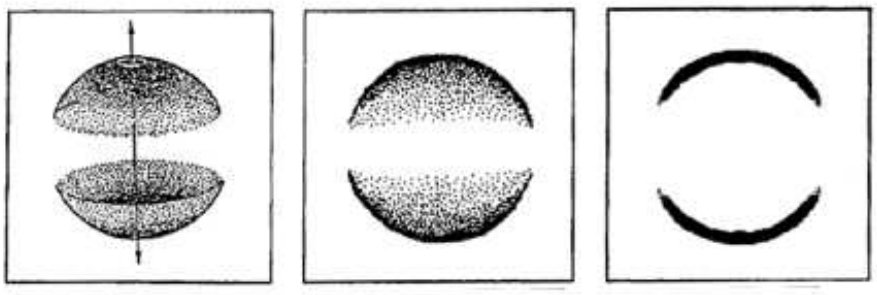

Figure 2.6: Illustration of the reconstruction of 3D distribution using the inverse Abel transformation by Heck and Chandler, taken from reference [131]. Left: Representation of a 3D distribution in space with cylindrical symmetry. Middle: 2D image obtained by projecting the 3D distribution shown in the left onto a 2D plane parallel to the symmetric axis, for example the paper plane in this context. Right: a 2D sliced image through the 3D distribution.

Consider the initial 3D distribution having a cylindrical symmetric axis z parallel to the 2D detector plane. The projection of each slice $f(x, y) = f(r)$ perpendicular to the z axis is a line $f(x)$ in the 2D image if projected along the y axis. This procedure corresponds to an Abel transform

$$f(x) = 2\int_r^\infty \frac{f(r)rdr}{\sqrt{r^2 - x^2}}. \tag{2.10}$$

The original slice of the distribution can then be obtained by an inverse Abel transform [131]

$$f(r) = -\frac{1}{\pi}\frac{\partial}{\partial r}\int_r^\infty \frac{rf(x)dx}{x\sqrt{x^2 - r^2}}. \tag{2.11}$$

The inversion can be done line by line, thus allowing a full reconstruction of the original 3D distribution. The inverse Abel transform is obtained in practice by taking the inverse Hankel transform of the Fourier transform of each line of the 2D image. However, this procedure is sensitive to the amount of noise in the image, and the noise is always accumulated as a central noise line in the reconstructed distribution. Instead of using an inverse Abel transform, an iterative inversion

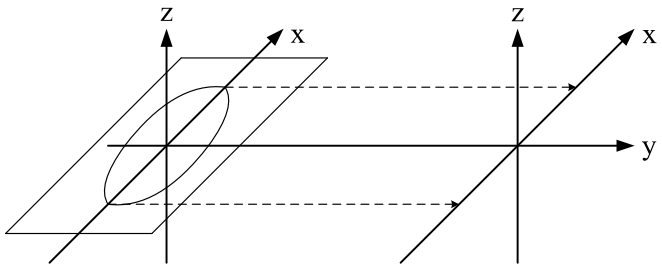

Figure 2.7: Abel projection of a slice $f(x, y)$ of the initial 3D distribution into a line $f(x)$ in a 2D plane.

scheme has been developed by Vrakking [135], which does not have the central noise line, thus further improving the quality of the reconstructed distribution.

Example of Velocity-Map Imaging: Enhanced ionization of Iodine molecules

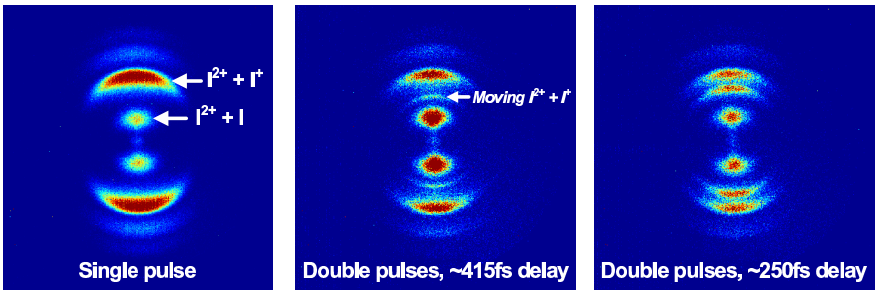

Figure 2.8: Multi-electron dissociative ionization of iodine molecules. See text for explanation of the process shown in the figure.

As a simple example, we show in Figure 2.8 the application of velocity imaging in multi-electron dissociative ionization of iodine molecules, which has been studied using a time-of-flight measurement by Corkum *et al* [136] in 1996. I_2 molecules were excited by a single ultrashort laser pulse. Measured I^{2+} signals contain contributions from dissociation channel $I^{2+} + I$, from Coulomb explosion channel $I^{2+} + I^{+}$ and from other higher Coulomb explosion channels not shown in the figure. We split the single pulse into two pulses with variable time delay between them by using a Liquid-crystal spatial light modulator (LC-SLM). While the molecule is dissociating in the $I^{2+} + I$ channel, the second laser pulse can further ionize the molecules, giving rise to the production of a $I^{2+} + I^{+}$ channel with a radius that depends on the timing of the second laser pulse.

Part II

Understanding electron dynamics during ionization

Chapter 3

Ionization of Rydberg atoms by radio frequency fields

Rydberg atoms in an external radio frequency field are used as a model system to study strong field ionization dynamics with sub-cycle time resolution. The electron emission can be controlled by manipulating the carrier-envelope phase, field amplitude and frequency of the driving field. We also show that by adding a second field with different frequency one can restrict the electron emission to a few field cycles while using a driving field of many cycles. This is of great interest for understanding and generating single attosecond laser pulses in the optical domain.

3.1 Introduction

As we have discussed in Chapter 1, the rapid development of ultrashort intense laser technology within the last decade has enabled many new findings in the field of intense-laser-matter interaction. A simple three-step recollision picture [21] has been developed to explain many of these strong field phenomena. In this model, electrons are first set free by tunneling through the potential barrier in the Coulomb + laser field potential or even escape over this barrier when the external field pushes this barrier below the binding energy of the electrons. The freed electron is then accelerated in the laser field, and finally driven back to the parent ionic core. Upon this recollision, three possible interactions may occur: elastic scattering, inelastic scattering, or radiative decay to the ground state. This can lead to three different observed phenomena: above-threshold ionization, non-sequential ionization, and high-order harmonic generation.

The ionization of atoms under the influence of a strong low frequency external field is inherently non-perturbative. In the tunneling regime, according to ADK theory [13], the ionization rate varies nonlinearly with the amplitude $E(t)$ of the applied field as

$$R \propto exp[-2(2I_p)^{3/2}/3E(t)], \tag{3.1}$$

where I_p is the field free ionization potential of the atoms. For laser pulses containing only a few optical cycles, the laser intensity changes dramatically from one cycle to the next. Under these conditions it becomes very interesting to investigate the actual time dependence of the ionization.

Integration of the 1D equations of motion of an electron in a linearly polarized field gives a cycle-averaged kinetic energy [137]

$$T = T_0 + 2U_p(1/2 + cos^2\omega t_0) - 2\sqrt{U_p}\sqrt{2T_0}cos\omega t_0, \tag{3.2}$$

where T_0 is the initial energy, U_p the ponderomotive energy (see equation 1.6 on page 14), and ωt_0 the initial phase of the laser field when the electron is freed. Upon recolliding with the ionic core, the electron's instantaneous kinetic energy is given by [137]

$$T_r = 2U_p(cos^2\omega t_r + cos^2\omega t_0 - 2cos\omega t_0 cos\omega t_r), \tag{3.3}$$

where t_r is the return time. One can see that the time t_0 at which the electron is ionized determines how much kinetic energy the electron will have when it collides with the ionic core, and thus the highest order harmonic that can be produced [138]. A single recollision event would naturally give a single attosecond laser pulse. The temporal width of the electron wave packet at the time of the

recollision determines the width of the attosecond extreme-ultraviolet bursts that are produced. A precise understanding of the electron dynamics on subcycle time scales is thus desirable if one wishes to improve the production of attosecond laser pulses using high-order harmonic generation. According to the three-step recollision model, the time that the electrons take to return to the core is just within one laser cycle. Ideally, one would like to investigate how the electron wave packet is emitted and how it evolves within the laser cycle. However, the required time resolution for such a study is of the order of 100 attoseconds for optical cycles. As an alternative, we propose scaling the physics by making use of low-frequency ionization sources, where subcycle time resolution can be achieved in the femtosecond or even in the nanosecond domain. Intense few-cycle radio frequency fields can be easily generated with readily available electronic equipment. Its shape, amplitude and carrier-envelope phase can be precisely controlled.

We recall that the general description of a laser field is given by $E_L(t) = E_0(t)cos(\omega_L t + \phi_0)$. Here $E_0(t)$ is the temporal envelope, ω_L is the laser frequency, and ϕ_0 is the carrier-envelope phase. Lasers whose carrier-envelope phases are not stabilized emit pulses with different ϕ_0 from shot to shot (see Figure 2.3). This instability can average out some important phase-dependent effects in strong field processes. Although phase-stabilized few-cycle lasers have been implemented [139], it is not yet available in many labs. In the radio-frequency domain used in this chapter, however, the generation of carrier-envelope phase stabilized pulses is trivially easy.

The ionization of highly excited Rydberg atoms by a radio frequency (RF) field provides a very similar system as in optical domain. As early as in 1974, Bayfield *et al* pioneered an experiment on microwave $(30MHz, 1.5GHz, 9.9GHz)$ ionization of highly excited Hydrogen atoms $(63 \leq n \leq 69)$, and suggested it as a useful scaled model for laser ionization of atoms in strongly bound states [140].

We first summarize a few important properties of Rydberg atoms. For a detailed discussion of Rydberg atoms, we refer to the book by Gallagher [141].

Rydberg atoms are atoms whose outermost electrons are excited close to the ionization threshold. Rydberg atoms are normally very large and remarkably stable compared to ordinarily excited atoms. Rydberg atoms have been detected whose diameter approaches a hundredth of millimeter. On the time scale of atomic phenomena Rydberg atoms live almost forever. Lifetimes between a millisecond and a second are common.

Rydberg atoms can be strongly distorted and even pulled apart by a relatively weak electric field. Similar to atoms in an strong optical field, the combination of the Coulomb potential and the external electric field forms a potential barrier.

The local maximum of this barrier is called the saddle-point, as shown in Figure 3.1. In the optical domain, electrons can escape from the atom by tunnelling through the potential barrier with a considerable rate. However, in Rydberg atoms, the barrier is so wide that electrons can hardly tunnel through. Only when the saddle point energy of the barrier is lower than the binding energy of the Rydberg electron can it be ionized. This is called *field ionization*. The binding energy of a state of quantum number n can be calculated for Hydrogen as (in atomic units unless otherwise stated)

$$E = -\frac{1}{2n^2}. \tag{3.4}$$

The saddle point energy induced by a external field F is given by

$$E = -2\sqrt{F}. \tag{3.5}$$

This gives a classical ionization threshold for the external electric field of a Rydberg electron with quantum number n

$$F = \frac{1}{16n^4}. \tag{3.6}$$

Rydberg states of Hydrogen and other atoms have a high degree of degeneracy. In an external electric field, the degenerate states of different angular momentum l are split into a series of Stark states. Stark states whose energy increases as a function of the electric field are called blue states, while states whose energy decreases are called red states (see Figure 3.1). The levels can be plotted as a function of the electric field in a so-called Stark map. For non-hydrogenic Rydberg atoms, avoided crossings are formed when red states of quantum number $n+1$ and blue states of quantum number n reach the same energy. Figure 3.1(a) shows a typical Stark level map of Rubidium $m = 0$ states around $n = 33$. A zoom of a portion of this Figure is shown in Figure 3.2.

In the case of Hydrogen, there is no coupling between the Stark states. For the extreme red states, the ionization threshold is increased and given by

$$F = \frac{1}{9n^4}. \tag{3.7}$$

For blue states, it is not possible to estimate the threshold field in a simple way. However, blue and red states of the same n and $m = 0$ often have threshold fields differing by a factor of 2. In non-hydrogenic atoms the Stark states are coupled by the presence of the core electrons. The blue states can be ionized on a faster time scale through the coupling with the red states.

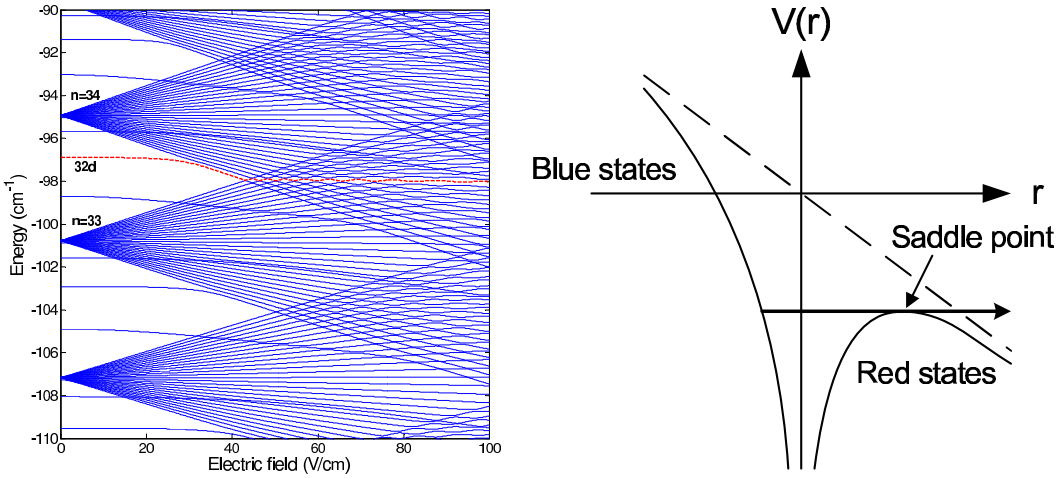

(a) (b)

Figure 3.1: (a) Stark level map of Rubidium atoms around $n = 33$, for $m = 0$ states. The dashed curve shows an adiabatic ionization path of the $32d$ state. (b) Potential of a Rydberg atom in an external field. Electrons can escape when they have an energy higher than the energy of the saddle-point in the Coulomb + external field potential.

In many experiments, including ours, pulsed electric fields are used, where the electric field may vary from zero to a maximum value several times. Rydberg states will then repeatedly evolve from zero-field angular momentum states to Stark shifted states. When the electric field is ramped, the avoided crossings between the blue and red Stark states (see Figure 3.2) can be traversed diabatically or adiabatically depending on the speed at which the crossing is taken. The probability of traversing a simple avoided crossing diabatically is given by the Landau-Zener formula [142]

$$P = exp[-2\pi|V|^2/\hbar(dW/dt)], \tag{3.8}$$

where V is the matrix element of the perturbation that gives rise to the avoided crossing ($2V$ is the separation of the levels at the crossing) and dW/dt is the rate of change of the level separation as the avoided crossing is approached. In an electric field, $dW/dt = (dW/dF)(dF/dt)$, where dF/dt is the slew rate of the field. Simply speaking, when the external field ramps very fast, a diabatic transition can occur. An adiabatic transition will happen at each avoided crossing if the field ramps very slow. Involvement of adiabatic transitions will lead to a broad distribution of states when reaching the ionization limit. In the next section we will argue that in our experiment ionization proceeds predominantly diabatically.

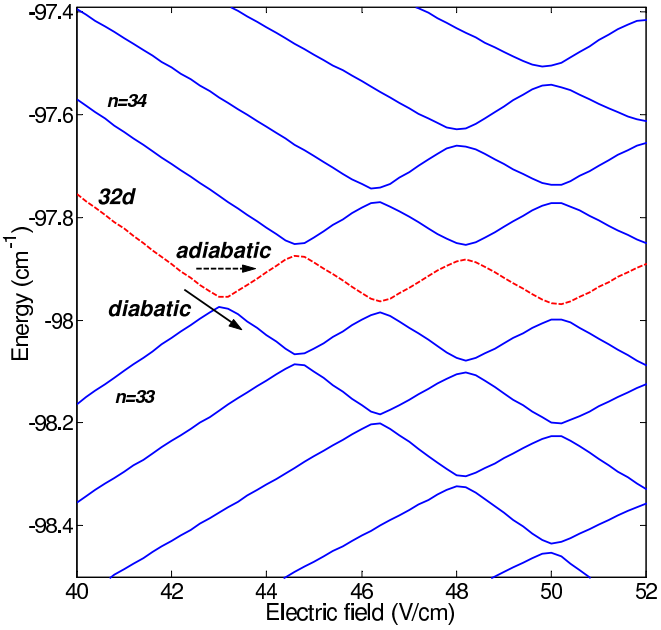

Figure 3.2: Two possible routes to pass an avoided crossings formed by the reddest states of the $n = 34$ manifold and the bluest state of the $n = 33$ manifold. Diabatic and adiabatic pathways are shown as solid and dashed arrows respectively. The dashed line shows the adiabatic pathway of the $n = 32d$ state.

Very recently, Gürtler *et al* have used Rydberg atoms as a model system to study time-resolved electron emission. Rubidium Rydberg atoms ($n = 90d$) were ionized by few-cycle radio frequency ($1 \sim 10MHz$) pulses [143]. The electron emission was observed to occur in multiple bursts and strongly depended on the carrier-envelope phase and the duration and amplitude of the RF pulses.

In this chapter, we will study the carrier-envelope phase dependency of the ionization process of highly excited Rubidium atoms ($n = 90d$) over a wider range of phase space. We will also study the ionization process under the influence of a two-color radio frequency field.

3.2 Experimental setup

The experimental setup was similar to the one used in reference [143]. The experiments were performed in a vacuum chamber ($10^{-7}mBar$). An atomic rubidium beam from a resistively heated oven was crossed by a $10Hz$ nanosecond dye laser beam. Atoms were excited by the narrow band laser ($\lambda = 593.714nm, \Delta\lambda =$

$0.005nm$) to a high Rydberg state $n = 90d$. Subsequent to the laser excitation the atoms were exposed to a few-cycle RF pulse. The RF electric field was defined as $E = E_0 e^{-(t/\tau)^2} cos(\omega t + \phi)$. Here τ is the pulse duration that was varied between $100ns$ and $500ns$, ω is the carrier frequency and ϕ is the carrier envelope phase. When changing the frequency or carrier envelope phase of the pulse, E_0 was chosen such that the pulse energy was kept constant during the experiment. A programmable arbitrary waveform generator (Agilent 33250A) was used to synthesize the few-cycle RF fields. The output waveform was amplified by an RF amplifier and then applied to a pair of capacitor plates spaced by $4.65mm$. The capacitor plates were set up in a 50Ω transmission line configuration. The RF fields were used to ionize the atoms and to accelerate the electrons towards an MCP detector. The time-resolved electron emission traces were then recorded with a digital oscilloscope. Electrons released at negative half-cycles of the RF pulses were pushed toward the detector and recorded, while electrons released at positive cycles were pulled away. A complete picture of the ionization was obtained by addition of two time traces with opposite field polarities.

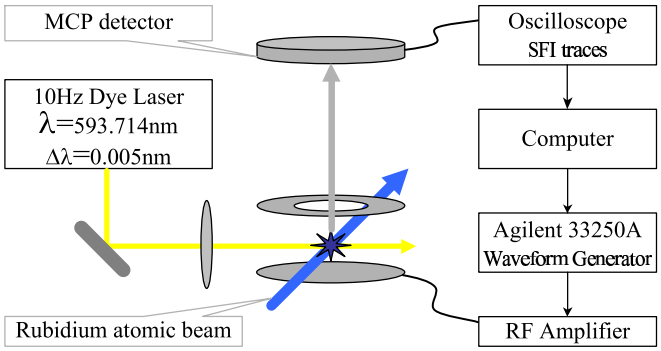

Figure 3.3: Experimental setup. Rubidium atoms are excited to a Rydberg state around n=90. A radio frequency field is generated with the Agilent 33250A waveform generator. The field is first amplified and then used to ionize the Rydberg atoms. Field ionization traces are recorded with an oscilloscope.

The amplified field strength of the RF field was varied between $10V/cm$ to $20V/cm$ in this experiment. These field strength are well above the ionization threshold for Rubidium $n = 90$, which is around $5V/cm$ according to Equation 3.6. Our $100ns$ few-cycle pulses have carrier frequencies around $10MHz$. This gives slew rates dF/dt as high as $500Vcm^{-1}\mu s^{-1}$ to $1000Vcm^{-1}\mu s^{-1}$. In a study on state-selective field ionization of Rubidium atoms, Gürtler *et al* have recorded field ionization traces for Rubidium atoms around $n = 32$ at variable ramping rates [143]. They have shown that under these conditions the ioniza-

tion traces become indistinguishable at ramping rates of about $1000 V cm^{-1} \mu s^{-1}$. Considering that $n = 90$ states are used in our experiment, we may conclude that most of our measurements are safely in the diabatic regime. The fact that only sharp ionization peaks are observed in the field ionization traces that will be presented below also confirms this statement.

3.3 One-color experiment

Figure 3.4 shows a radio frequency field and its corresponding field ionization trace. Rubidium Rydberg atoms are ionized with a $20 MHz, 250 ns$ amplified radio frequency field. Electrons are emitted at each half field cycle when the instantaneous field rises over the ionization threshold. A sub-cycle resolution is achieved by using a low frequency field and Rydberg atoms, which is a very difficult to achieve in optical domain.

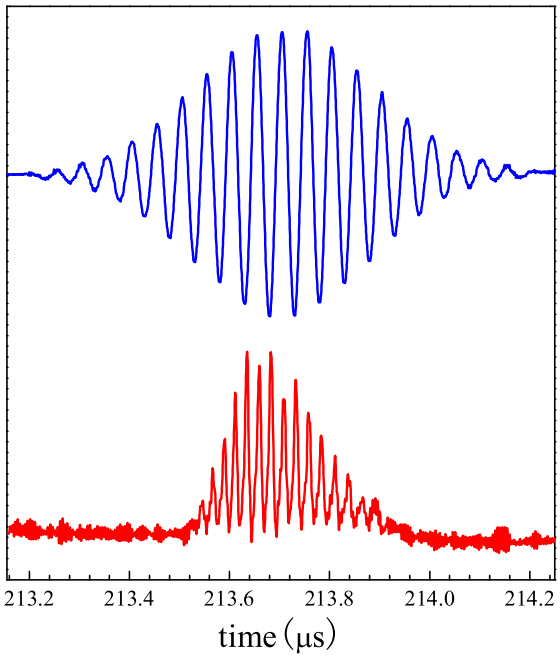

Figure 3.4: Upper: $20 MHz$ amplified radio frequency field. Lower: recorded electron emission traces. Electrons are emitted at each half field cycle when the local field reaches the ionization threshold.

Using a radio frequency field, we can easily and precisely control the carrier-envelope phase of the electric field, which is again a very difficult task in the optical domain. Consequently we first looked at the influence of the carrier-

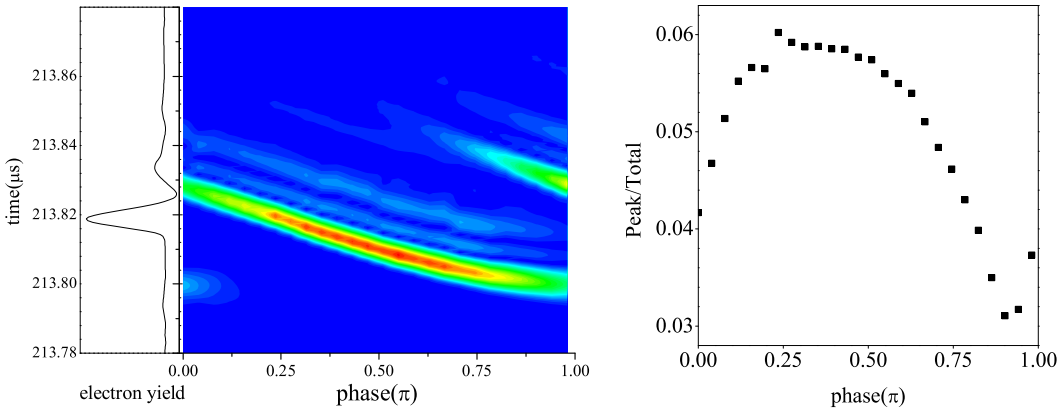

(a) (b)

Figure 3.5: (a) Contour plot of field ionization traces as a function of carrier-envelope phases. The peak amplitude was $9V$ after amplification. The left panel shows a typical ionization trace. (b) Figure-of-merit P/T (see text) as a function of carrier-envelope phase ϕ. Clearly the range from $\pi/4$ to $\pi/2$ is favorable for a single electron emission peak.

envelope phase on the ionization process in our experiment. A contour plot of field ionization traces recorded for few-cycle RF fields with different carrier-envelop phases ϕ is shown in Figure 3.5(a). Since our interest is to study the electron emission process at a sub-cycle time scale, we define a figure-of-merit for these traces which is defined as the ratio of the maximum electron emission yield $P(Peak)$ to the integral of the time-dependent electron yield $T(Total)$. Carrier envelope phases that yield a high figure-of-merit correspond to situations where electrons are mostly ionized within one half-cycle of the RF field. The value of P/T as a function of phase ϕ is plotted in Figure 3.5(b). When the carrier envelope phase ϕ is varied from 0 to π, we clearly see that there is a region, roughly from $\pi/4$ to $\pi/2$, where electrons are ejected as a single peak, while in another region, several peaks are visible, leading to a lowering of the figure-of-merit. A closer look is shown in Figure 3.6. At $\phi = 0$, two electron emission peaks are found, but when we change the phase to $\phi = 42.35^o$, only a single emission peak appears that results from the most intense half-cycle in the pulse. As we have discussed in the introduction part, the ionization process is highly nonlinear as a function of the field amplitude. A slight phase shift thus manages to avoid ionization in the first half-cycle.

We note that we have observed in our experiments that the Rydberg atoms are depleted after the field maxima at the highest field amplitudes used. Saturation

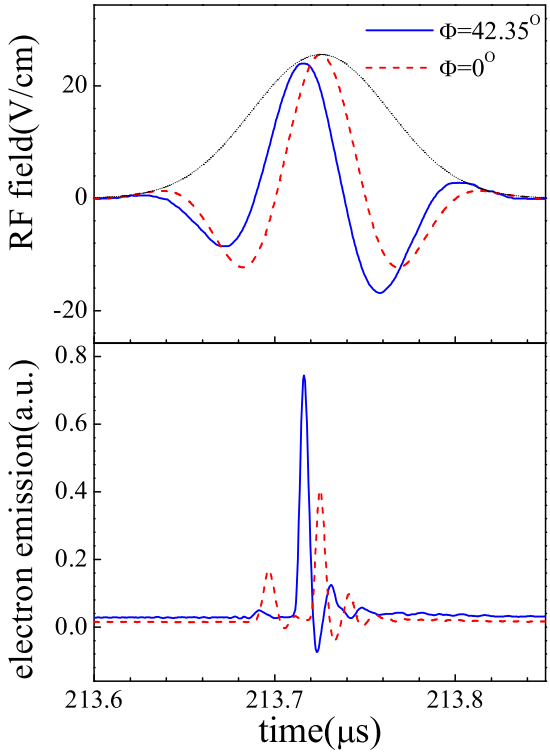

Figure 3.6: Radio frequency fields with carrier-envelope phase $\phi = 0$ and 42.35^o (upper) and electron emission traces (lower). For $\phi = 42.35^o$ the electrons are emitted within a single half-cycle . For $\phi = 0$, the electrons are emitted over two half-cycles.

effects can be used in optical strong field ionization to control the ionization process, and consequently to affect the generation of attosecond laser pulses.

The clear carrier-envelope phase dependence observed in our experiments inspired us to apply a feedback loop to search for the best results in a parameter space consisting of carrier-envelope phase, pulse duration and field frequency. The carrier-envelope phase ϕ, the pulse duration τ and the number of cycles in the pulse N were chosen as variable input parameters of a simple genetic algorithm. The previously introduced figure-of-merit P/T was used as fitness value, and was deduced based on the recorded electron emission traces that were created by a set of radio frequency fields. According to the fitness value the algorithm generates a new set of waveforms which in turn were amplified and applied to ionize the Rydberg atoms in the vacuum chamber. The pulse duration was allowed to vary from $100ns$ to $500ns$, and the number of cycles was varied from 1 to 5. The frequency was then determined by the pulse duration and the number

of cycles. However, frequencies were limited between $5MHz$ to $25MHz$ due to the bandwidth of the amplifier. The best result, which converges to a quasi-single cycle pulse, of this optimization is shown in Figure 3.7, detailed discussion will be given on the next page.

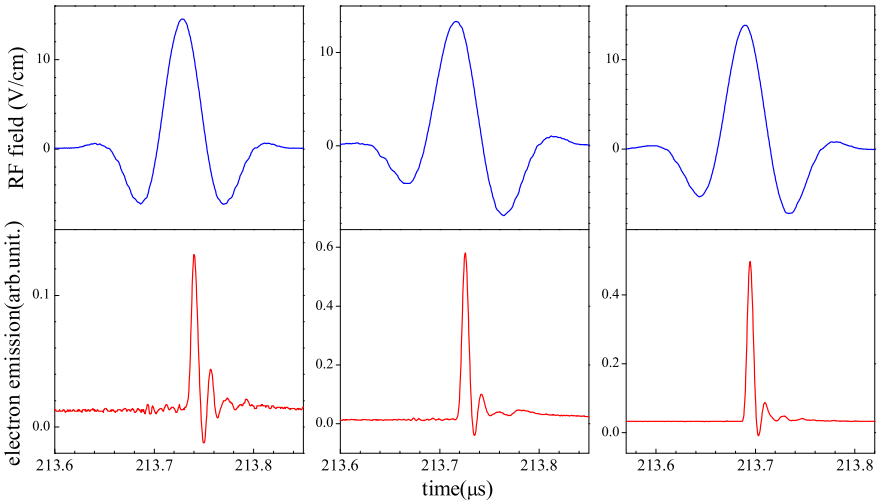

Figure 3.7: Best results of radio frequency fields and corresponding electron emission traces for three different optimization schemes: P/T (left), $1/(\omega\Delta t)$ (middle) and their combination $P/(T\omega\Delta t)$ (right), where P is the maximum of electron emission yield, T the total electron yield, ω the field frequency and Δt the full width at half maximum of the electron emission trace.

Fitness definition	Phase shift $\phi(\,^o)$	Frequency $f(MHz)$	Period $T(ns)$	Duration $\tau(ns)$
P/T	2.12	10	100	100
$1/\omega\Delta t$	30	9	111.1	112.55
$P/T\omega\Delta t$	14.42	9.4	106.4	109.41

Table 3.1: Corresponding field parameters of the three radio frequency fields shown in Figure 3.7. See text for detailed explanation.

In addition to the previously introduced fitness definition P/T two further fitness definitions were used in the experiments. Fitness definition P/T allows us to search for electric fields where electrons are confined as much as possible to a single half-cycle. A second fitness value was defined as $1/(\omega\Delta t)$, where Δt is the full width at half maximum of the electron emission trace. This will

direct the experiments to search for solutions where the width of the electron emission traces are narrow compared to the field cycle. The last fitness function used is a combination of these two $P/(T\omega\Delta t)$, and is motivated by what one wishes to accomplishes in a high harmonic generation experiment, namely the generation of an isolated attosecond pulse that is as short as possible. In all these experiments, the peak amplitudes were chosen to be $5V$, and the pulse energy during the experiment was kept constant. We have carefully checked that at this peak amplitude there were no depletion in all measurements.

Figure 3.7 and Table 3.1 give a summary of the best results for the three optimization experiments discussed above. All the best radio frequency fields actually went to the shortest possible pulse duration in the measurements, i.e, about $100ns$, although with a small phase shift. Since the field ionization is a highly nonlinear process, to have most electrons emitted in one half-cycle one needs to concentrate the pulse energy in one single half cycle of a short pulse. Thus in the P/T optimization the radio frequency field goes to the shortest pulse duration and lowest frequency available in the experiment, which are $100ns$ and $10MHz$. However, in our experimental setup, the ionizing field also acts as the accelerating field. In order to have narrow electron emission peak a high acceleration field is needed. This partially explains why the $1/(\omega\Delta t)$ optimization finds different optimal carrier envelope phase. Not surprisingly the third optimization $P/(T\omega\Delta t)$ falls in between the results of the other two optimizations. Indeed, in the generation of single attosecond pulses in optical domain, a strong ionization half-cycle followed by a stronger acceleration half-cycle is found to be the optimal solution, see Figure 3.12, where two fundamental laser fields are used to prepare such a driving field.

Our experimental results indicate that few-cycle pulses are indeed a way to generate a single electron emission peak, and to generate a single attosecond peak in the optical domain. But, in the following two-color experiments, we will show, few-cycle pulses are not necessary for the generation of single attosecond pulses.

3.4 Two-color experiment

In this part, we investigated ways in which the ionization process can be influenced by shaping of the field cycle through the use of two-color fields, which minimizes the size of the wave packet (compared with the RF period) or confines the ionization to a small portion of the RF pulse. The waveform generator produced a two-color RF field, which consisted of few-cycle pulses with a Gaussian envelope and was given by $E(t) = E_0 e^{-(t/\tau)^2}[cos(2\pi f_1 t + \phi_1) + \alpha cos(2\pi f_2 t + \phi_2)]$,

where E_0 is the amplitude of field 1, τ is the pulse duration, f_1, f_2 are the two frequencies used, and ϕ_1, ϕ_2 are the carrier-envelope phases of the two components. α describes the relative strength of field 2. Field amplitude E_0 was normalized such that the energy of the pulse remained constant when the field parameters were varied as described below.

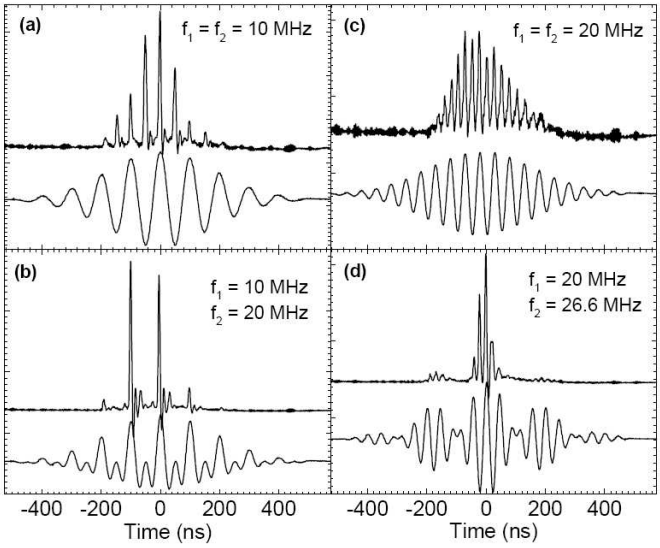

Figure 3.8: RF pulse fields (bottom curves) and corresponding electron TOF measurements (top curves) for a 250ns pulse duration and fundamental frequencies of 10 (left) and 20 (right) MHz. For (a) and (c), only the fundamental frequency is present, whereas for (b) and (d) an equally intense frequency contribution is added: (b) fundamental + second-harmonic frequency, (d) fundamental + incommensurate frequency.

Figure 3.8 shows the results of an experiment in which Rb 90d atoms were ionized by use of 250-ns-long pulses and a 10 or 20MHz RF carrier frequency. Figure 3.8 (a) and (c) clearly show that electron emission occurs on every half-cycle. Adding a second frequency component dramatically changes the time-dependent ionization. For instance, adding a second-harmonic contribution can limit the ionization to once per fundamental period [Figure 3.8(b)]. Or, by using an incommensurate second frequency component, $f_2 = 4/3f_1$, one can restrict the ionization to the central part of the fundamental pulse [Figure 3.8(d)]. Thus, starting from quite a long (15 cycle) pulse, one can restrict ionization to a rather short time range, as if a much shorter (3$\sim$ 4 cycle) pulse had been used.

In what follows, we discuss the influence of different RF field parameters on the ionization in more detail. From the two examples above one can, however, already

identify two pertinent strategies. On the one hand the duration, amplitude, and phase of the harmonics of a given fundamental frequency can be used to limit the electron emission to a single burst per optical cycle and to minimize the duration of these bursts compared with the RF period. On the other hand, incommensurate frequencies can be used to confine the ionization to a small time interval within the fundamental pulse.

Addition of a second harmonic

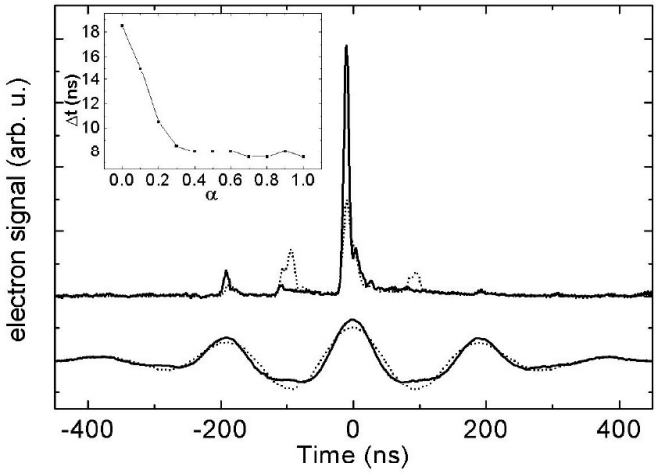

Figure 3.9: Ionization yield versus time (top curves) for two different RF fields (bottom curves). Dotted curves, RF field with only one frequency component $f_1 = 5.14MHz$, leading to ionization on every half-cycle. With only 9% (in energy) of second harmonic $f_2 = 10.28MHz$ (solid curves), electron emission occurs only once per fundamental cycle. The carrier phases of the two frequencies are zero. Inset, duration of the main electron peak as a function of second harmonic amplitude. The total energy of the pulses was held constant.

First we concentrate on the use of a fundamental frequency ($5.14MHz$) and its second harmonic ($10.28MHz$) and the conditions for achieving ultrashort electron bursts. The pulse was $250ns$ long (two cycles at $5.14MHz$) with carrier phases $\phi_1 = \phi_2 = 0$. Figure 3.9 shows the real-time ionization signals for $\alpha = 0$ and $\alpha = 0.3$. For $\alpha = 0.3$ a decrease of the full width at half-maximum Δt can be observed and the electrons are emitted only once per cycle. One can understand this behavior by considering the time variation of the field and the high nonlinearity of the ionization process. Addition of the harmonic increases the maximum field that occurs. This maximum field value is reached faster, leading to

a shorter, more-intense electron burst; the former property is furthermore aided by the fact that the ionization is partly saturated. As the field is symmetric near $t = 0$, one would also expect the ionization signal to be symmetric. However, as we keep the pulse energy constant, variations in the pulse parameters lead to high field values that deplete the population in the Rydberg states significantly, leading to the asymmetry observed in the figures.

These effects rely on a delicate shaping of the field cycle, with small differences leading to dramatic effects. The amount of second harmonic needed to minimize Δt is quite low: The factor 0.3 in amplitude translates into only 9% of the total energy. The inset of Figure 3.9 shows the duration Δt of the most intense electron peak as a function of relative amplitude α of the second harmonic. As soon as the amplitude reaches 0.3 the duration remains almost constant (and above the instrumental limit of $3ns$). The decrease in the duration of the electron pulse is accompanied by an increase in the ionization efficiency.

Phase effect of the added second harmonic

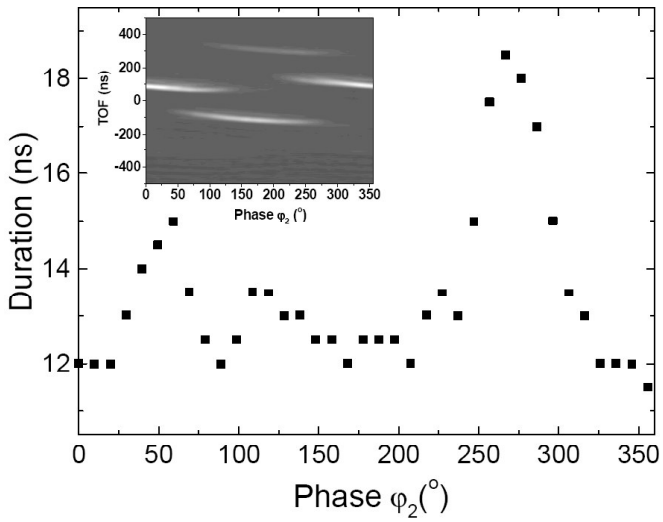

Figure 3.10: Duration of the most intense electron pulse as a function of the relative phase between the fundamental ($5.14MHz$) and the second-harmonic ($10.28MHz$) field oscillations ($250ns$ pulse duration, $\phi_1 = 0$). The energy of the pulses was kept constant for all values of the phase. The second-harmonic frequency contribution is 9% of the total energy. Inset, contour plot of the electron TOF as a function of the relative phase between the fundamental and second-harmonic field oscillations.

Next we look at the influence of the relative phase between the fundamental

and second-harmonic field oscillations. Figure 3.10 shows the duration of the electron pulses Δt as a function of phase ϕ_2 for $\alpha = 0.3$ and $\phi_1 = 0$. The duration depends sensitively on phase ϕ_2. It is minimal for $\phi_2 = 0, 90^o, 180^o$, and it has a strong maximum for $\phi_2 = 270^o$. Meanwhile, the ionization efficiency remains almost constant as a function of ϕ_2. The determination of the pulse width was made on the most prominent peak in the electrons' TOF. As shown in the inset of Figure 3.10, the ionization signal is confined to a single peak for $\phi_2 = 0$. For other values of ϕ_2 there are three electron peaks in the signal. In considering the implications of these results for high harmonic generation, one should realize that the present experiments probe the initial ionization of the electron only. The electrons are emitted at a maximum of the field, and the subsequent variation of the field may not drive the electron back to the core. For the production of single attosecond pulses it may be better to have two cycles of equal amplitude beneath the envelope, the first one to allow for ionization and the second to drive the electron back to the core.

Addition of an incommensurate frequency

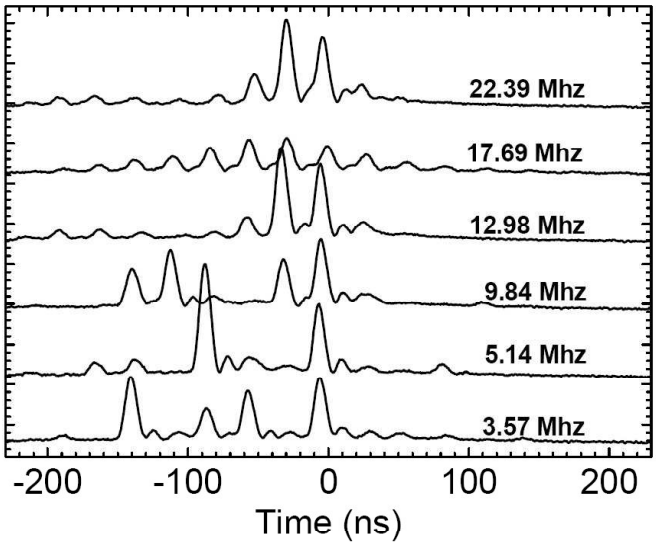

Figure 3.11: Electron TOF measurements for 250-ns long pulses (16 cycles) with different frequencies added to the fundamental frequency of $17.69 MHz$. The contribution of the second frequency is 9% of the total energy.

So far we have discussed subcycle electron emission times for few-cycle RF fields. Next we look at the possibility of restricting the ionization to a few cycles when pulses with many cycles are used. For $250 ns$ -long pulses with frequency

$f_1 = 17.69MHz$ (i.e., 16 cycles), real-time ionization traces were recorded as a function of f_2 of a second component that contributed 9% to the total energy of the RF field. (Figure 3.11). Dramatic changes in the ionization profile are observed that are due to the exponential dependence of the ionization rate on the electric field. In Fig. 3.10 the case with only one frequency $f_1 = f_2 = 17.69MHz$ is clearly the least desirable, as electrons are emitted on every half-cycle during the entire pulse. For $f_2 = 22.39$ and $12.98MHz$, the ionization is nicely confined to a few cycles, and only three prominent electron peaks are observed (as opposed to 12 peaks for the single-frequency case). Another interesting case is obtained for $f_2 = 5.14MHz \approx f_1/3.5$, where only two prominent isolated peaks are observed, separated by three half-cycles. A polarization-gating technique [79, 144] might be able to select only one of them, thus providing a route toward the creation of an isolated attosecond pulse.

3.5 Conclusion and future work

In conclusion, we have demonstrated that a single electron emission peak can be generated over a small range of carrier-envelope phase. This observation holds the possibility of helping to understand and generate a single electron wavepacket in the optical domain in order to generate a single attosecond pulse. We also point out that a learning algorithm can be used to search for optimum solutions over a wide range of parameter space including carrier-envelope phase, field frequency, field amplitude, pulse duration etc.

We have also shown that ionization dynamics can be dramatically influenced by use of two-color few-cycle pulses and a subtle reshaping of the field oscillation. The number of electron bursts can be limited, and the electron emission can be confined to an interval that is short compared with the pulse duration. This research may inspire similar experiments in the optical domain aimed at the generation of single attosecond pulses and the use of electrons as probes of molecular dynamics.

Based on the understanding from this experiment, Siedschlag *et al* [145] have studied high-order harmonic generation in Hydrogen atoms exposed to a superposition of two linearly polarized laser fields with different colors. The full three-dimensional Schrödinger equation for the hydrogen atom was solved numerically to obtain the single-atom response. Phase-matching effects were also taken into account in the limit of small atomic density. The results (see Figure 3.11) clearly indicate the possibility of creating isolated attosecond pulses from many-cycle ($\tau_{FWHM} = 9.5fs$) driving pulses by an appropriate tuning of the two laser fre-

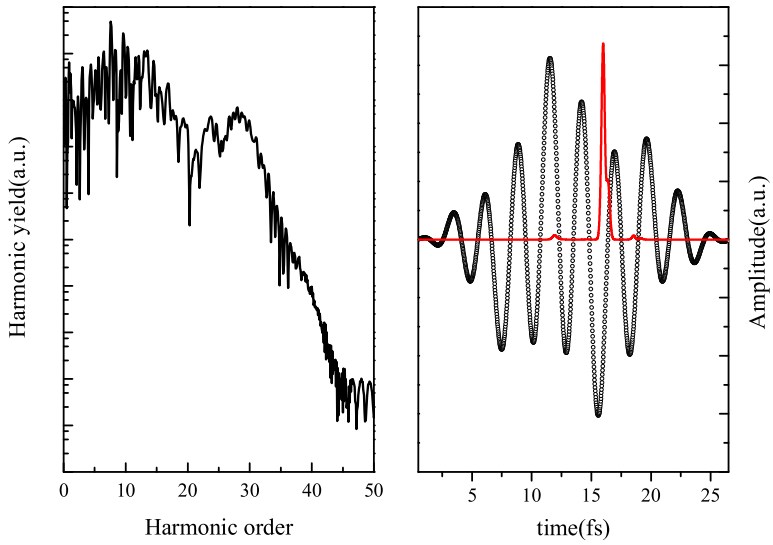

Figure 3.12: (Left) HHG spectrum of a single H atom irradiated by a two-color field ($I_1 = 8.77 \times 10^{13} W/cm^2, \lambda_1 = 780nm; I_2 = 0.09 I_1, \lambda_2 = 2680nm$). The pulse length T_{FWHM} was $9.5fs$ for both colors, and the carrier-envelope phases were both zero. A spectral window around the 27th harmonic was used to generate the attosecond response in the right. (Right) The open circles show the two-color laser field and the solid line shows the attosecond pulses generated. From reference[145]

quencies, which results in control of the ionization and the recollision dynamics of the electronic wavepacket.

Chapter 4

Above-threshold ionization of Rydberg atoms by intense far-infrared laser fields

Powerful output from the FELIX free electron laser brings us from the radio frequency to the far-infrared wavelength regime, and a big step closer to the optical domain. Above-threshold ionization becomes possible with these strong far-infrared laser pulses when using low-lying Rydberg states of Xenon, which constitutes another model system for better understanding the mechanism of strong field ionization processes in the optical domain. The low (terahertz) frequencies of these laser pulses can (in the future) allow us to probe sub-cycle electron dynamics with readily available femtosecond laser pulses.

4.1 Introduction

In strong field laser physics, ionization of an electron followed by acceleration of the electron and a re-collision with the ion left behind lies at the basis of several experimental techniques that have attracted considerable interest in the last few years. Ion-electron recombination accompanied by the emission of an XUV/x-ray photon leads to the formation of attosecond laser pulses, which show tremendous promise in experiments that are aimed at studying time-dependent electron dynamics. Furthermore, the re-collision electron can be used to probe the properties of the atom or molecule that it originates from. Re-collision electrons can be used for tomographic imaging of molecular wave functions [146], and to determine molecular structures by means of diffraction [147, 148]. They can even be used to observe nuclear motion on sub-femtosecond timescales using Coulomb explosion imaging [149].

Though of considerable interest, it is by today's standards impossible to study the wave packet motion of the ionized electron and the re-collision process in real time, since this requires time-domain studies with a time-resolution of 50 attoseconds or less. Therefore we have proposed to carry out atomic ionization experiments using a far infrared low-frequency ionization source. In a low-frequency laser field the time-scales for the electron wavepacket motion and the electron-ion re-collision can be slowed down to such an extent that probing of this motion in the time-domain may be feasible.

Intense field ionization can alternatively be described in terms of a multi-photon or field ionization picture. The multi-photon ionization picture applies when the ionization yield scales as $S \sim I^N$, where N represents the minimum number of photons that is required to ionize the atom and I is the intensity of the laser. In the field ionization picture, ionization occurs by passing over or tunneling through a potential barrier formed by the Coulomb and laser electric fields.

As we have discussed in Chapter 1, the transition from the multi-photon to the field ionization regimes is usually related to the Keldysh parameter $\gamma = (I_p/2U_p)^{1/2}$ [10]. For $\gamma >> 1$ the time needed for the electron to tunnel through the combined Coulomb-laser field potential barrier significantly exceeds the length of the optical cycle of the laser, and ionization occurs by multi-photon ionization. For $\gamma << 1$ the reverse is the case, and ionization proceeds by tunnelling through or passing over the barrier in the combined Coulomb-laser field potential. If an electron is released into the continuum by means of field ionization, it can be accelerated by the laser field up to a kinetic energy of $2U_p$ [21]. If the driven motion of the electron under the influence of the laser field leads to

a re-collision with the parent ionic core, then the electron kinetic energy can be further increased and may reach a maximum of $10U_p$ [27]. Hence, in experimental ATI spectra the observation of photoelectrons beyond $2U_p$ is the traditional signature of re-collision.

4.2 Above-threshold ionization of Xenon with free electron laser

In this experiment, a beam of metastable Xenon atoms was prepared in the $6s[3/2]_{J=2}$ state by electron impact excitation. This metastable beam propagated along the symmetry axis of a velocity-map imaging photoelectron spectrometer. It was crossed at right angles by the focused output from a Lambda Physik Scanmate dye laser that excited the Xenon atoms to a series of Rydberg states shown in Figure 4.1.

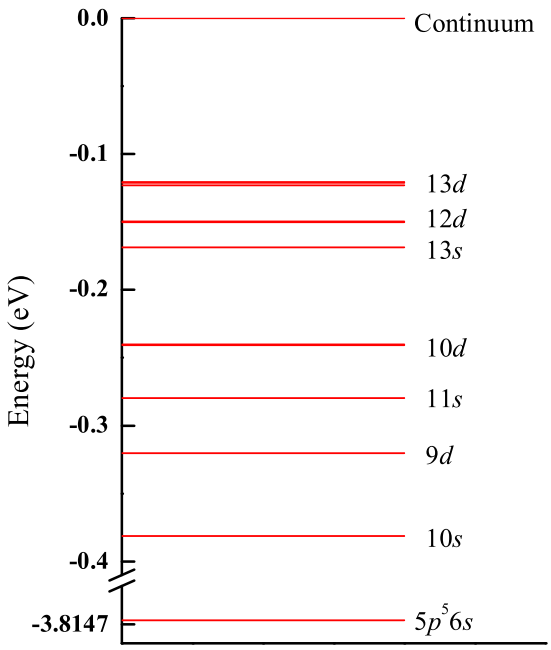

Figure 4.1: Xenon Rydberg states that are prepared from the $6s[3/2]_{J=2}$ metastable state through excitation with a tunable dye laser. These Rydberg states are further ionized with far-infrared free electron laser pulses with a wavelength ranging from 8 to 150μm.

Far infrared laser pulses from a free electron laser were then used to ionize the Rydberg state Xenon atoms. The free electron laser facility (FELIX) provides

continuously tunable radiation in the spectral range of $40-2500cm^{-1}(4-250\mu m)$, at peak powers ranging up to $100MW$ in (sub)picosecond pulses. The infrared beam consists of short micropulses, which have a nominal duration of $5ps$ and are separated by intervals of either $1ns$ or $40ns$ of zero intensity [150]. The micropulses form a train (the macropulse) with a duration up to $1\mu s$. The macropulses are repeated every few hundred ms, with a maximum repetition rate of 10 Hz. A single micro-pulse was selected from the $4\mu s$ macropulse from the free electron laser. The selected pulses were focused using an off-axis parabolic mirror with $(F/D) \approx 10$, where F is the focal length of the lens and D is the diameter of the free electron laser beam on the optic.

The photoelectrons were accelerated in a $530V/cm$ extraction field and projected onto a 2D imaging detector consisting of a dual microchannel plate assembly followed by a phosphor screen and a CCD camera system.The polarization of the free electron laser was chosen parallel to the 2D imaging detector. Photoelectron images were recorded as a function of the wavelength, pulse duration and intensity of the free electron laser, and as a function of the Rydberg state prepared by the tunable dye laser.

Dependence of ATI of Xe($10d$) state on wavelength

In Figures 4.2 and Figure 4.3 a series of experimental results are given for the ionization of Xenon $10d$ by the free electron laser, where the wavelength of the laser was varied between $42\mu m$ and $120\mu m$. Figure 4.2 shows 2D slices through the reconstructed 3D velocity distributions that were obtained by inverse Abel transformation of the experimental data. The images show a series of rings, indicating that the photoelectrons are formed with discrete energies. As can be seen in Figure 4.3, where the angle-integrated photoelectron kinetic energy spectra are shown, these energies correspond to a series of above-threshold ionization peaks separated by the energy of a single photon, and are due to the fact that the ionization occurs by the absorption of more than the minimum number of required laser photons.

In order to assess whether the measurements shown in Figure 4.2 are likely to have been performed in the multi-photon or in the field ionization regime, we will first evaluate the ponderomotive energy and the Keldysh parameter for the measurement performed with the free electron laser operating at a wavelength of $42\mu m$. The measurement in Figure 4.2 was taken using a laser bandwidth $\Delta E/E \sim 0.4\%$. Using the relation for a Gaussian pulse that $\Delta E/E \leq 0.373/N$, where N is the number of cycles in the pulse, we may conclude that the number of cycles in the experiment was at least 100. This means that the laser pulse

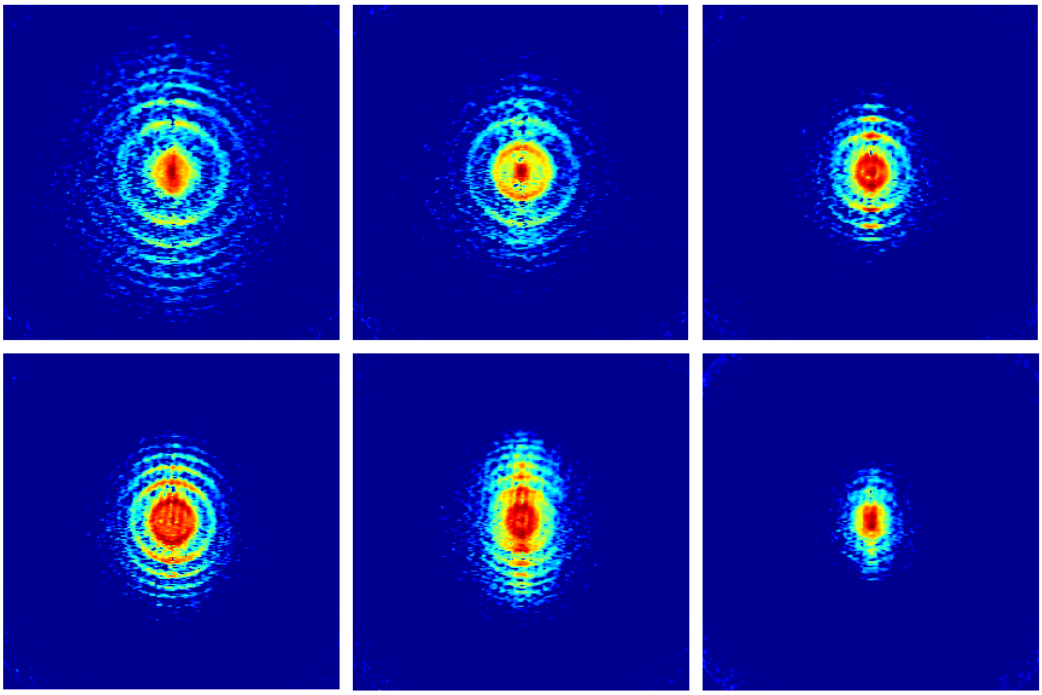

Figure 4.2: Inverted images of above-threshold ionization of Xenon $10d$ state ionized with short free electron laser pulses. The bandwidth was confined to $\Delta E/E < 1\%$ in all cases. The laser wavelength was tuned from $42\mu m$ to $120\mu m$. The wavelengths corresponding to the measurements shown in the figure are $42\mu m, 50\mu m, 70\mu m, 80\mu m, 100\mu m, 120\mu m$, from top-left to bottom-right.

was at least $12ps$ long and (using a pulse energy of $10\mu J$) had an instantaneous power of up to $0.8MW$. Assuming that the laser was focused to a diffraction-limited spotsize $w = (4\lambda/\pi)(F/d) \sim 540\mu m$, this suggests that the $42\mu m$ laser pulse had an intensity as high as $3.6 \times 10^8 W/cm^2$. The anticipated laser peak intensity scales with λ^{-3}, through a combination of lengthening of the pulse and the reduced tightness of the focus for longer wavelengths. Using the fact that $1a.u. = 3.51 \times 10^{16} W/cm^2$, an intensity of $3.6 \times 10^8 W/cm^2$ corresponds to a laser peak field strength of approximately $F_{laser} = 10^{-4} a.u.$ Consequently the maximum ponderomotive energy is $U_{p,max} = F_{laser}^2/4\omega^2 = 0.0021 a.u. = 0.058eV$ (using the fact that at $42\mu m$ wavelength the frequency of the laser in atomic units is equal to $0.00108 a.u.$). Hence, the observed extension of the photoelectron spectrum to about $0.2 \sim 0.25eV$ appears to be beyond the semi-classical limit of $2U_p$. For the determined value of U_p the Keldysh parameter $\gamma = (I_p/2U_p)^{1/2}$ is approximately 1.4.

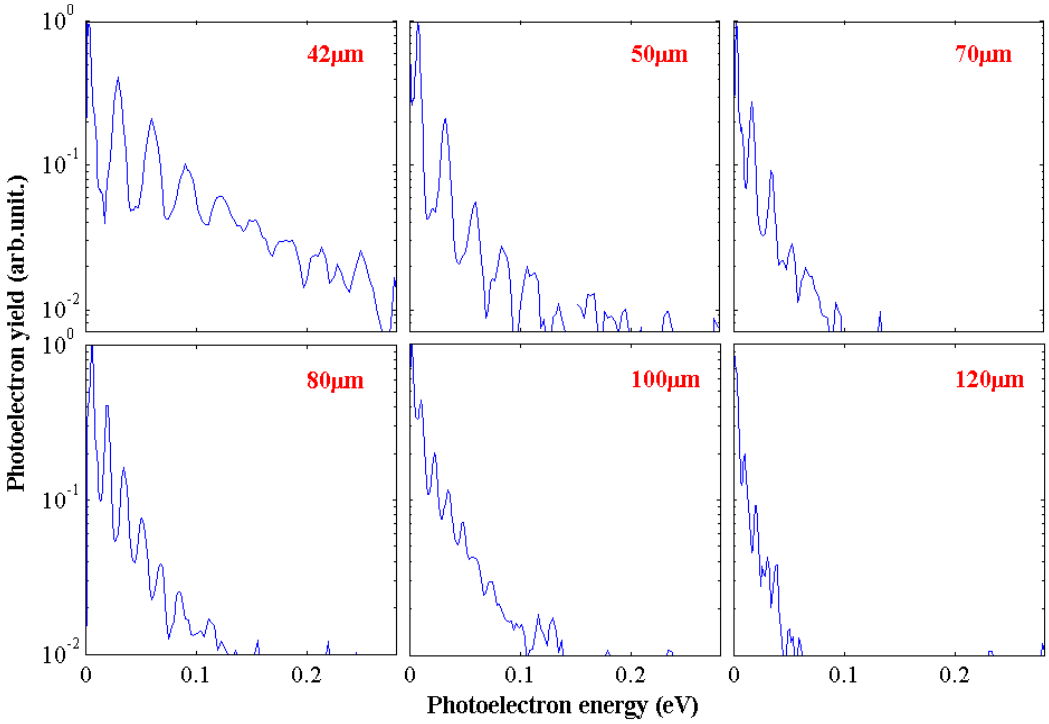

Figure 4.3: Corresponding angle-integrated photoelectron spectra for the measurements shown in Figure4.2, where Xenon $10d$ state was ionized by the free electron laser pulses. The laser wavelength was tuned from $42\mu m$ to $120\mu m$. The bandwidth of the pulse was confined to $\Delta E/E < 1\%$ in all cases. The laser wavelength was tuned from $42\mu m$ to $120\mu m$.

Noting that the uncertainties in the determination of the ponderomotive energy are likely to be as much as a factor of 2 and will likely lead to an overestimation rather than an underestimation of the ponderomotive energy, we conclude that the extension of the photoelectron spectrum beyond $2U_p$ and the evaluation of a Keldysh parameter larger than 1 suggest that the experiments were performed in the multi-photon regime.

Combining the λ^{-3} scaling of the focused peak intensity with the λ^2 scaling of the ponderomotive energy, we anticipate a λ^{-1} scaling for the highest energies observed in the photoelectron spectrum. Indeed, a reduction of the maximum photoelectron kinetic energy with increasing wavelength is observed. However, using the same reasoning the Keldysh parameter is expected to scale up with $\lambda^{1/2}$. Therefore, perhaps contrary to intuition, the Keldysh parameter increases with free electron laser wavelength and for longer wavelengths the experiments moves more and more into the multi-photon regime. This is caused by the fact

that towards longer wavelengths the focused laser intensity drops of more rapidly (with λ^{-3}) than the increase in the ponderomotive energy due to its λ^2 scaling.

Dependence of ATI of Xe($10s$) state on pulse duration

In the experiment, the laser intensity can be increased by reducing the duration of the laser pulse. In Figure 4.4 a series of measurements are shown for ionization of the Xenon $10s$ state ($0.38eV$ binding energy) using $42\mu m$ free electron laser pulses where the bandwidth was varied between $\Delta E/E \approx 0.4\%$(long pulse) to $\Delta E/E = 1.6\%$(short pulse). In this case the ionization involved the absorption of at least 13 laser photons, and the intensity in the experiment would be estimated as $1.5 \times 10^9 W/cm^2$ for the shortest pulses, leading to $U_p = 0.233eV = 0.0085a.u.(\gamma \sim 0.9)$. Corresponding angle-integrated photoelectron spectra are shown in Figure 4.5.

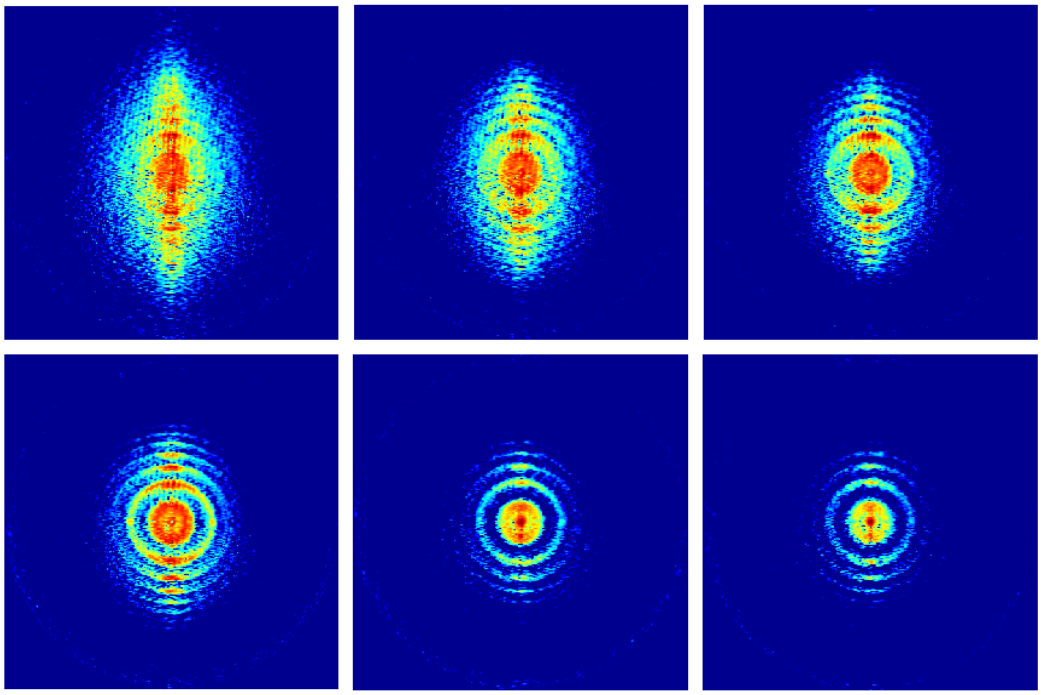

Figure 4.4: Inverted images of above-threshold ionization of Xenon $10s$ state ionized by 42 μm free electron laser pulses. The pulse duration is varied by changing the spectral bandwidth of the free electron laser. The bandwidth of the output pulse varies $\Delta E/E \approx 1.6\%$ (short pulse) in the top-left image to $\Delta E/E \approx 0.4\%$ (long pulse) in the botton-right image. The pulse energies were typically around $10\mu J/pulse$.

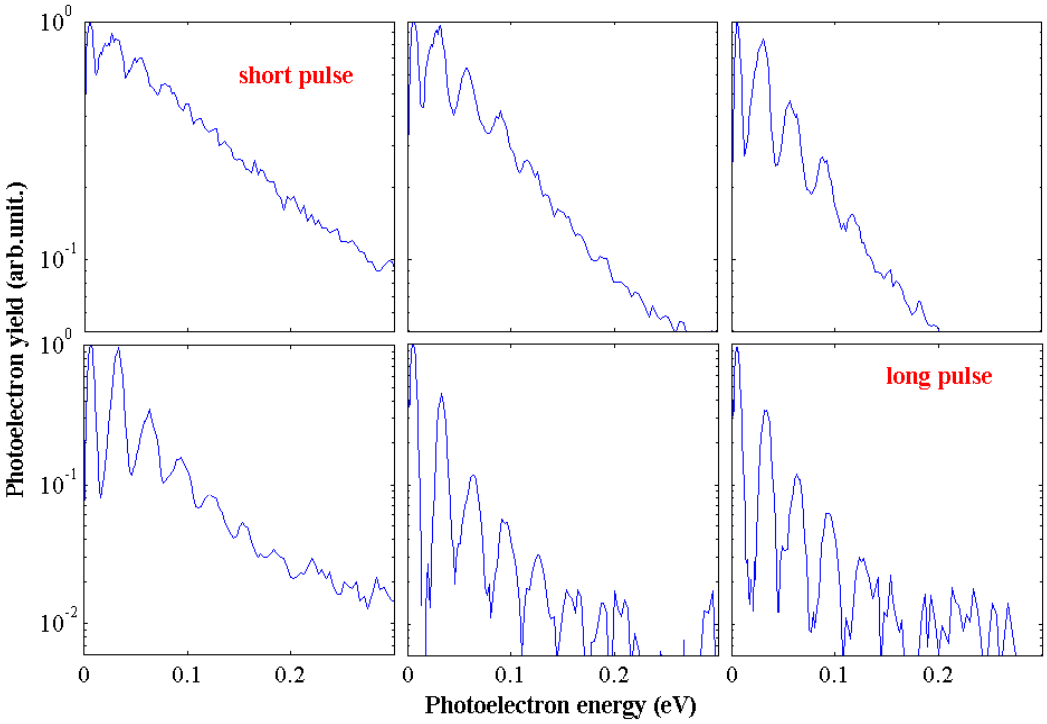

Figure 4.5: Corresponding angle-integrated photoelectron spectra for the measurements shown in Figure 4.4, where Xenon $10s$ state was ionized by $42\mu m$ laser pulses. The bandwidth of the pulse varies $\Delta E/E \approx 1.6\%$ (short pulse) in the top-left image to $\Delta E/E \approx 0.4\%$ (long pulse) in the bottom-right image. The pulse energies were typically around $10\mu J/pulse$. Note the different vertical scale for the upper and lower plots.

In the measurements a number of interesting changes can be observed as a function of the laser pulse duration: first, for increasing pulse duration the highest experimentally observed photoelectron kinetic energies are reduced; secondly, at the shortest pulse duration the photoelectron angular distribution aligns itself along the laser polarization axis; thirdly, at the shortest pulse duration the photoelectron peaks are hardly resolved anymore. In combination with the fact that the variation of the pulse duration moves the experiment from a regime where $\gamma > 1$ (long pulse) to a regime where $\gamma < 1$ (short pulse), we tentatively assign the observed changes in terms of a transition from multi-photon ionization to field ionization.

In addition to the aligning of the photoelectron angular distribution to the laser polarization axis, the measurements shown in Figure 4.4 contain very interesting angular distributions for the lowest order ATI peaks.

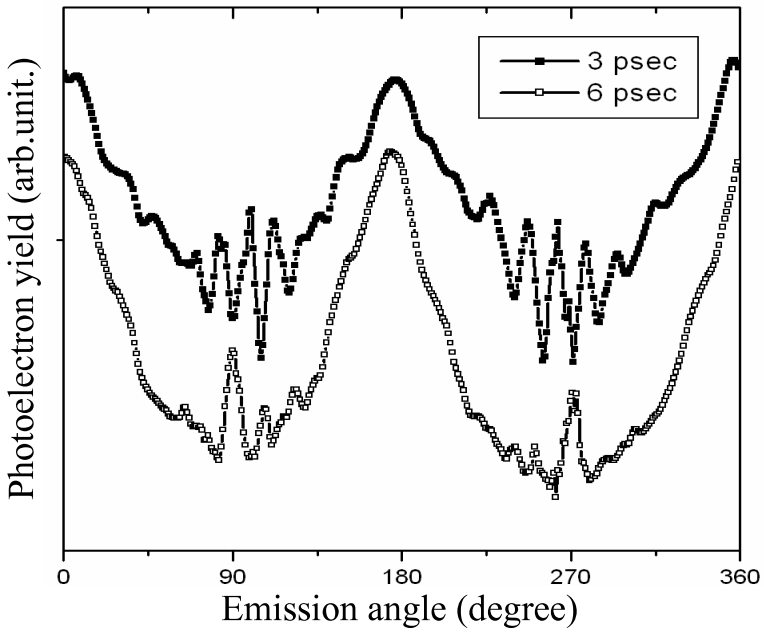

Figure 4.6: Rapid oscillations in the angular distribution recorded for ionization of the Xenon $10s$ state by $42\mu m$ free electron laser pulses with a duration of appr. 3 and 6 ps. The oscillations may be due to interferences between electron wavepackets that are formed during different half-cycles of the free electron laser pulse.

This feature is further illustrated in Figure 4.6, where the angular distribution of the second ATI peak is shown for the top-middle and bottom-middle measurement in Figure 4.4. These angular distributions display some highly unusual features: in the shorter pulse case (pulse duration roughly around $3ps$) the angular distribution contains 5 or 6 rapid oscillations between 0 and 180 degrees, whereas in the longer pulse measurement (pulse duration roughly around $6ps$) the angular distribution displays a prominent feature at 90 degrees with respect to the laser polarization axis.

In the literature there exist several examples of high-order oscillations in the angular distributions of ATI electrons. Helm and co-workers have interpreted rapid oscillations in the ATI of Xenon atoms at $800nm$ in terms of resonant population of AC Stark-shifted high-l Rydberg states in the ionization process [151]. Recently, Burgdörfer and co-workers have suggested that these type of rapid oscillations may be due to Rammsauer-Townsend interferences, where ATI electrons that tunnel-ionize during consecutive half-cycles of the IR laser field interfere [152]. In other words, in this description there would be no role for the

occurrence of resonances.

The interference explanation is appealing in the present context, since in an interference experiment we can readily imagine that the interference pattern changes when the number of contributing electron wave packets (each corresponding to a *slit* [153] in the experiment) varies, while conversely, in the case of a resonant multi-photon ionization process we do not anticipate dramatic changes in the interference pattern as a function of the pulse duration.

Dependence of the above-threshold ionization of Xenon on the initial Rydberg state

In the following experiment, we compare the ionization from a range of different initial Xenon Rydberg states.

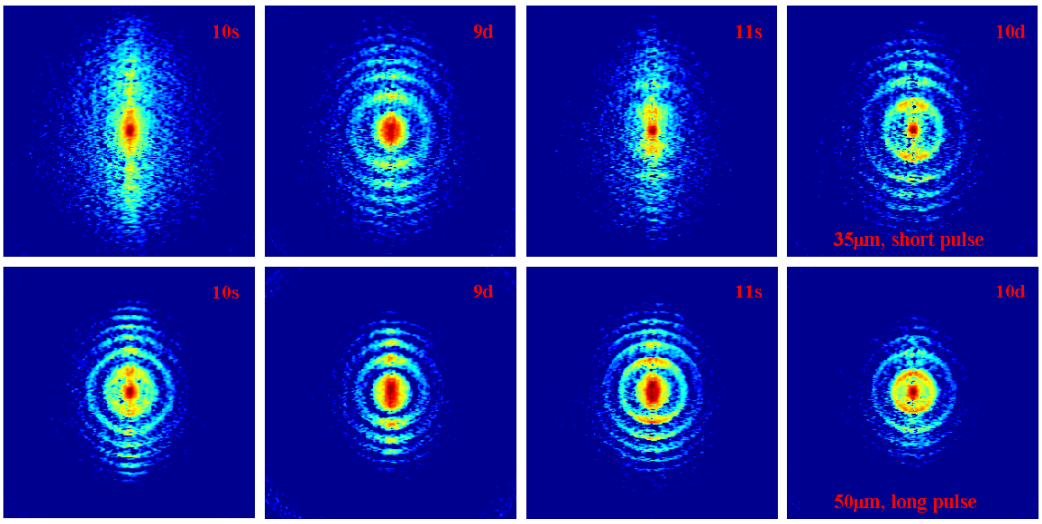

Figure 4.7: Inverted images of above-threshold ionization of Xenon ns and nd states ionized by $35\mu m$ short($\Delta E/E \approx 1.6\%$) and $50\mu m$($\Delta E/E \approx 0.4\%$) long free electron laser pulses. The pulse energies were typically around $10\mu J/pulse$.

Shown in Figure 4.7 are measurements for ionization of the Xenon *10s, 9d, 11s* and *10d* states with free electron laser pulses at two different wavelengths $35\mu m$ and $50\mu m$. The bandwidth for the pulses at $35\mu m$ and $50\mu m$ were approximately $\Delta E/E \approx 1.6\%$ and $\Delta E/E \approx 0.4\%$ respectively. This leads to relatively short pulses at $35\mu m$ and relatively long pulses at $50\mu m$. The striking feature in these measurements is that the angular distributions are strongly aligned along the laser polarization axis when the initial state is an s-orbital, and stay relatively broad when the initial state is a d-orbital.

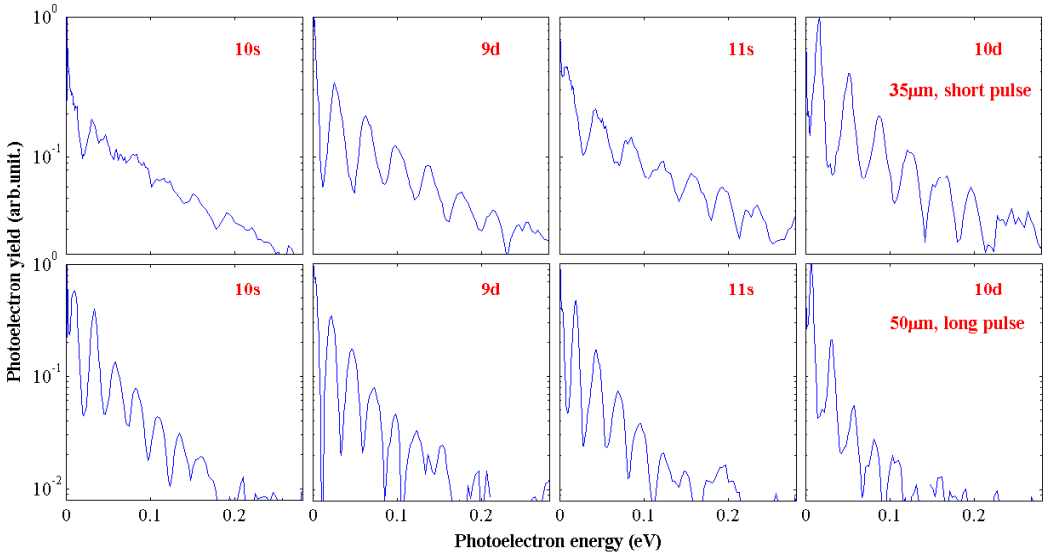

Figure 4.8: Corresponding angle-integrated photoelectron spectra for the measurements shown in Figure 4.7, where Xenon ns and nd state were ionized by $35\mu m$ short and $50\mu m$ long free electron laser pulses. The pulse energies were typically around $10\mu J/pulse$.

Given that all these experiments were performed under the same laser conditions and that the energy of the Xenon $9d$ state lies between Xenon $10s$ and Xenon $11s$ states, these measurements suggest that the strong field ionization is sensitive to the initial angular momentum of the Rydberg orbital. While a strong dependence of the ionization process on initial orbital is part of field ionization theories like ADK, it is much less clear whether the strongly aligned photoelectron angular distributions for experiments starting from a Xenon ns orbital can readily be explained in a multi-photon ionization picture.

Indeed, when we increase the Keldysh parameter by lengthening the laser pulse and lowering the peak intensity in the experiment, the difference between Xenon ns and nd states almost disappeared, as illustrated in the second line of images in Figure 4.7. Note that the laser wavelength was also increased from $35\mu m$ to $50\mu m$.

Figure 4.8 shows corresponding photoelectron spectra for the measurements shown in Figure 4.7. In these spectra it is clearly observed that for high initial state energy the ATI peaks are well resolved, whereas for low initial state energy the photoelectron peaks are much less well resolved. As before, these observations are consistent with a transition from the field ionization to the multi-photon regime when the initial state energy is increased. This transition is in contrast to

the fact that the Keldysh parameter γ actually becomes smaller when the initial state energy is increased. We consider that these observations are due to the fact that for highly excited initial states a substantial part of the ionization, which involves less photons than lower states, occurs well before the laser reaches its maximum intensity. Consistent with the observation in the changes of photoelectron angular distribution, the peak-valley contrast of the photoelectron spectra for nd states is more clear than of ns states for the $35\mu m$ case, while in the $50\mu m$ case there is no observable difference for ns and nd states.

4.3 Indirect Above-threshold ionization in the presence of DC field

In conventional strong field ionization the role of external DC electric fields is negligible, since the ionization of ground state atoms and molecules with ionization potential around $0.5a.u.(= 13.6eV)$ involves the use of laser fields as strong as $F_{laser} = 0.1a.u. = 5 \times 10^8 V/cm$ at the wavelength of the commonly-used $800nm$ Ti:Sapphire laser ($\omega = 0.057a.u.$), whereas in our two-dimensional imaging experiment the DC electric field that is used to project photoelectrons typically has a field strength of $F_{dc} \sim 10^{-7}a.u.$. This situation dramatically changes when strong field experiments are carried out using weakly-bound electronic states and far-infrared laser pulses. We first note that we expect that for weakly-bound electronic states tunnel ionization will not be important, since the width of the barrier in the combined Coulomb-laser field potential increases with decreasing electron binding energy. Rather, an upper limit to the laser field strength required for ionization is given by the threshold electric field for over the barrier ionization $F_{th} = I_p^2/4$. ATI spectra are then anticipated extending to an energy $2U_p = F_{th}^2/2\omega^2 = I_p^4/32\omega^2$. It follows that at far infrared wavelengths the number of ATI rings will be similar to that encountered with ground state atoms in the optical domain as long as the ratio I_p^4/ω^3 is held constant. If we consider ionization at a wavelength of $108\mu m(\omega = 4.2 \times 10^{-4}a.u.)$, and accordingly scale the initial state of the Xenon atom from its ground state energy to $1.1 \times 10^{-2}a.u.$, we arrive at a situation where the threshold laser field F_{th} for over the barrier ionization is approximately $3 \times 10^{-5}a.u.$. This being an upper limit, we may anticipate that the ionization dynamics can be affected by the presence of a $10^{-7}a.u$ external DC electric field, as was the case in the experiment.

Figure 4.9 shows selected images, along with radial distributions that were obtained by angular integration, for a series of experiments where Xenon Rydberg states were prepared close to the saddle-point in the combined Coulomb-DC field

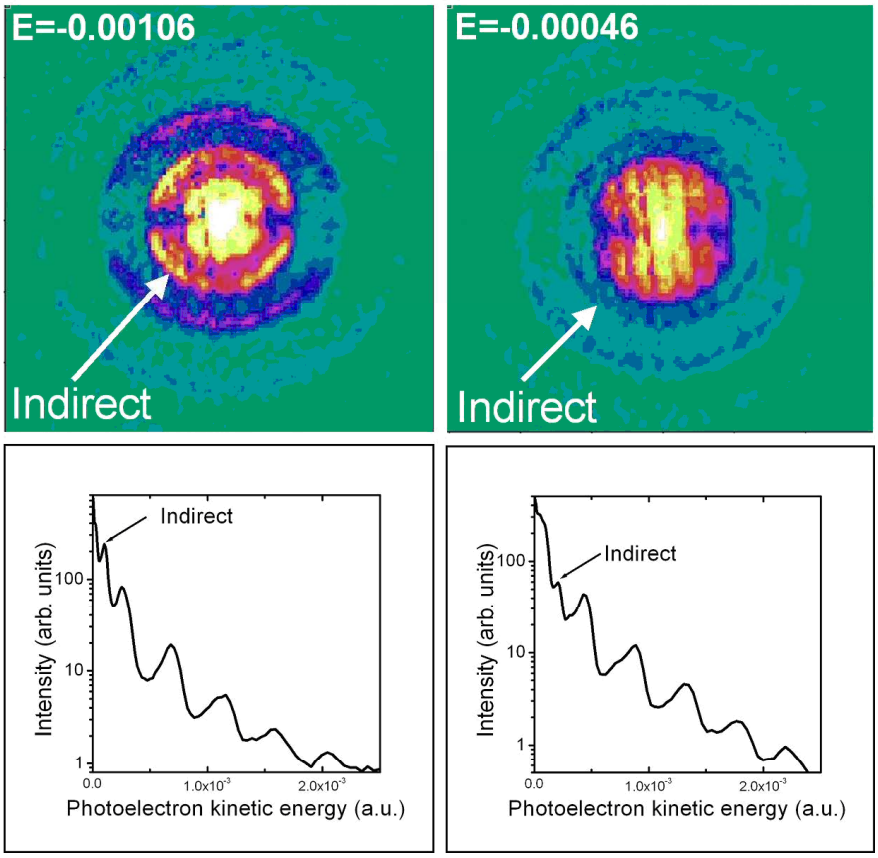

Figure 4.9: Recorded 2D images for ionization of Xenon Rydberg states lying at energies of -0.00106 and $-0.00046 a.u.$ with respect to the field-free ionization limit by $108 \mu m$ free electron laser pulses. Also shown are apparent photoelectron kinetic energy distributions derived from the 2D images, which shows a regular structure of ATI peaks, as well as an additional peak due to electron-ion re-collision.

potential, and ionized using $108 \mu m$ free electron laser pulses. Using the fact that the image represents a measurement of the velocity of the electron in the plane of the detector, the radial distributions are plotted as a function of the apparent kinetic energy corresponding to a given radius on the detector. A series of regularly spaced peaks separated by the $108 \mu m$ free electron laser photon energy ($\omega = 4.210^{-4} a.u.$) are observed and identified as ATI peaks.

Remarkably, the distributions show an additional peak (indicated by an arrow) between the lowest-order photoelectron peak and the first ATI peak. We will argue that this peak is the result of an electron-ion re-collision under the influence of the DC electric field in the experiment. Consequently, the radial

distributions shown in the lower two plots in Figure 4.9 cannot truly be viewed as measurements of the kinetic energy distribution of the emitted photoelectrons, but are apparent kinetic energy distributions under the assumption of a cylindrically symmetric photoelectron emission.

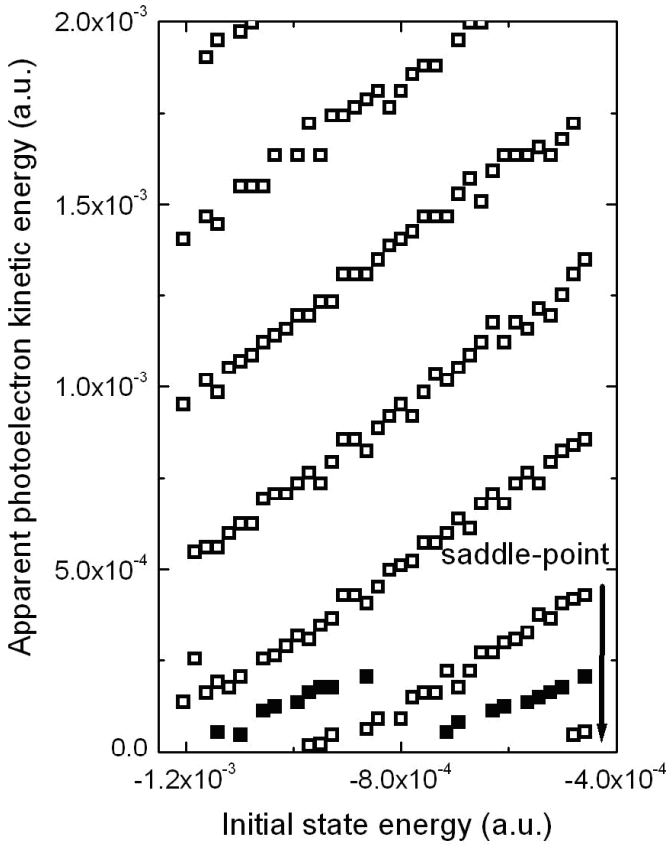

Figure 4.10: Apparent photoelectron kinetic energies of the emitted photoelectrons as a function of the energy of the initial state that is prepared by the dye laser. Open squares correspond to peaks that lie an integer number of photons above the initial Rydberg state, whereas closed squares correspond to additional peaks that are due to the influence of the Coulomb and DC fields on the trajectory of the electron.

In Figure 4.10, the positions of observed peaks in the radial distributions of the emitted photoelectrons are shown as a function of the energy of the initial state prepared by tuning the dye laser. If the atom is prepared at an energy that is an integral number N photons below the saddle point in the combined Coulomb-DC electric field potential, then ionization by absorption of N photons leads to the production of a photoelectron with zero excess kinetic energy, while

absorption of S additional photons leads to the production of photoelectrons with a kinetic energy $S\hbar\omega$. An increase in the initial state energy leads to a similar shift in the photoelectron spectrum, and as a result photoelectron peaks are expected at energies $(N+S)\hbar\omega + E_{init} - E_{sp}$, where E_{init} and E_{sp} are the energy of the initial state and the saddle point. In this fashion, 5 ATI branches are experimentally observed in the initial state energy range shown in Figure 4.10 (open squares). Additional rings (solid squares) appear at apparent photoelectron kinetic energies that cannot be understood on the basis of the initial state energy, the photon energy and the saddle point energy. These rings are reminiscent of observations that were previously made at AMOLF [154, 155] and occur since the combination of the Coulomb interaction, the interaction with the laser field F_{laser} and the interaction with the DC electric field F_{dc} leads to a re-collision of the electron with the parent ionic core that changes the asymptotic velocity of the photoelectron.

This observation is remarkable for several reasons. For an initial state that lies at one photon energy below the saddle point, the Keldysh parameter drops below 1 for field strength above $(2\omega^3)^{1/2} = 1.2 \times 10^{-5} a.u.$, suggesting, at first sight, that under the experimental conditions the role of field ionization might be non-negligible. However, the observation of an indirect ionization process where the electron trajectory is strongly influenced by the combination of the DC electric field and the Coulomb field suggests that the laser field fails to drive the electron away significantly from its parent ionic core and is seemingly more compatible with a multi-photon ionization picture. Indeed, as we have observed previously, in our discussion of Figure 4.2 and Figure 4.3, at longer free electron laser wavelengths the ionization process moves more and more into the multi-photon regime, since the focused laser intensity drops off more rapidly (with λ^{-3}) than the increase in the ponderomotive energy due to its λ^2 scaling.

4.4 Summary and future work

Above-threshold ionization of Xenon Rydberg states with far-infrared free electron laser pulses have been successfully performed over a wide range of different laser wavelengths, different pulse durations and from different initial Rydberg states. This implies that there exists indeed the possibilities to probe atomic ionization dynamics with femtosecond laser pulses that are readily available in many laser labs.

In this study, measurements were performed mainly in the multi-photon ionization regime. When the laser wavelength is increased the experiments move

more towards the multi-photon regime due to the fast drop of the focused peak laser intensity that is wavelength dependent. Photoelectrons are observed to be preferentially aligned along the laser polarization axis when Xenon s states are ionized with free electron laser pulses of short pulse durations and short wavelengths. This seems to suggest a transition to a field ionization regime. Furthermore, measurements over a series of initial s and d Rydberg states show a consistent difference in the photoelectron angular distribution between s and d states, even when the measurements are performed with the same laser pulses. We also observed that electrons with very low kinetic energy may come back and rescatter off their parents ionic cores, leading to an extra peak in the photoelectron kinetic energy spectra. In order to better understand the observations made in these measurements, calculations by solving the time-dependent Schrödinger equation are currently in progress.

Chapter 5

A 2D study of above-threshold ionization by few-cycle infrared laser pulses

Start-of-the-art ultrashort technology has made it possible to control the carrier-envelope phase of the laser electric field. This opens a new way to study and control the electron dynamics in strong field ionization processes. With the help of a velocity-map imaging photoelectron spectrometer, we have been able, for the first time, to measure the full photoelectron angular distribution in the whole photoelectron kinetic energy range. Above-threshold ionization of rare gas atoms by few-cycle infrared laser pulses indeed shows very interesting features that have never been measured before. This may allow us to deepen our understanding on the strong field ionization process, and the role of electron recollision with the parent ionic core, which lies at the basis of attosecond laser pulse generation.

5.1 Introduction

As we have discussed in Chapter 1, above-threshold ionization of rare gas atoms has been studied very intensively during the last several decades. Freeman *et al* have realized that sharp structures that are independent of the laser intensity are due to resonances through high-l Rydberg states. Paulus *et al* [30] and Walker *et al* [156] have observed an extended plateau where the electron energy extend above $2U_p$ and reaches $10U_p$. This plateau has been understood as being due to the recollision of ionized electrons with the parent ionic core. Paulus *et al* have also performed above-threshold ionization with few-cycle infrared laser pulses. Their recent work on the above-threshold ionization with phase-stabilized few-cycle pulses has shown that electrons are not ejected equally towards two directions along the laser polarization [157]. By varying the carrier-envelope phase, electron emission can be steered from one side to the other. This asymmetry of ionization can be used as a way to determine the carrier-envelope phase.

Interesting angular distributions of ejected electrons have been measured with the help of imaging spectrometers. Helm *et al* first introduced the photoelectron imaging spectrometer technique into atomic photoionization experiments. Their work has clearly shown the signature of high Rydberg states through which atoms are resonantly ionized [151]. Van Woerkom *et al* have also studied the angular distribution of electrons in the lower energy region in detail [158]. The only angular distribution measurement in the high energy plateau region, to the best of our knowledge, was performed by DiMauro *et al* [28]. They observed that electrons were ejected at 45 degrees with respect to the laser polarization axis in the plateau region or more specifically around $8U_p$. These electrons are believed to be due to a recollision process. However, there is no exact explanation in the literature explaining how the recollision process leads to this particular angular distribution in the plateau region.

In our experiment, a velocity-map imaging photoelectron spectrometer was used to study above-threshold ionization by carrier-envelope phase-stabilized laser pulses. The velocity-map imaging spectrometer allows to simultaneously measure the photoelectron spectrum and the angular distribution. Apart from the up-down asymmetry along the laser polarization depending on the carrier-envelope phase, we also observed electrons ejected at fixed angles which are different from the previously reported angle of 45 degrees in the plateau region.

5.2 Experiment setup

The experiment was performed with a $3KHz$ Ti:Sapphire laser in the group of Krausz in the Max-Planck Institute for Quantum Optics in Garching. The carrier-envelope phase of the output pulses was stabilized through a feedback control loop [139]. The focused laser intensity was around $1 \times 10^{14} W/cm^2$. The pulse duration could be varied from $5fs$ to $20fs$ by changing the gas pressure in a hollow-core fiber which is used to broaden the spectra of the laser pulses. The laser pulses were focused into the interaction region of a velocity-map imaging photoelectron spectrometer to ionize rare gas atoms. Electrons were then accelerated towards a MCP+Phosphor screen detector assembly. A 2D image was recorded by a CCD camera system.

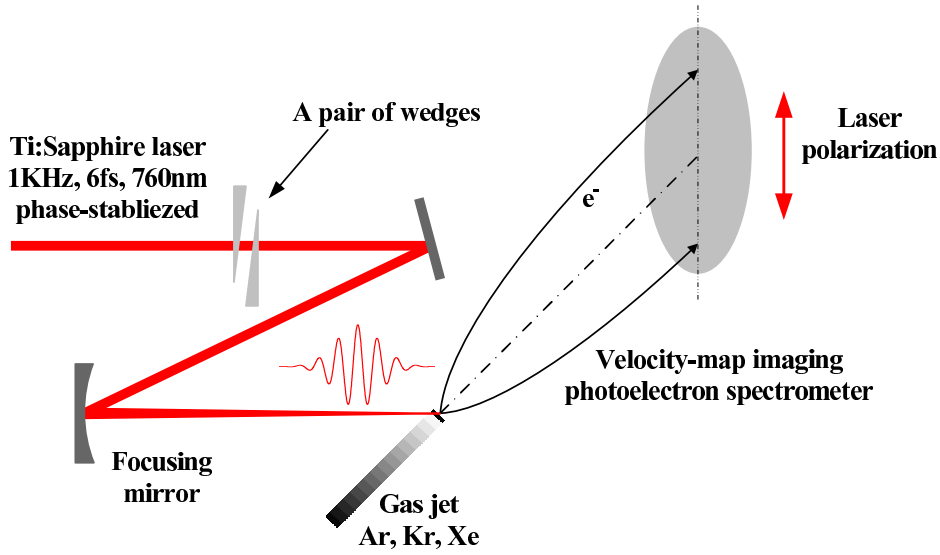

Figure 5.1: Experimental Scheme. Phase-stabilized few-cycle laser pulses are focused by a concave mirror to ionize rare gas atoms in the interaction region of a velocity-map imaging photoelectron spectrometer. The gas is supplied with a $50Hz$ valve, thus only one out of sixty pulses are used to ionize the atoms. A pair of two thin glass wedges(apex angle 2.8^o) is used to control the carrier-envelope phase. The laser polarization is shown in the figure as vertical. Electrons are accelerated towards the detector assembly, and a 2D image is recorded with a CCD camera system.

A pair of glass wedges was used to change the carrier-envelope phase. The wedges were inserted with a certain angle into the laser beam. A 2π phase shift roughly correspond to $2mm$ movement of one wedge. If we describe the laser field as $E = E_0 cos(\omega t + \phi)$, a cosine-like pulse is defined with $\phi = 0$. The laser

polarization was vertical and parallel to the plane of the detector as shown in Figure 5.1. It was the same for all the images shown in this chapter.

5.3 Carrier-envelope phase dependence

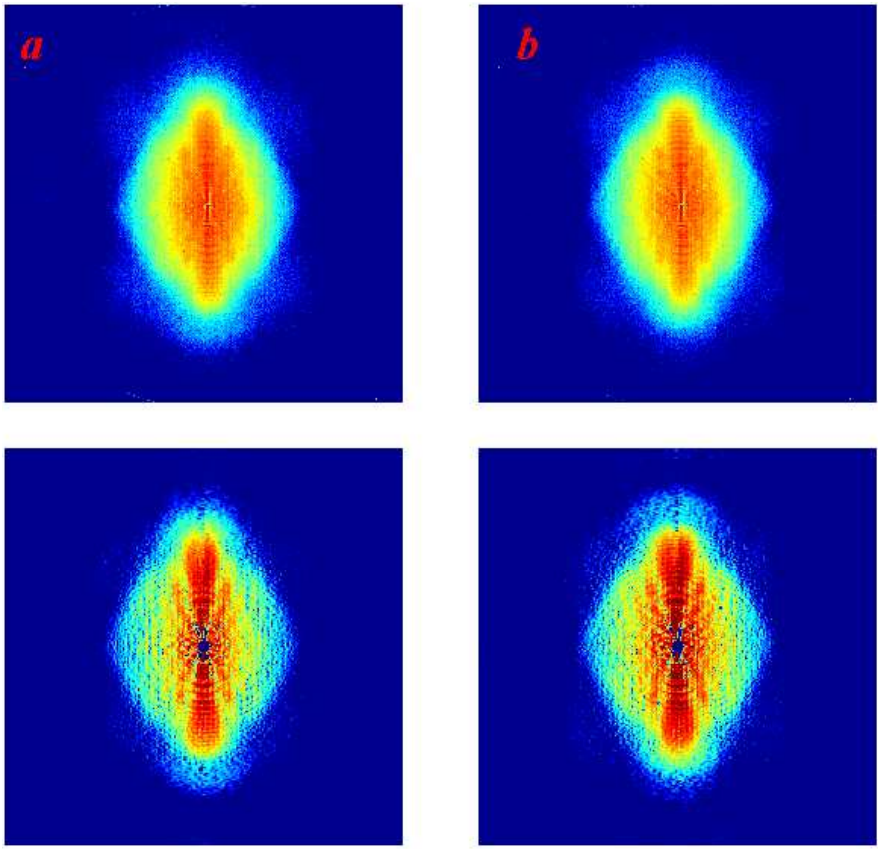

Figure 5.2: Recorded raw images for ionization of Argon atoms by $6fs$ laser pulses with a peak intensities around $1.2 \times 10^{14} W/cm^2$. The measurements were performed at two extreme cases: $\phi = 0(\boldsymbol{a})$ and $\phi = \pi(\boldsymbol{b})$. Fringes can be seen in the lower part of $\boldsymbol{a}$ and upper part of $\boldsymbol{b}$. Shown in bottom part of the figure below two raw images are 2D slices through the reconstructed 3D distributions. The angular structure in the central part of the images, as well as the fringes, are believed to be due to the interference of electrons created from different half-cycles of the laser field.

Argon atoms were ionized by $6fs$ laser pulses with a peak intensity close to $1.2 \times 10^{14} W/cm^2$. At this intensity, U_p is about $6.4eV$. Figure 5.2 presents images at two specific carrier-envelope phases,namely $\phi = 0$ and $\phi = \pi$. 2D projections

of the 3D velocity distribution are shown in the upper two images marked a and b. 2D slices through the reconstructed 3D velocity distributions are shown in the lower part.

It is not very obvious that there is an up-down asymmetry from these images. However, in Figure 5.2 ***a***, interference fringes can be seen in the lower part of the image, close to the cutoff region of the photoelectron spectrum. In Figure 5.2 ***b***, this sharp structure appears in the upper part of the image. This is an indication of a π phase change from a cosine-like pulse with the field maximum pointing towards one side along the laser polarization to a cosine-like pulse with the field maximum pointing in the opposite direction.

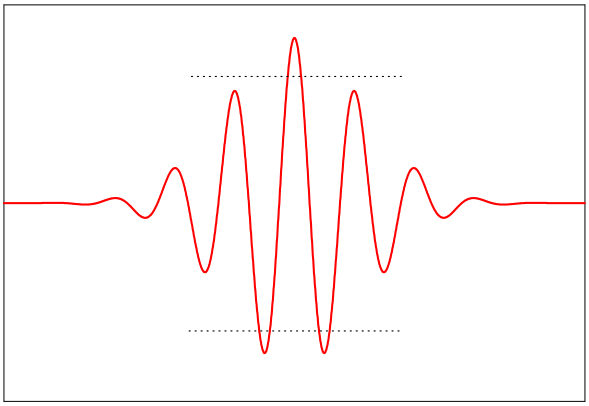

Figure 5.3: Shown in red is a few-cycle laser pulse with a carrier-envelope phase $\phi = 0$. Dotted line shows a threshold above which electrons will be ionized by the laser field, thus creating three electron wavepackets with 1 in upper direction and 2 in the opposite direction. Interference will occur between the two electron wavepackets ejected downwards.

We have discussed in previous chapters that above-threshold ionization is a highly nonlinear process. Electrons are ionized only when the optical field reaches a threshold amplitude. For the pulse shown in Figure 5.3, electrons are created mainly by three half-cycles in the central part of the pulse, thus producing three electron wavepackets, one in the upper part of the image and two in the lower part. The two wavepackets in the lower part acquire a phase difference in the laser field due to their different ionization timing. They will interfere with each other and an interference pattern is then recorded by the detector. Note that interferences will occur only when electrons have the same momentum. The first and third ionization peak create electrons with momenta close to the cut-off region. This explains the observation of these interference fringes close to the cutoff region, but not in the cut-off region.

Figure 5.4 presents photoelectron spectra for $\phi = 0$ and $\phi = \pi$. Electrons

emitted upwards and downwards are separately shown. An up-down asymmetry is clear around $40eV$ which is well into the plateau region of the spectra.

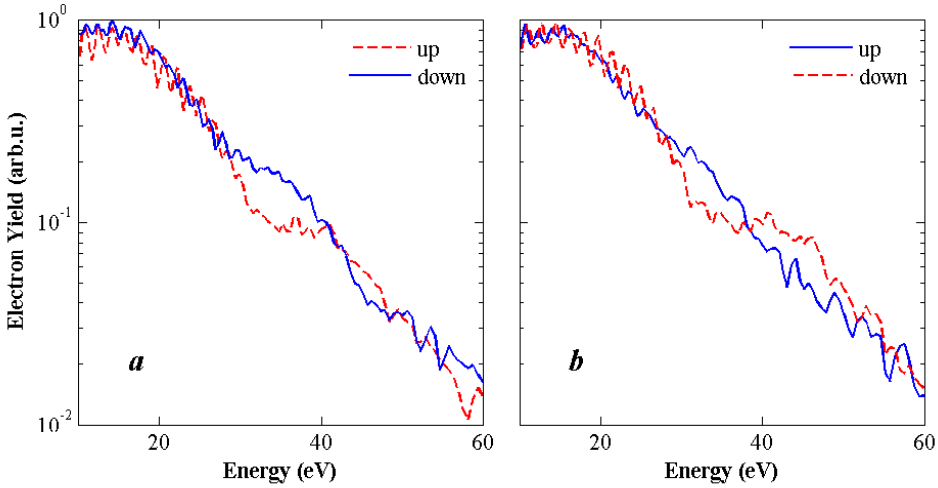

Figure 5.4: Normalized photoelectron spectra of the measurement shown in Figure 5.2 where Argon atoms were ionized by a $6fs$ laser pulses with peak intensity around $1.2 \times 10^{14} W/cm^2$ at $\phi = 0(\boldsymbol{a})$ and $\phi = \pi(\boldsymbol{b})$, integrated over 20 degree around the laser polarization.

To investigate the phase dependence of the electron emission process, an energy dependent asymmetry factor is defined as $(P_{up}(E) - P_{down}(E))/(P_{up}(E) - P_{down}(E))$, where $P_{up}(E)$ and $P_{down}(E)$ are the angle-integrated energy spectra of electrons emitted upwards and downwards respectively. Figure 5.4 compares the experimental up-down asymmetry plot with a calculation by numerically solving the time-dependent Schrödinger equation within the single-active electron approximation. The parameters used in the calculation are an $8fs$ pulse with a central wavelength of $800nm$ and a peak intensity of $1 \times 10^{14} W/cm^2$. The integration angle for the experiment and calculation are 20^o and 18^o. Although the parameters chosen for the calculation are slightly different from the experiment, the calculation results resemble the experimental results very well.

Clearly, the higher energy part ($> 2U_p, U_p = 6.4eV$) of the photoelectron spectra, namely the plateau region, shows higher sensitivity to the carrier-envelope phase. This again reflects the strong dependence of the ionization process on the optical field of the few-cycle laser pulses. As we have discussed in the last page, high energy electrons are mainly created by half-cycles very close to the field maximum. The final kinetic energy of the ejected electron depends on the initial kinetic energy upon recolliding and the acceleration following the recollision, both requiring a high field strength. The difficulty to meet all these requirements

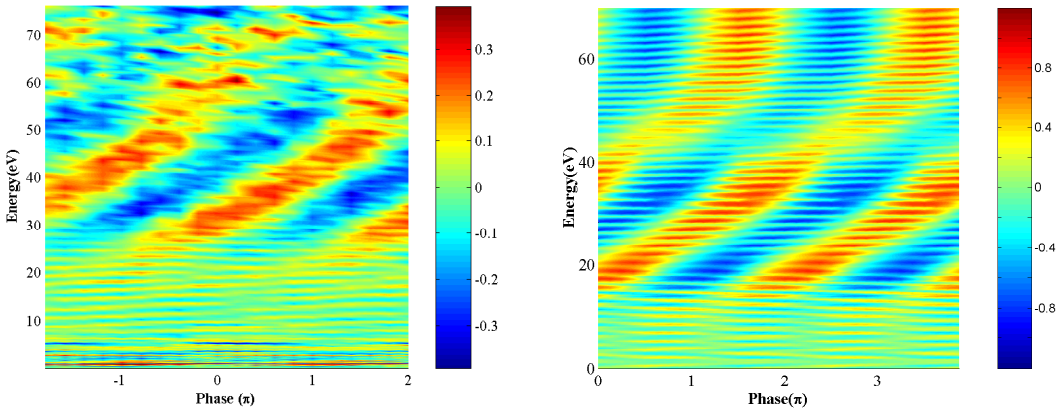

(a) Experiment (b) Calculation

Figure 5.5: Up-down asymmetry contourplot showing the asymmetry as a function of the carrier-envelope phase and the electron energy, for both experiment (a) and calculation (b). The experiment parameters are the same as in Figure 5.2, i.e. $6fs$ and $1.2 \times 10^{14} W/cm^2$, while in the calculation $8fs$ laser pulses with peak intensity of $1 \times 10^{14} W/cm^2$ are used. The fact that the calculation with these parameters reproduces better the experimental results implies there might be some errors in estimating the experimental parameters.

leads to the significant asymmetry dependence of the plateau electrons on the carrier-envelope phase [39].

The clear phase shift of the asymmetry as a function of carrier-envelope phase in the lower and higher energy part of Figure 5.5 may be used to uniquely determine the value of the carrier-envelope phase. A single shot measurement may be able to determine the carrier-envelope phase.

5.4 Angular distributions

According to the semi-classical theory, electrons created through the process of above-threshold ionization can be divided into two different types. Electrons that are directly emitted have a kinetic energy below $2U_p$. Electrons that are rescattered off the ionic core may have kinetic energy from $2U_p$ to $10U_p$ depending on their phases when they return to the ionic core [159]. These electrons form a second plateau region in the photoelectron spectrum. The effect of different trajectories that electrons follow when they leave the ionic core or when they return and rescatter off the ionic core are manifested not only on the extension of the photoelectron spectrum up to $10U_p$ but also in the angular distributions of the

electrons. With a velocity-map imaging spectrometer one can measure the photoelectron spectrum and the photoelectron angular distribution simultaneously.

In the following, we will discuss detailed measurements on the angular distribution of the electrons during the above-threshold ionization process in Xenon, Argon and Krypton with non-phase-stabilized infrared laser pulses. As before, the laser polarization is vertical in the plane of the paper. The laser peak intensity is estimated from the classical $10U_p$ cutoff in the photoelectron spectrum along the laser polarization axis and by comparing previous reported results by Paulus *et al.*

Xenon

Results for above-threshold ionization of Xenon using $25fs$ long pulses are presented in Figure 5.6. The estimated peak intensity was $9.3 \times 10^{13} W/cm^2$, thus $U_p = 5eV$. The slight asymmetry along the 0^o and 180^o direction is due to the nonlinear detection efficiency of the old MCP detector that was used in the experiment.

Four different energy regions with qualitatively different angular features can be clearly distinguished. First, the low energy part, up to $2U_p = 10eV$. This region contains a complex structure in the photoelectron velocity and angular distribution. Second, a medium energy part, from $10eV$ to $20eV$. Electrons in this region appear to be emitted not only around the laser polarization axis but also around 60^o with respect to the vertical laser polarization. Thirdly, a medium-high energy part, from $20eV$ to $30eV$, where electrons appear to be emitted along the laser polarization axis and around 30^o with respect to the laser polarization axis. Lastly, the highest energy part, above $30eV$. In this region electrons are emitted solely along the laser polarization.

Figure 5.7 plots the angular distributions for selected photoelectron energies within the above discussed four different energy regions. The angular distribution is plotted from 0^o to 360^o starting from the upper direction of the laser polarization.

Photoelectron spectra as a function of the emission angle are shown in Figure 5.6 ***c***. Well-know ATI peaks separated by one infrared photon energy can be clearly seen in the plateau region. The complex angular structures in the lower energy region might be due to the interference between electron wavepackets that are created at different half cycles of the laser field. We have discussed a similar effect in previous Chapter. (See Figure 4.6 in Chapter 4.)

The angular features around 60^o and 30^o in this experiment seem to be an extension of the interference feature from the lower energy part to higher energies.

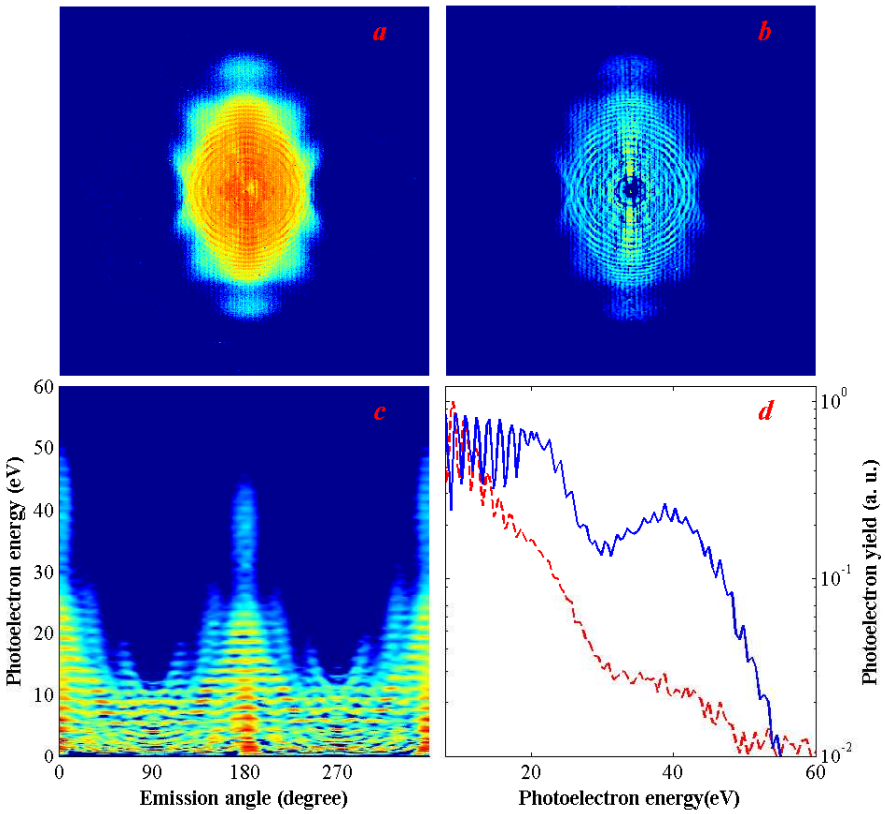

Figure 5.6: ***a*** Raw ATI image from Xenon ionized with a $25fs$ long pulse at an estimated intensity of $9.3 \times 10^{13} W/cm^2$. ***b*** 2D slice through the reconstructed 3D electron velocity distribution. ***c*** Photoelectron kinetic energy as a function of the emission angle with respect to the laser polarization. ***d*** Photoelectron spectrum integrated over all angles (dashed red line) and around zero degrees along the laser polarization (solid blue line).

Based on their energies, which are clearly above $2U_p$, we would suspect that these features might be the consequence of a recollision. In the present experiment electrons are created with almost zero kinetic energy through tunnel ionization or multi-photon ionization at low intensities. They may have chances to return and scatter off their parent ions depending on their trajectories which in turn depend on their moment of ionization.

Figure 5.8 presents the results from Xenon ionized by $6fs$ long pulses. The peak intensity was estimated to be $1.1 \times 10^{14} W/cm^2$. Very similar features are observed compared to the results with $25fs$ pulses. The interference structures in the lower energy part are not as sharp as in the $25fs$ case. This is probably because with longer pulses, more electron wavepackets are created over many

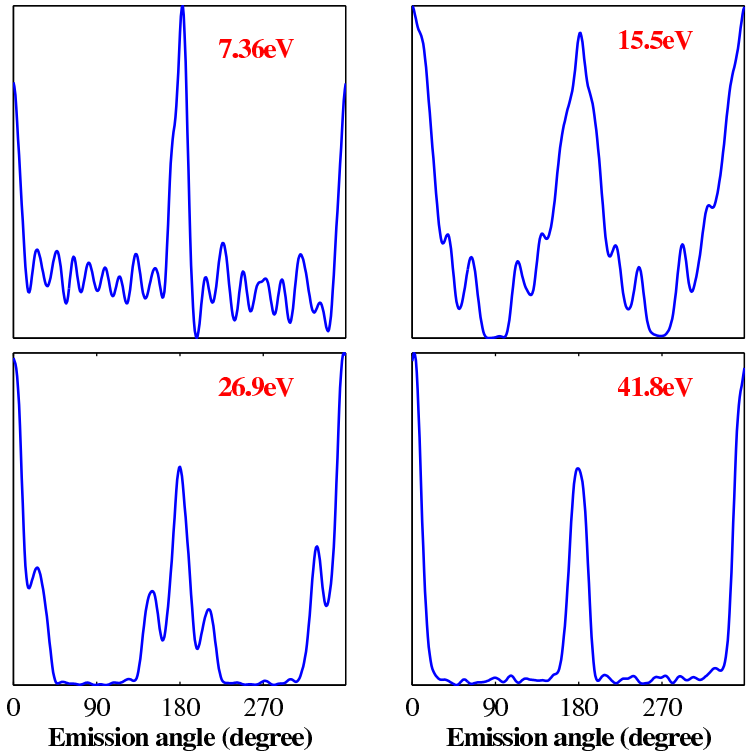

Figure 5.7: Angular distribution plots in 4 different energy regions for the images shown in Figure 5.6 (Xenon, long pulse). Note the features around 60^o with respect to the laser polarization axis at $15.5eV$ and at 30^o degrees with respect to the laser polarization axis at $26.9eV$ in the plots. The laser polarization is at 0^o and 180^o. Note that, high frequency noise in the angular plots shown in this section is Fourier-filtered out carefully only for visibility reasons. It has been checked that the filtering does not introduce extra features or remove significant features.

optical cycles, resembling a multi-slit interference in optics. By contrast, the field amplitude changes significantly from one cycle to the next when using few-cycle laser pulses. With a $6fs$ pulse, very few electron wavepackets can be created, and their properties are quite different due to the significantly different field strength.

The angular features around 60^o and 30^o are very well preserved in the $6fs$ results. However, careful inspection of Figure 5.8 ***c*** shows that the 30^ocontribution extends much further into the plateau region, up to $40eV$. Furthermore, it does not seem to be dependent on the electron energy, while the 60^o contribution does. This may indicate that these two contributions have different origins.

Plots of angular distributions at four selected photoelectron energy in different energy ranges are shown in Figure 5.9. A loss of the regular interference

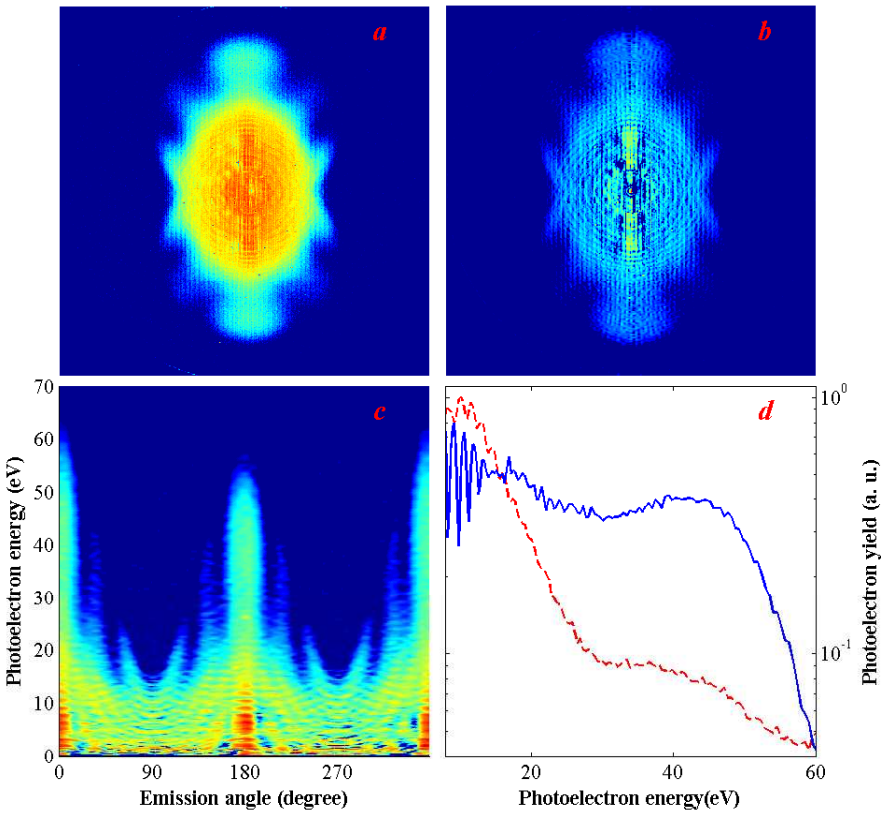

Figure 5.8: ***a*** Raw ATI image from Xenon ionized by $6fs$ long pulses at an estimated intensity of $1.1 \times 10^{14} W/cm^2$. ***b*** 2D slice through the reconstructed 3D electron velocity distribution. ***c*** Photoelectron kinetic energy as a function of the emission angle with respect to the laser polarization. ***d*** Photoelectron spectrum integrated over full angle (dashed red line) and around zero degree along the laser polarization (solid blue line). Note the extension of the stripes at 30^o in ***c*** comparing to with the same image in Figure 5.6.

structure in the lower energy part can be seen in the top-left plot in Figure 5.9 and Figure 5.7, which can be explained by the fact that the electron wavepackets involved in the interference in the $6fs$ case are very different from those in the $25fs$ case. Features around 60^o and 30^o stay almost unchanged, and small ripples around 30^o can be seen even at $41eV$.

Measurements on the above-threshold ionization of Xenon with $6fs$ laser pulses were performed over a range of pulse energies. An overview plot of the photoelectron kinetic energy as a function of the emission angle is presented in Figure 5.10. The estimated intensity increases from $6 \times 10^{13} W/cm^2$ in the top-left measurement to $1.2 \times 10^{14} W/cm^2$ in the bottom-right measurement. It can

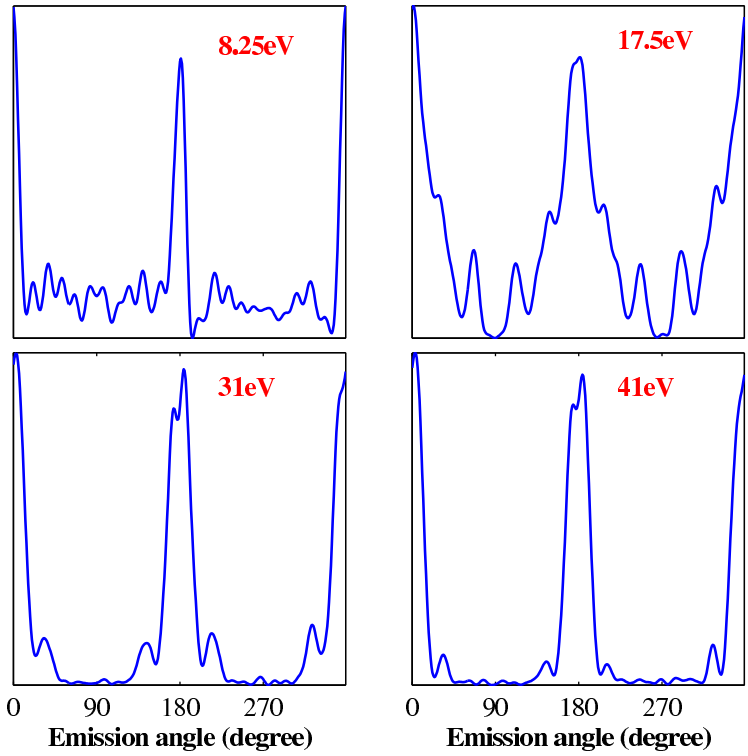

Figure 5.9: Angular distribution plots in 4 different energy regions in the images shown in Figure 5.8 (Xenon, short pulse). Similar features around 60^o and 30^o are well preserved compared to the long pulse case.

be clearly seen that the fringe spacings in the interference structures, depend strongly on the peak laser intensity, while the structures around 60^o and 30^o do not change too much when increasing the peak intensity.

As we have pointed out in the introduction part of this Chapter, Helm *et al* [151] have studied the angular dependence for above-threshold ionization of Xenon with $100fs$ $800nm$ laser pulses in an intensity range from $1.8\times10^{13}W/cm^2$ to $7.8\times10^{13}W/cm^2$. Similar structures have been observed in the low energy part in their experiment. Those structures have been explained by resonant ionization via high-l Rydberg states. Van Woerkom *et al* [158] have confirmed this explanation in their experiments performed with $110fs$ $800nm$ laser pulses with peak intensities up to $1\times10^{14}W/cm^2$ with an energy resolution of $25meV$, compared to $50meV$ resolution estimated in our measurements.

In their experiments, because of the long laser pulses used, Xenon atoms are mostly ionized by absorbing multiple infrared photons before the laser field reaches the maximum. However, in our experiments with extremely short laser

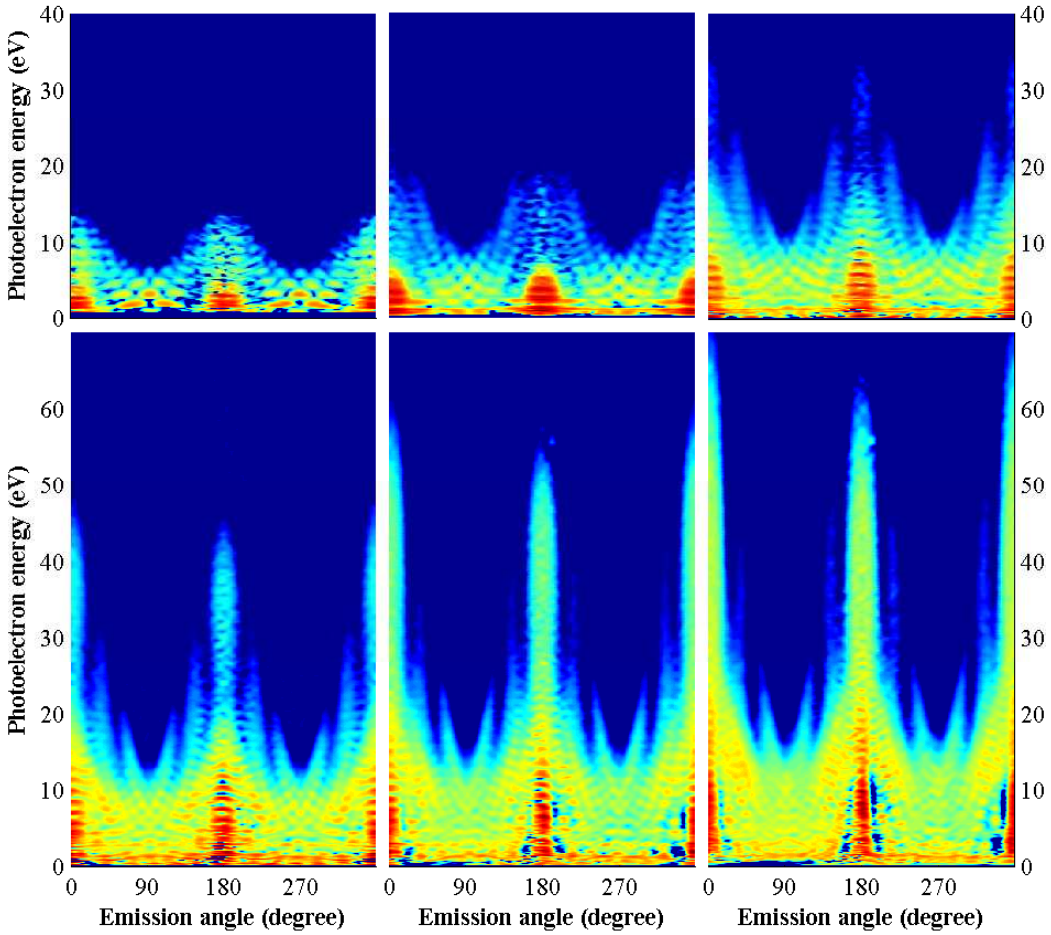

Figure 5.10: Photoelectron kinetic energy as a function of the emission angle with respect to the laser polarization for a series of different intensities. The estimated peak laser intensity varies from $6 \times 10^{13} W/cm^2$ in the top left measurement to $1.2 \times 10^{14} W/cm^2$ in the bottom right measurement. Note that the different photoelectron kinetic energy scales for the images shown in the top part are different from those shown in the bottom part.

pulses (especially the $6fs$ case), Xenon atoms are put into a strong laser field near the field maximum immediately or after one or two half-cycles. Thus most electrons are freed by tunnelling through or directly over the potential barrier that is formed by the external laser field and the Coulomb field of the ionic core. We have discussed in Chapter 1 on page 11 that over-the-barrier ionization of Xenon occurs at an intensity of $8.6 \times 10^{13} W/cm^2$. This is exactly the intensity range that we are working with in our measurements. Electron wavepackets with zero or very low initial kinetic energy are created in our experiments near the field

maxima. Different electron trajectories will then acquire different phases from their propagation in the laser field. The interference between the final electron wavepackets seems to be more applicable to our observation.

Neither Helm *et al* nor Van Woerkom *et al* have presented angular distributions at higher photoelectron energy. The maximum electron energy at which angular distributions were reported by Van Woerkom *et al* was about $10eV$, which is just in the beginning of the plateau region of their ATI spectra. The only angular measurement in the plateau region was done by Yang *et al* [28] with $50ps$ $1\mu m$ laser pulses at an intensity of $3 \times 10^{13} W/cm^2$. They observed electrons with an energy around $8U_p$ appearing at 45^o.

Although in a quite different experimental condition, we have observed electrons appearing around 60^o and 30^o in the plateau region. As we have mentioned, the 60^o contribution seems like an extension of the interference structure in the lower energy part, while the 30^o contribution might have a different origin, i.e. due to a recollision process. As can be seen in Figure 5.10, the 30^o contribution indeed grows with the plateau and the cutoff when increasing the peak intensity, while the others do not.

Since the recollision process strongly depends on the ionization time and the returning time of the electrons, further detailed carrier-envelope phase dependent investigation on the angular distribution would possibly reveal whether the electrons appearing at 30^o and 60^o are from the recollision process or not.

Argon and Krypton

Results from Argon and Krypton ionized with $25fs$ and $6fs$ pulses are summarized in Figure 5.11. The intensity in these measurements are difficult to estimate since the photoelectron energy spectra do not have a clear plateau or cutoff. And the results from Krypton with $25fs$ pulses were recorded accidentally at $1.6kV$ instead of $1.8kV$ applied to the micro-channel plate detector.

Similar angular structures were observed in both Argon and Krypton for both $25fs$ and $6fs$ cases, with qualitative difference from the results from Xenon. First, the structures in the lower energy part exhibit slower oscillations than the rapid oscillations observed in the Xenon results. Secondly, the results from Argon and Krypton have clear angular features perpendicular to the laser polarization, which is vertical in the plane of the paper. This feature tends to extend to the higher energy region. Thirdly, there is no clear 60^o and 30^o features in the higher energy region as observed in the Xenon results. This might be due to the fact that the recollision probability in the ionization process in Argon and Krypton is smaller than that of Xenon.

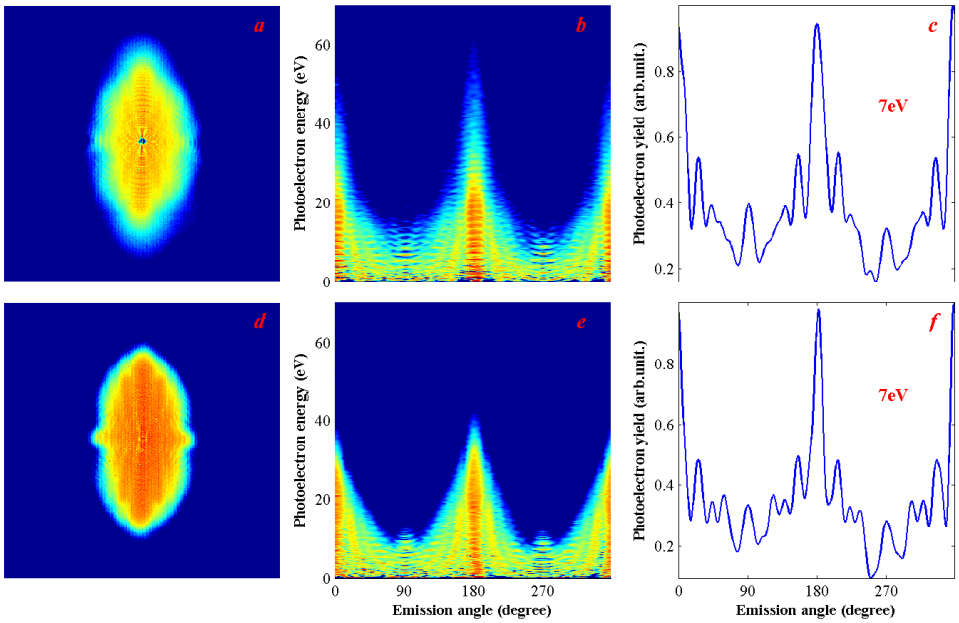

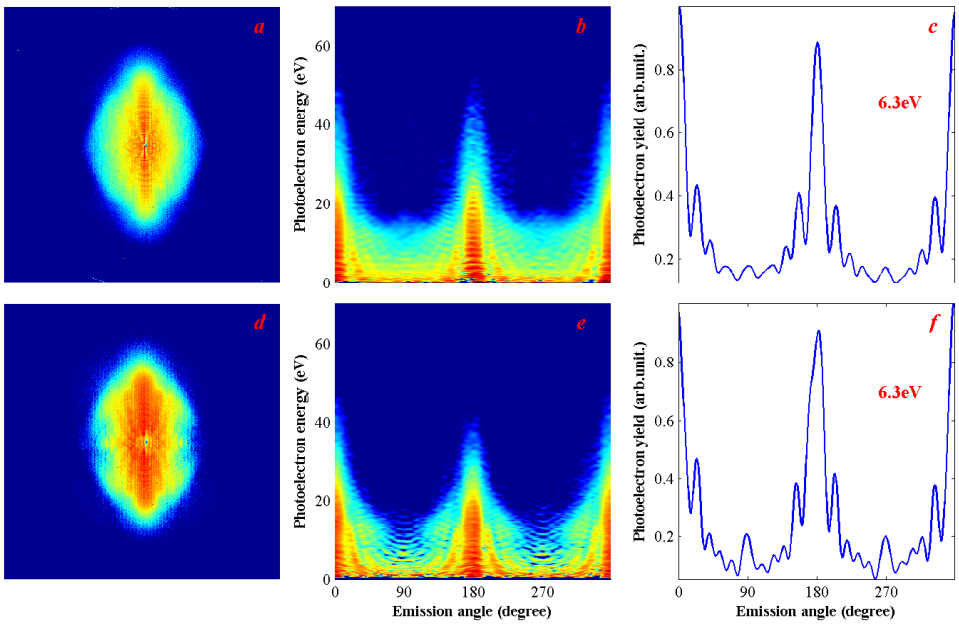

(B) Argon (***a, b, c***) and Krypton (***d, e, f***) results with $6fs$ pulses

Figure 5.11: Results for Argon and Krypton with $25fs$ (A) and $6fs$ (B). Raw images are shown in ***a*** and ***d*** , and corresponding photoelectron energy spectra as a function of the emission angle are plotted in ***b*** and ***e*** respectively. ***c*** and ***f*** show angular distributions for selected photoelectron energy.

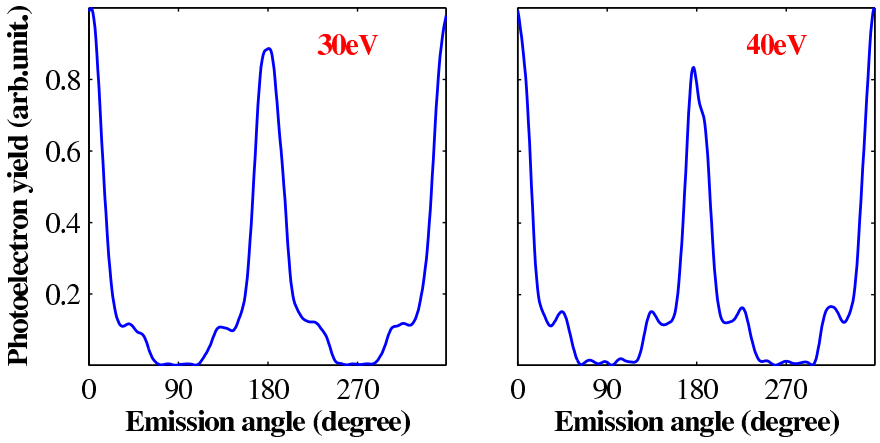

Figure 5.12: Angular distributions for selected photoelectron energies around $30eV$ and $40eV$ integrated over an energy bandwidth of $4eV$ from the results of Argon with $6fs$ pulses.

However, we do see weak contributions around 30^o in the results from Argon ionized with $6fs$ pulses at higher photoelectron energy. The angular distributions for a photoelectron energy around $30eV$ and $40eV$ integrated over an energy bandwidth of $4eV$ are shown in Figure 5.12. This figure clearly shows that electrons also appear around 30^o at higher energies in the plateau region. This again indicates that electrons appearing around 30^o are due to recollision. Furthermore, the independence of the 30^o feature to the pulse duration, laser intensity and atomic species all confirm that it is an intrinsic property of the ionization process.

5.5 Summary and future work

Asymmetry along the laser polarization in the electron emission in above-threshold ionization of rare gas atoms has been studied with a 2D velocity-map imaging photoelectron spectrometer. It can be used to measure the carrier-envelope phase. Because of the high collection efficiency, close to 100%, it may also allow a real-time single-shot measurement of the carrier-envelope phase.

We have observed interference structures in above-threshold ionization in Xenon, Argon and Krypton, which can be explained by interference between electron wavepackets which are created in successive half-cycles of the laser field. We have also observed electrons emitted around 60^o and 30^o with respect to the laser polarization, which has never been reported before. The former seems to

be part of the interference of electron wavepackets, while the latter is believed to be due to the recollision of electrons off their parent ionic core. Detailed physical explanations are needed. Theoretical work by solving the time-dependent Schrödinger equation and by using a strong-field approximation approach are ongoing [160]. A detailed study on the dependence of the photoelectron angular distributions on the carrier-envelope phase of the infrared laser pulses will possibly be able to tell us if the observed electrons at 30^o are indeed from a recollision process.

Part III

Attosecond laser pulses and their applications

Chapter 6

Generation and characterization of attosecond pulse trains

We report experiments on the characterization of a train of attosecond pulses, using mixed-color (XUV+IR) atomic two-photon ionization and detection of the resulting photoelectrons on a velocity-map imaging detector. We demonstrate that the relative phases of different XUV frequency components obtained by means of high harmonic generation are not only encoded in the dependence of the photoelectron yield on the XUV-IR time delay, but also in the angular distribution of the ejected photoelectrons, thus making the technique suitable for the detection of single attosecond pulses. We present measurements on the characterization of attosecond pulses resulting from harmonic generation in three different generation gasses, and conclude that the timing of the attosecond pulse with respect to the field oscillation of the driving laser critically depends on the target gas used to generate the harmonics.

6.1 Introduction

Important advances have been made in the experimental realization and detection of attosecond laser pulses formed through the generation of high-order harmonics (HHG) of femtosecond infrared (IR) laser pulses in noble gas atoms [91, 95, 89]. In that process attosecond time structures result from phase locking of a series of discrete plateau harmonics [95, 101, 97], or a sufficiently broad segment of the cutoff harmonics continuum [89].

Many problems still have to be solved before well characterized and controlled attosecond pulses can be used as a routine tool for time-resolved spectroscopy. When many-cycle IR pulses are used for the harmonic generation, the attosecond pulses appear in a pulse train. Although we will show results in the next chapter where a sequence of attosecond laser pulses is crucial for the success of the experiment, pulse trains are incompatible with many pump-probe experiments and the ultimate goal is to produce single attosecond pulses. Another problem is the characterization of the attosecond pulses. Full characterization can only be done through a non-linear process, since linear processes do not mix different frequency components and thus are insensitive to their relative phase. Knowledge of the latter is essential and (together with the easily measurable amplitudes) sufficient for determining a complete field reconstruction except for an overall phase.

6.2 Reconstruction of attosecond harmonic beating by interference of two-photon transitions

A method for Reconstruction of Attosecond harmonic Beating By Interference of Two-photon Transitions (RABBITT) has been proposed by Muller [94]. This approach is closely related to the theoretical work of Veniard *et al* [161]. An infrared field is introduced so that ionization with a harmonic photon can be accompanied by absorption as well as emission of different numbers of IR photons. In the electron spectrum, this results in the appearance of sidebands. At low IR intensity, where the problem can be treated in second-order perturbation theory, each atom can adsorb and emit one IR photon, resulting in only a pair of sidebands adjacent to the peak that results from ionization by a harmonic. These sidebands appear at energies corresponding to even multiples of the IR photon energy. Only two nearest harmonics H_q, H_{q+2} contribute to each sideband peak S_{q+1} by adsorbing or emitting an IR photon. The sideband signal contains a phase $\phi_q - \phi_{q+2} + 2\phi_{IR}$ due to the interference of these two paths. Retarding

the IR beam by a time τ with respect to the harmonic field sets $\phi_{IR} = \omega_{IR}\tau$. The sideband signal is then mapped as a function of τ. The integrated sideband signal is

$$S_{q+1} = A_f cos(\phi_q - \phi_{q+2} + 2\omega_{IR}\tau + \Delta\phi^f_{atomic}), \tag{6.1}$$

where A_f is the transition amplitude and $\Delta\phi^f_{atomic}$ is the intrinsic complex phase of the transition matrix elements, which is small and can be obtained from established theory with high precision. The phase difference $\phi_q - \phi_{q+2}$ can be determined by fitting experimentally recorded sideband signals. RABBITT has been successfully used in characterizing attosecond pulse trains [95, 99, 162, 97].

In previous experiments transitions involving harmonics and the fundamental IR laser were observed in a focused geometry using a time-of-flight electron spectrometer, where the photoelectron signal was integrated over all ejection angles. This method would run into trouble when characterizing single attosecond pulses or very short trains of such pulses, where photoelectrons produced by single- and two-color (XUV+IR) multi-photon ionization have overlapping energy distributions. Therefore it is essential to find alternative ways to distinguish single-photon and two-photon events. In this chapter, we demonstrate that the angular distribution of the photoelectrons can be used to this end.

6.3 Photoelectron angular distribution

The photoelectron angular distribution (PAD) results from a superposition of partial waves of electrons emitted from an atomic or molecular ion core. The electron wavefunction can be expressed as [163, 164]

$$\psi_f = \sum_{lm} c_{lm} e^{-i\delta_l} Y_{lm}(\theta, \phi), \tag{6.2}$$

where c_{lm} contains radial and angular information about the state from which the photoionization occurred and about the continuum, and δ_l is a phase shift acquired during the photoionization process. Y_{lm} are partial spherical harmonics labeled by l, the orbital angular momentum quantum number, and m, the laboratory frame projection quantum number. Here $\theta \in [0, \pi]$ is defined as the polar angle[1] starting from the Z axis, and $\phi \in [0, 2\pi)$ is the azimuthal angle[2] in the XY plane, starting from the X axis. See the Appendix for a detailed illustration of

[1]Note that, in mathematical literatures, the definition of polar and azimuthal angles are exchanged.

[2]This azimuthal angle should not be confused with the phase angle that we used in the RABBITT measurement.

the spherical coordinate system used. Then the measured photoelectron angular distribution is obtained by taking the square modulus of Equation 6.2:

$$\begin{aligned} I(\theta,\phi) \propto \psi_f \psi_f^* &= \sum_{lm}\sum_{l'm'} c_{lm} c_{l'm'}^* e^{-i(\delta_l - \delta_{l'})} Y_{lm}(\theta,\phi) Y_{l'm'}^*(\theta,\phi) \\ &= \sum_{LM} B_{LM} Y_{LM}(\theta,\phi), \end{aligned} \tag{6.3}$$

where $L \leq l + l'$ and $M = m + m'$. B_{LM} thus contains information about the scattering phase of each individual partial wave function and the interference between them.

For photo-ionization with a linearly polarized laser of an isotropic distribution of atoms or molecules, L must have even values because of the inversion symmetry of the system studied. In addition, a cylindrical symmetry exists around the laser polarization direction, which is chosen to be parallel to the Z axis in the coordinate system. In this case only $M = 0$ contributes to the angular distribution. Furthermore, if we take measurements in a plane where ϕ is constant, for example, $\phi = 0$, then the photoelectron angular distribution in the measurement plane reduces to

$$I(\theta) \propto \sum_{L=0}^{2K} B_{L0} Y_{L0}(\theta), \tag{6.4}$$

where K is the maximum number of photons involved during the ionization process.

Mathematically, the spherical harmonics are related to associated Legendre polynomials by

$$Y_{lm}(\theta,\phi) = \sqrt{\frac{2l+1}{4\pi}\frac{(l-m)!}{(l+m)!}} P_l^m(cos\theta) e^{im\phi}. \tag{6.5}$$

We can rewrite Equation 6.4, in terms of zero order Legendre polynomials, as

$$I(\theta) \propto \sum_{L=0}^{2K} B_{L0}^{'} P_L^0(cos\theta). \tag{6.6}$$

For a two-photon process, for example, the sideband signal in a RABBITT measurement involving one XUV photon and one IR photon, the photoelectron angular distribution can thus be expressed as

$$\begin{aligned} S_{q+1}(\theta) &\propto \alpha P_0(cos\theta) + \beta P_2(cos\theta) + \gamma P_4(cos\theta) \\ &= \alpha + \beta P_2(cos\theta) + \gamma P_4(cos\theta). \end{aligned} \tag{6.7}$$

Here, α describes the angle-integrated total photoelectron intensity since the integration of higher order terms in the right side of Equation 6.7 is zero.

6.4 Experimental setup

Measurements of the α parameter in Equation 6.7 as a function of the time delay between the harmonic beam and the IR beam can be used to determine the phase relationship between two adjacent odd harmonics, and form the basis of the RABBITT method. This analysis was first performed by Paul *et al* [95] to reconstruct attosecond laser pulses trains from high order harmonic generation. Our experiment demonstrates that a similar analysis can also be performed on the basis of parameters β and γ by measuring the angular distribution of sideband photoelectron signals in a RABBITT measurement, replacing the traditional magnetic-bottle time-of-flight tube with a velocity-map imaging spectrometer.

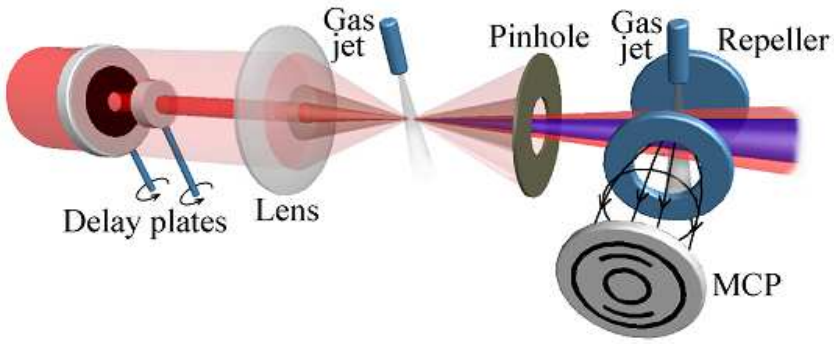

Figure 6.1: Experimental setup. See text for detailed description.

A 3D illustration of the experimental setup is shown in Figure 6.1. The output from a $50Hz$ Ti:Sapphire femtosecond laser system, delivering near-Fourier-transform limited $70fs, 10mJ$ laser pulses around $800nm$, is split into an annular outer beam (adjustable up to a diameter $D_{out} = 20mm$) and an inner beamlet ($D_{inner} = 3mm$), which are delayed with respect to each other by passing through two pieces of computer-controlled glass cut from the same antireflection-coated plate. An $f = 2m$ lens focuses the co-propagating IR beams into a rare gas jet, where the annular beam generates harmonics. A masking plate with a $D_{mask} = 0.5mm$ pinhole blocks the annular part of the IR beam $20cm$ behind the focus, and transmits the inner IR beam and the harmonics into a spectrometer chamber. There the lasers cross an atomic beam and the resulting photoelectrons are detected using velocity imaging, which projects the electrons with the aid of electrostatic fields onto a position-sensitive channel-plate detector. The

3D velocity distribution is recovered from the measured projection by applying an iterative procedure [135]. Our experiment uses an in-line geometry, where the XUV and IR beams are not refocused, thus creating optimally 'clean conditions' for the determination of the relative phases of the high-order harmonics.

Argon was used as an ionization target, because of the availability of calculated matrix elements for its mixed-color two-photon ionization [165]. The favorable cross sections for XUV single-photon ionization of Ar facilitate the detection of high-order harmonics. The ionization potential of Ar ($\sim 10\hbar\omega_{IR}$) limits the lowest detectable harmonics order 11. The highest detected order, 21, is limited by the present geometry of the spectrometer.

6.5 Results and discussion

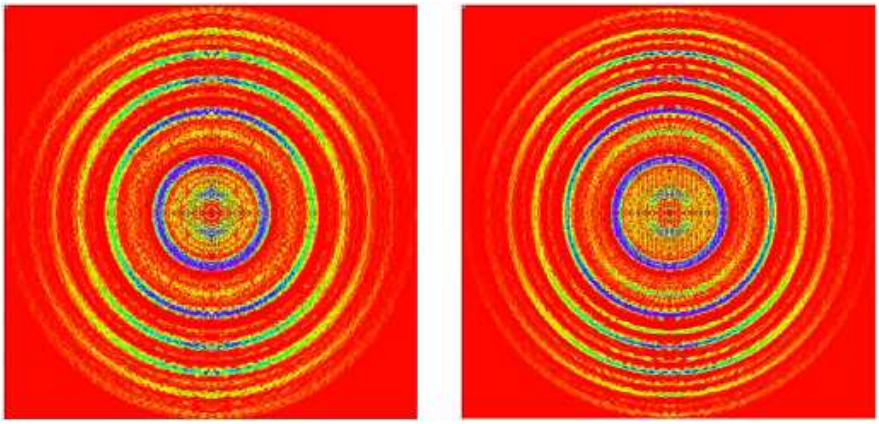

Figure 6.2: 2D Slice through the 3D velocity distribution measured for mixed-color two-photon (XUV+IR) ionization of Argon, where the XUV light is obtained through high harmonic generation in Argon. The 3D velocity distribution contains a series of prominent rings resulting from ionization by one XUV photon ($11th - 21st$ harmonic) and weaker sidebands at intermediate energies where two mixed-color ionization processes involving the adjacent harmonics interfere. In the image on the left, the interference is destructive for most sidebands, whereas in the image on the right it is constructive.

Typical angle-resolved photoelectron images obtained with harmonics generated in an Argon gas jet are presented in Figure 6.2, where 2D slices are shown through the 3D velocity distributions obtained. Prominent rings result from single-photon ionization by the $11th$ to $21st$ harmonic. In the right panel, one

can discern sidebands between consecutive rings. The signal associated with these sidebands disappears when the dressing field is blocked.

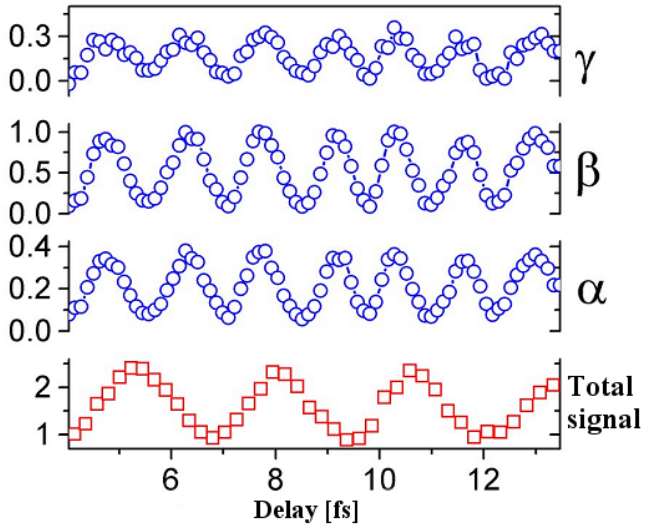

Figure 6.3: Extracted oscillations associated with parameters α, β and γ as defined in Equation 6.7 for sideband S_{16} that contains interfering contributions from ionization by the $15th$ and $17th$ harmonics, as a function of the time delay between the XUV pulse and the IR dressing beam. Both parameter α, describing the intensity of the sideband, and parameters β and γ, describing the angular distribution of the ejected photoelectrons in the sideband, oscillate as a function of the delay with half the IR period, and allow the extraction of a phase that contains information about the phase shift between the $15th$ and $17th$ harmonics. The total signal oscillates with the full IR period.

Figure 6.3 shows α, β and γ for sideband S_{16} arising from interference between different ionization channels involving the $15th$ and the $17th$ harmonics, together with a curve representing the total photoelectron signal (the sum of all harmonics and sidebands).

The total signal oscillates with a frequency that corresponds to the IR field period of $\sim 2.7fs$, since the total laser intensity at the harmonic generation point is slightly affected by the weak dressing beam passing through it. This results in oscillations in the total XUV-yield as the phase of the dressing IR is scanned, that can be fit to a functional form $cos(\omega_{IR}\tau)$. The total signal thus allows *in situ* calibration of the delay τ which (for small rotation angle of the glass plates) is a quadratic function of this angle.

In the sideband signals, characteristic oscillations occur in the α parameter at twice the frequency of the oscillations in the total photoelectron yield, since the

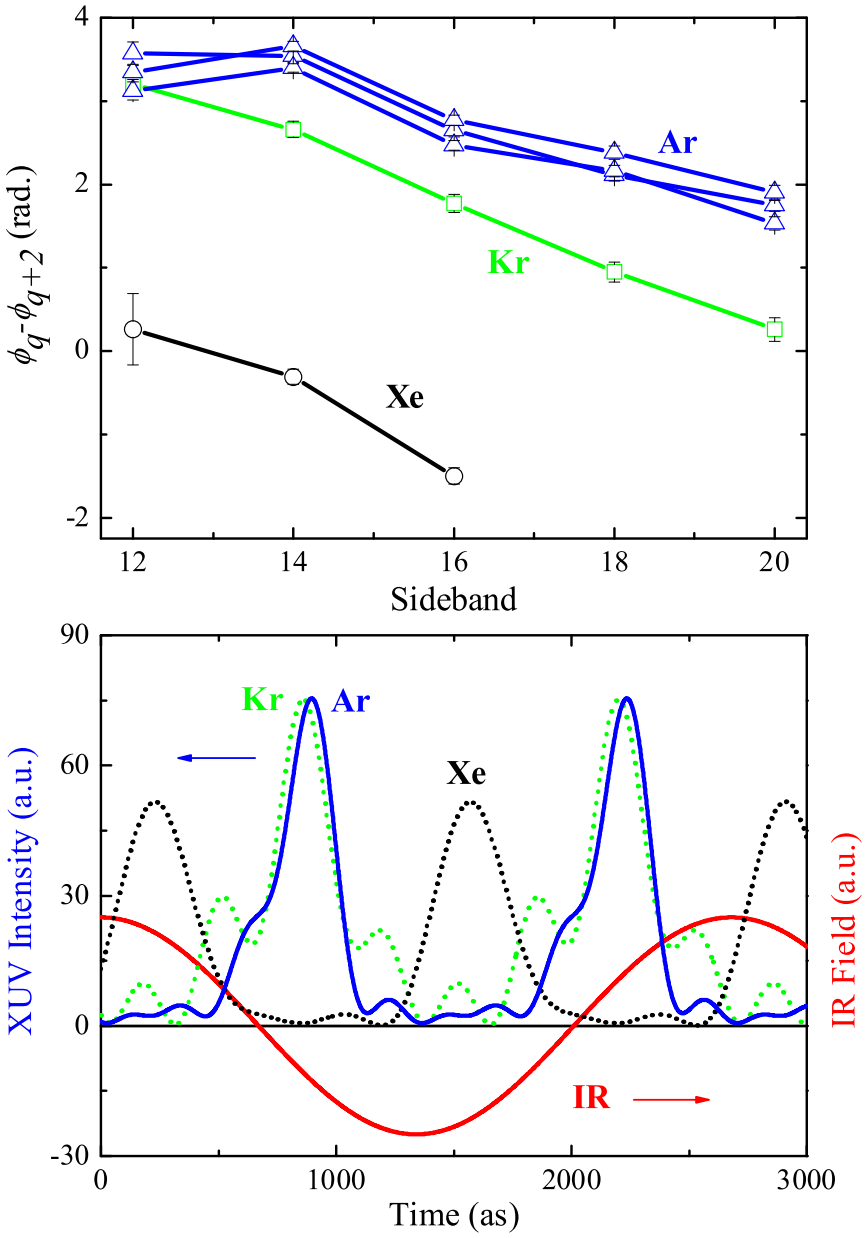

Figure 6.4: Top: Extracted phase differences $\phi_q - \phi_{q+2}$ between adjacent harmonics for three experiments performed using Argon as harmonic generation gas(open triangles), and using Krypton (open squares) and Xenon (open circles) as harmonic generation gases. The three Argon data sets were taken on different days under conditions as similar as we could make them. Bottom: XUV temporal shape for Argon, Krypton, and Xenon as harmonic generation gases, on the basis of the harmonic phase differences shown in the top plot. The harmonic amplitudes needed for the reconstruction were obtained from photoelectron spectra recorded in the absence of the IR dressing beam.

interference involves one channel where an IR photon is emitted and one where an IR photon is absorbed. Even deeper oscillations can be clearly distinguished in the parameters β and γ. Fitting these curves to a cosine function, as a function of the pre-determined delay τ, gives us the possibility to extract from our experimental data the three phases ϕ_α, ϕ_β and ϕ_γ. The fact that the modulation depths and phases of parameters α, β and γ are not equal points out that there exists a qualitative modulation of the shape of the angular distributions, rather than merely an overall change of the signal strength.

According to the theoretical treatment of the mixed-color two-photon ionization, the relative phase of the harmonics can be obtained from ϕ_α by subtracting a small phase correction $\Delta\phi^f_{atomic}|_\alpha$ contributed by the atomic response [95, 165]. $\Delta\phi^f_{atomic}|_\alpha$ is about $0.1 \sim 0.2rad$, depending on the sideband order and quantum paths involved.

Phase differences of neighbouring harmonics $\phi_q - \phi_{q+2}$ for a series of experiments using Argon, Krypton and Xenon as harmonic generation gas are shown in the top panel of Figure 6.4. Combining these phase measurements with a measurement of the relative amplitudes of the harmonics determined from the photoelectron spectra, a reconstruction of the XUV temporal shape becomes possible. As shown in the bottom panel of Figure 6.4, the reconstructed XUV-burst can be as short as $\sim 250 \pm 30$ $attosecond(FWHM)$ for harmonic orders 11 through 21 when argon is used for high-harmonic generation.

The reconstruction of the XUV temporal shape also yields a determination of the timing of the XUV bursts with respect to the field oscillations of the femtosecond IR laser. According to the description of high-harmonic generation in terms of the three-step recollision model, the time corresponding to the maximum kinetic energy of the ionized electrons upon recolliding with their parent ions occurs at a delay of about 70% of the IR period (T_{IR}) with respect to the field maximum of the IR field [21]. Taking into account the Gouy phase shift accumulated by the XUV and IR dressing beams between the high-harmonic generation point and the spectrometer [96], we obtain a pulse timing of $(0.83 \pm 0.05) \times T_{IR}$ for Argon and Krypton and $(0.59 \pm 0.07) \times T_{IR}$ for Xenon, see Figure 6.4. This striking difference between Argon and Krypton versus Xenon is most likely due to the fact that in the former case the high-harmonic generation takes place in the tunneling regime, whereas in the latter it takes place in the multiphoton ionization regime. In the latter case, resonant effects can strongly affect recollision times [37]. The observed differences between Argon, Krypton, and Xenon underscore the remarkable robustness of the results that have been obtained for these three gases over the course of extensive experiments, where variations in the laser intensity, beam focusing conditions, and harmonic gas densities might have led

to variations in the phases determined [166]. It seems that optimization of the harmonic yield and quality of the 2D photoelectron images has ensured that on a day-to-day basis the experiment was performed under rather similar conditions. (See the argon results in Figures 6.4 and 6.5.)

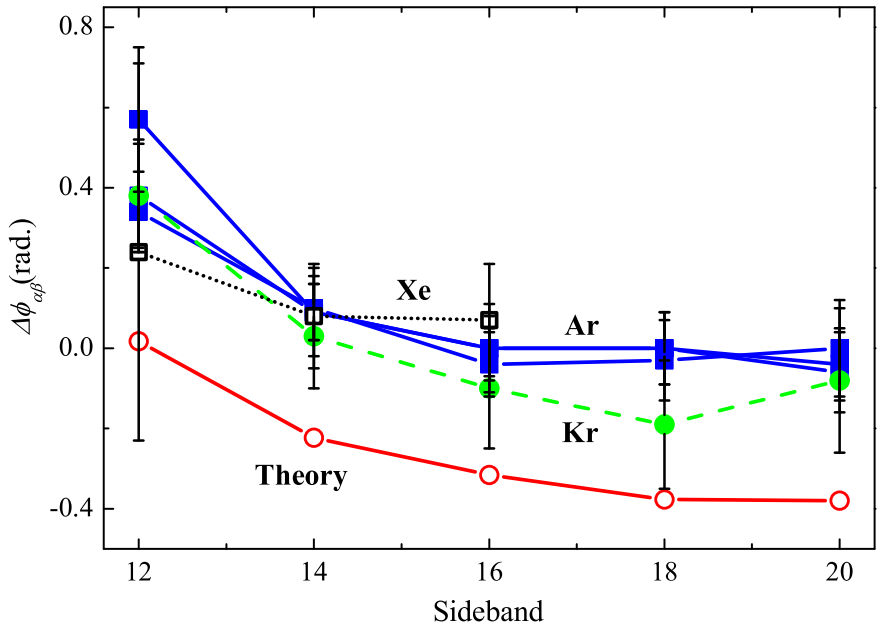

Figure 6.5: Difference between the extracted phases $\Delta\phi_{\alpha\beta} = \phi_\alpha - \phi_\beta$ for three experiments using Argon (solid squares), Krypton (solid circles), and Xenon (open squares) as harmonic generation gas, along with a theoretical prediction based on the mixed-color two-photon ionization model (open circles). Since the phase difference depends only weakly on the harmonic amplitudes and is independent of the harmonic phases, the experimental results lie on top of each other, and agree reasonably well with the theoretical prediction.

The phase corrections $\Delta\phi^f_{atomic}|_\beta$ and $\Delta\phi^f_{atomic}|_\gamma$ depend only weakly on the harmonic amplitudes, and thus are practically independent of the generation process. As such, they provide a good check on the various atomic phases obtained by theoretical modeling of the ionization process. Results obtained for $\Delta\phi_{\alpha\beta} = \phi_\alpha - \phi_\beta$ are presented in Figure 6.5. Within the accuracy of the measurements, all experimental curves coincide. The theoretical curve [165] reproduces the trend in the experimental data quite well, albeit with a slight offset. The theoretical results for $\Delta\phi_{\alpha\beta}$ and $\Delta\phi_{\alpha\gamma}$ remain almost constant when the ratio of the amplitudes of neighboring harmonics is changed in the range between 0.5 and 2. Thus, the reconstruction of the XUV pulse shape can be performed both on the basis of sideband intensities and on the basis of the angular distribution

measurements.

More importantly, phase ϕ_γ associated with the αP_4 term in Equation 6.7 only appears in the two-photon sideband signals, not in the photoelectron signals arising from one-photon ionization by harmonics. Therefore, the phase dependence of the angular distribution might be useful for characterization of attosecond pulses under conditions where the harmonic spectrum is so broad (due to the short pulse duration) that one- and two-photon signals overlap in energy and can no longer be distinguished in a measurement where the photoelectron kinetic energy spectrum is obtained with a traditional magnetic-bottle time-of-flight tube.

6.6 Conclusion

We have demonstrated that angle-resolved photoelectron spectroscopy in mixed-color (XUV+IR) two-photon ionization can be used to determine the relative phases of a comb of harmonics and to reconstruct the temporal shape of the XUV pulse. Harmonic generation in Argon, Krypton and Xenon has been characterized with this technique. A striking dependence of the timing of the attosecond XUV bursts on the harmonic generation gas was observed. XUV bursts appear earlier in Xenon than in Argon and Krypton, which is attributed to the fact that high harmonic generation in Xenon occurs in the multi-photon ionization regime, while it occurs in the tunneling ionization regime in Argon and Krypton. XUV bursts with pulse durations as short as $250as$ are obtained from the harmonic generation in Argon. Since the angular measurements allow a separation of the photoelectron signals into one- and two-photon contributions, it should be possible to extend this technique to the characterization of isolated attosecond pulses.

Chapter 7

Attosecond electron wavepacket interferometry

In this chapter we describe an attosecond electron wavepacket interferometric experiment, where Argon atoms are ionized by a sequence of attosecond XUV pulses in the presence of an infrared laser field that induces a momentum shear between consecutive electron wavepacket replicas. Through the momentum shear, electron wavepackets with different initial momenta are made to overlap and the resulting interferogram contains information on the variation of the phase of the electron wavefunction in momentum space, and consequently on that of the ground-state wave function. Its applicability to reveal fundamental process of single photon ionization will also be discussed. This technique opens a new avenue toward the complete determination of excited and ground-state electronic wave functions of complex, chemically relevant molecules.

7.1 Introduction

To describe the interaction of matter with the external world, quantum mechanics uses complex quantities, such as wave functions and transition matrix elements, defined by an amplitude and a phase. Measurements generally focus on the determination of probability distributions and cross-sections which are related to the square modulus of the above quantities and hence only reveal amplitude information. To access phase information, interferometric methods are required, analogous to the situation encountered in optics, where interferometry is applied to determine the phase variations in time and space of electromagnetic waves.

There are two types of implementation of interferometry in optics, from which phase information can be obtained. In the first implementation, a light field $E(x)$ is split into two replicas. Each replica travels a different path. The two replicas interfere when they are recombined, and from the interference pattern

$$|E(x) + E(x)e^{i\Delta\Phi(x)}|^2 \propto 1 + cos\Delta\Phi(x). \tag{7.1}$$

the difference in the accumulated phase, $\Phi(\Delta x)$, in the two paths can be extracted. The interference pattern in this case does not depend on the phase of the initial field, but on the optical path difference. This technique can therefore be used, for example, to measure refractive indices.

In the second implementation, the field itself can be characterized if a *shear* Δx is introduced into one of the replicas. If $|E(x)| \approx |E(x + \Delta x)|$ in the region of overlap, we have

$$|E(x) + E(x + \Delta x)|^2 \propto 1 + cos[\phi(x) - \phi(x + \Delta x)]. \tag{7.2}$$

where $\phi(x)$ is the phaser of $E(x)$. In this case, information about the optical field itself and especially on the variation of the phase $\phi(x)$, can be retrieved. This technique has been applied extensively in optics for the measurement of wavefront distortions (where a spatial shear is induced) [167] and the determination of the spectral phase of ultrashort optical pulses (where a spectral shear is induced) [126]. A variant in momentum space, called momentum-shearing interferometry has been proposed in atom optics [106].

Our interferometric scheme closely resembles the above discussed traditional implementation of interferometry in optics. In our experiment, we observe interferences in momentum space between continuum electron wavepackets that are prepared through ionizing Argon atoms by a train of attosecond laser pulses in the presence of an infrared laser field. This gives us the possibility to retrieve the phase information of the electron wave function, and to investigate the electron dynamics during the process of atomic photoionization.

7.2 Principle of wavepacket interferometry

Attosecond pulses created through high-order harmonic generation by focusing a driving infrared laser field onto rare gases are generally separated by half of the infrared laser period. Consecutive electron wavepackets created by a train of attosecond pulses will interfere where their momentum distributions overlap. The principle of a wavepacket interferometry will be illustrated in this subsection for the case of Helium. The calculations that will be presented in this section were done by J. Mauritsson and K. Schafer from the Department of Physics at Louisianan State University, USA.

The photoelectron momentum distribution $|\Psi(\mathbf{p})|^2$ obtained when a Helium atom is ionized by a single attosecond pulse is shown in Figure 7.1(a). It is a ring-shaped distribution peaked along the laser polarization axis, which is defined as p_y axis in this study.

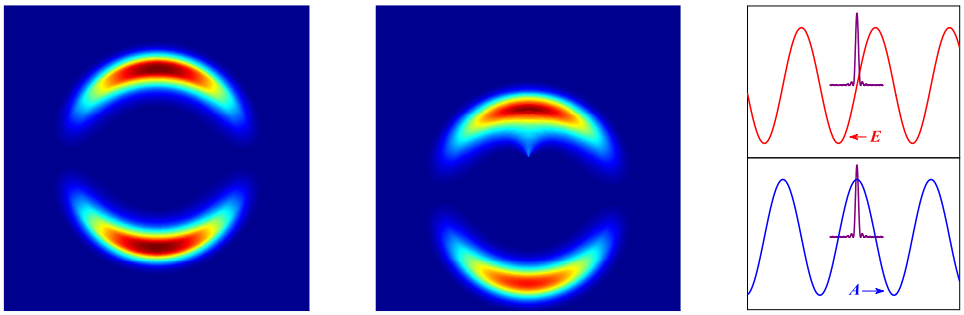

(a) (b) (c)

Figure 7.1: Calculations performed by solving the time-dependent Schrödinger equation in Helium within the single active electron approximation. Helium atoms are ionized by a single $180as$ pulse with central energy around $46eV$ and a bandwidth of $11eV$. (a) shows the momentum distribution of electrons ionized by the attosecond pulse in the absence of the infrared laser field. (b) shows a shifted distribution when the ionization occurs in the presence of an infrared laser field that is linearly polarized along the y axis ($I_{IR} = 3 \times 10^{13} W/cm^2$). Here the attosecond pulse coincides with the maximum of the vector potential $\mathbf{A}$. The momentum shift is equal to $-e\mathbf{A}$. See texts for detailed explanation. (c) shows the infrared laser field $\mathbf{E}$, the vector potential $\mathbf{A}$ and the single attosecond pulse.

When an infrared laser field is present at the time of creation of the electron wavepackets, the momentum distribution is shifted by the amount of momentum transferred from the field to the electron wavepackets, as shown in Figure 7.1(b).

This momentum transfer is maximum when the electric field of the infrared laser crosses zero, and zero when the field is at a maximum or a minimum. This agrees with previous results using attosecond pulse trains[168] or single attosecond pulses [88]. This effect, which strongly depends on the initial timing, has previously been used in attosecond metrology to determine the characteristics of single attosecond pulses [89] as well as of the infrared laser field [109].

A train of attosecond XUV pulses can be described as a sum of odd harmonics which we assume for simplicity to have an equal amplitude

$$\mathbf{E}_{XUV}(t) \propto \sum_q e^{iq\omega t}. \tag{7.3}$$

The transition amplitude from the ground state to a final state with momentum $\mathbf{p}$ is given by:

$$a_{\mathbf{p}}(\tau) \propto \int_{-\infty}^{+\infty} \mathbf{E}_{XUV}(t) \cdot d[\mathbf{p} + e\mathbf{A}(t,\tau)] e^{-iS(t,\tau)/\hbar} dt. \tag{7.4}$$

where $\mathbf{A}(t,\tau) = \mathbf{A}_0 sin[\omega(t+\tau)]$ is the vector potential of the infrared laser field $E_L = E_0 cos[\omega(t+\tau)]$, delayed by τ relative to the attosecond XUV pulse and $S(t,\tau)$ is the quasi-classical action describing the motion of an electron ionized at time t in the infrared laser field. The attosecond XUV field and the infrared laser field are both chosen to be polarized along the Y-axis. The one-photon dipole-matrix-element, $\mathbf{d}(\mathbf{p})$, in the direction of the XUV field is generally written as $d_y(\mathbf{p}) = \mid d_y(\mathbf{p}) \mid e^{i\phi(\mathbf{p})}$. Assuming that attosecond XUV pulses are only nonzero at time $t = k\pi/\omega$, the time integration in equation 7.4 can be replaced by a discrete sum over the number of attosecond pulses, labelled by an integer $\mathbf{K}$.

$$\begin{aligned} a_{\mathbf{p}}(\tau) &\propto \int_{-\infty}^{+\infty} \sum_q e^{iq\omega t} d[\mathbf{p} + e\mathbf{A}(t,\tau)] e^{-iS(t,\tau)/\hbar} dt \\ &\simeq \sum_k e^{iqk\pi} d_y[\mathbf{p} + e\mathbf{A}(\frac{k\pi}{\omega},\tau)] e^{-iS(\frac{k\pi}{\omega},\tau)/\hbar} dt. \end{aligned} \tag{7.5}$$

In what follows we consider a special case, for reasons of simplicity, where only two consecutive electron wavepackets are present in the interference. The underlying physics is the same for the interference of a train of attosecond electron wavepackets.

There are three phase factors which lead to the wavepacket interference. First, a π phase shift between consecutive attosecond pulses, which comes from the first term in the integrand in equation 7.5. Second, a dipole phase difference $\Delta\phi_{\mathbf{p}}$ due to the momentum shear of the attosecond electron wavepacket, which comes from the second term in the integrand in equation 7.5. This phase difference can be

described as

$$\Delta\phi_{\mathbf{p}} = \phi[\mathbf{p} + e\mathbf{A}(\frac{k\pi}{\omega}, \tau)] - \phi[\mathbf{p} - e\mathbf{A}(\frac{k\pi}{\omega}, \tau)]. \tag{7.6}$$

Third, a phase difference $\Delta\phi_S$ that the electron wavepacket accumulates in the strong infrared laser field through quasi-classical action, which comes from the third term in the integration equation 7.5. The quasi-classical action S which describes the motion of the ionized electron in a strong infrared laser field can be written as

$$S(t, \tau) = \int_t^{+\infty} \frac{(\mathbf{p} + e\mathbf{A_0} sin[\omega(t+\tau)])^2}{2m} dt + I_p t. \tag{7.7}$$

The phase difference is then

$$\begin{aligned}
\Delta\phi_S &= \frac{1}{\hbar}\{\int_{\frac{(k+1)\pi}{\omega}}^{+\infty} \frac{(\mathbf{p} + e\mathbf{A_0} sin[\omega(t+\tau)])^2}{2m} dt + I_p \frac{(k+1)\pi}{\omega}\} \\
&\quad -\frac{1}{\hbar}\{\int_{\frac{k\pi}{\omega}}^{+\infty} \frac{(\mathbf{p} + e\mathbf{A_0} sin[\omega(t+\tau)])^2}{2m} dt + I_p \frac{k\pi}{\omega}\} \\
&= I_p \frac{\pi}{\hbar\omega} + \frac{1}{\hbar}\int_{\frac{k\pi}{\omega}}^{\frac{(k+1)\pi}{\omega}} \frac{(\mathbf{p} + e\mathbf{A_0} sin[\omega(t+\tau)])^2}{2m} dt \\
&= I_p \frac{\pi}{\hbar\omega} + \frac{\mathbf{p}^2}{2m}\frac{\pi}{\hbar\omega} + \frac{e^2 A_0^2}{4m}\frac{\pi}{\hbar\omega} + (-1)^k \frac{2eA_0 \mathbf{p} cos\theta}{m\hbar\omega} cos(\omega\tau) \\
&= W\frac{\pi}{\hbar\omega} \pm \frac{2eA_0 \mathbf{p}_y}{m\hbar\omega} cos(\omega\tau).\ (\mathbf{p_z} = 0).
\end{aligned} \tag{7.8}$$

where $W = I_p + U_p + (\mathbf{p_x^2} + \mathbf{p_y^2})/2m$, I_p is the ionization potential, $U_p = e^2 A_0^2/4m$ the ponderomotive energy and θ the angle between the laser polarization axis and the final momentum of the electron. The total phase difference is then

$$\Delta\phi = \Delta\phi_S + \Delta\phi_{\mathbf{p}} + \pi. \tag{7.9}$$

When attosecond XUV pulses coincide with the maxima/minima of the infrared laser field, i.e. $cos\omega\tau = \pm 1$, the vector potential is zero as shown in Figure 7.2(a). The momentum transfer from the laser field to the electron wavepackets is zero, thus the dipole phase difference $\Delta\phi_{\mathbf{p}}$ then becomes zero. Only the accumulated phases due to the different amount of time the electron wavepackets spend in the continuum contribute to $\Delta\phi$, and it simplifies to

$$\Delta\phi = W\frac{\pi}{\hbar\omega} \pm \frac{2eA_0 \mathbf{p}_y}{m\hbar\omega} + \pi. \tag{7.10}$$

The interference pattern consists of circles, centered at $(p_x = 0, p_y = \pm 2eA_0/\pi)$, see Figure 7.2(b). The $\pm$ sign depends on the sign of the vector potential at

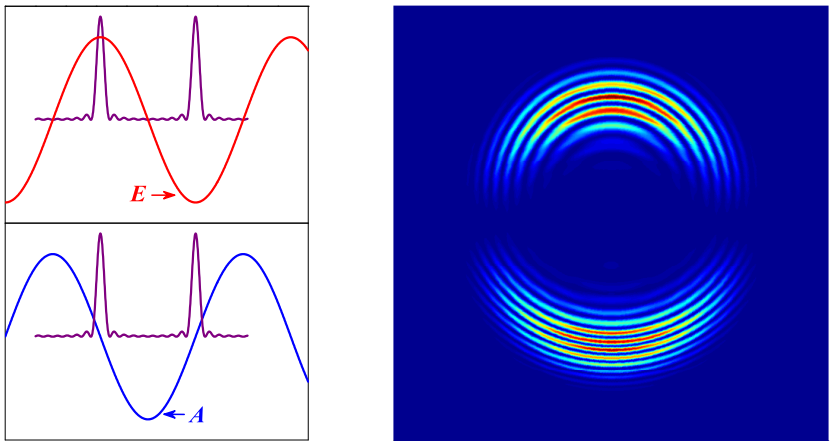

(a) (b)

Figure 7.2: Calculations performed by solving the time-dependent Schrödinger equation in Helium within the single active electron approximation. Helium atoms are ionized by a sequence of two attosecond pulses separated by half the infrared laser period, as shown in (a). The ionization occurs at a zero crossing of the vector potential **A**. The interference shown in (b) is due to the accumulated phase difference between the two electron wavepackets. See texts for detailed explanation.

which the two consecutive electron wavepackets are created. The positions of the maxima are determined by the condition:

$$\frac{\mathbf{p_x^2} + \mathbf{p_y^2}}{2m} \pm \frac{2eA_0\mathbf{p_y}}{m\pi} = (2n+1)\hbar\omega - I_p - U_p, \tag{7.11}$$

where n is a positive integer. This interference pattern can be used to determine the intensity of the infrared laser field, however no information about the initial phase of the electron wavepacket can be deduced.

When attosecond XUV pulses coincide with the zero crossings of the infrared laser field, i.e. $cos\omega\tau = 0$, the vector potential is maximum or minimum as shown in Figure 7.3(a). The momentum transfer from the infrared laser field is maximal and opposite in direction for consecutive wavepackets. The phase difference accumulated due to the interaction with the field between the two ionization events adds up to zero in this case. The phase difference now becomes

$$\Delta\phi = W\frac{\pi}{\hbar\omega} + \phi[\mathbf{p} + e\mathbf{A}(\frac{k\pi}{\omega}, \tau)] - \phi[\mathbf{p} - e\mathbf{A}(\frac{k\pi}{\omega}, \tau)] + \pi. \tag{7.12}$$

The position of the maxima of the interference pattern is determined by

$$\frac{\mathbf{p_x^2} + \mathbf{p_y^2}}{2m} \pm [\phi(\mathbf{p} + e\mathbf{A}) - \phi(\mathbf{p} - e\mathbf{A}]\frac{\hbar\omega}{\pi} = (2n+1)\hbar\omega - I_p - U_p. \tag{7.13}$$

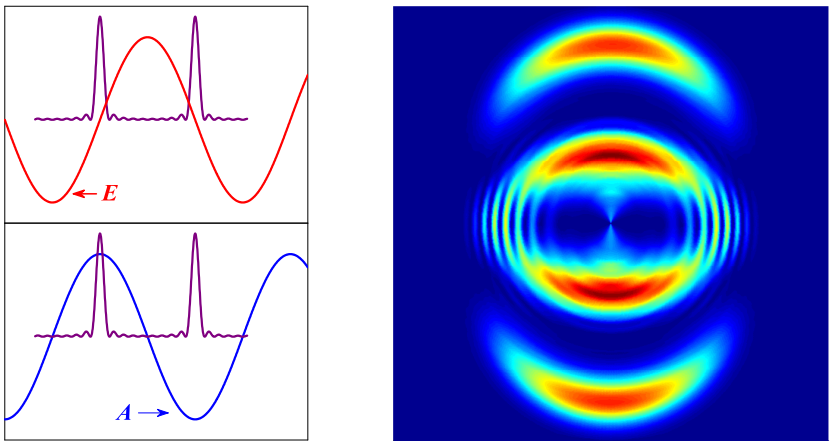

(a) (b)

Figure 7.3: Calculations performed by solving the time-dependent Schrödinger equation in Helium within the single active electron approximation. Helium atoms are ionized by a sequence of two attosecond pulses separated by half the infrared laser period, as shown in (a). The ionization occurs at a maximum/minimum of the vector potential **A**. The interference shown in (b) is due to a momentum shear between the two electron wavepackets. The interference occurs around 90^o with respect to the laser polarization, where the electron wavepackets overlap in momentum space. See the text for a detailed explanation.

It contains information on the relative phase $\phi(\mathbf{p})$ of the electron wavepacket at two different positions in momentum space.

7.3 Experiment and comparison to calculations

This experiment was performed in the Department of Physics at Lund Institute of Technology in Sweden. In our experimental implementation, see Figure 7.4, attosecond pulse trains were created through high-order harmonic generation by focusing $35fs$, $1.6mJ$ infrared laser pulses into a $3mm$ long Argon gas cell at $30mbar$ pressure. A $200nm$ thick Aluminium filter allowed us to eliminate the strong fundamental infrared field, to spectrally filter the low order harmonics, and to partially compensate for the positive intrinsic chirp of the attosecond pulses. Further filtering was achieved with a $1.5mm$ aperture in a convex spherical mirror. A train of attosecond pulses centered around $30eV$ were obtained.

The dressing infrared beam, a fraction of the driving laser beam which was

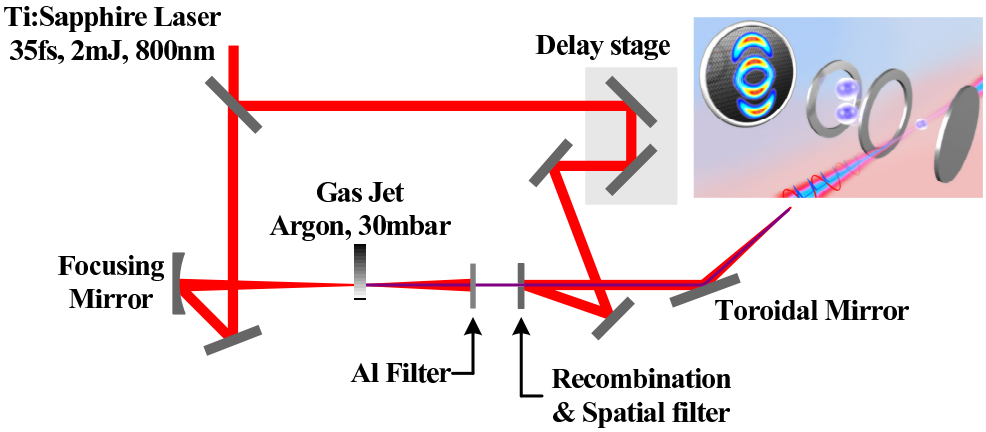

Figure 7.4: Experimental scheme. High-order harmonics are generated by focusing a strong infrared laser beam into an Argon gas jet. A train of attosecond pulses is formed by selecting a set of plateau harmonics with an Aluminium filter, which also blocks the strong infrared beam that came out together with the harmonics. Inset in the upper-right corner shows a schematic picture of the velocity-map imaging photoelectron spectrometer. See texts for detailed description.

used to generate the attosecond XUV pulses, was finely delayed relative to the attosecond XUV pulses with a piezo-electric actuated translation stage. The dressing beam was recombined with the XUV beam after reflection on a spherical convex mirror.

Both the XUV beam and the dressing beam were then focused by a toroidal platinum mirror into the active region of a velocity-map imaging spectrometer. Electron wavepackets with an individual duration of $200as$, a central kinetic energy of $11eV$ and a bandwidth of $11eV$ were created by ionizing Argon atoms with the attosecond pulse train. The polarization of the infrared and XUV fields were parallel, and perpendicular to the detection axis of the velocity-map imaging spectrometer.

Electrons created in the interaction region were accelerated in a DC field and projected onto the detector assembly consisting of dual micro-channel plates and a phosphor screen, from which a 2D image wass recorded. An iterative inversion algorithm [135] was used to reconstruct the electron distribution in 3D space from the recorded 2D image.

The main experimental observations are presented in Figure 7.5. 2D slices through the full 3D momentum distributions are presented for five delays between the XUV pulses and the infrared laser field, with a time step corresponding to

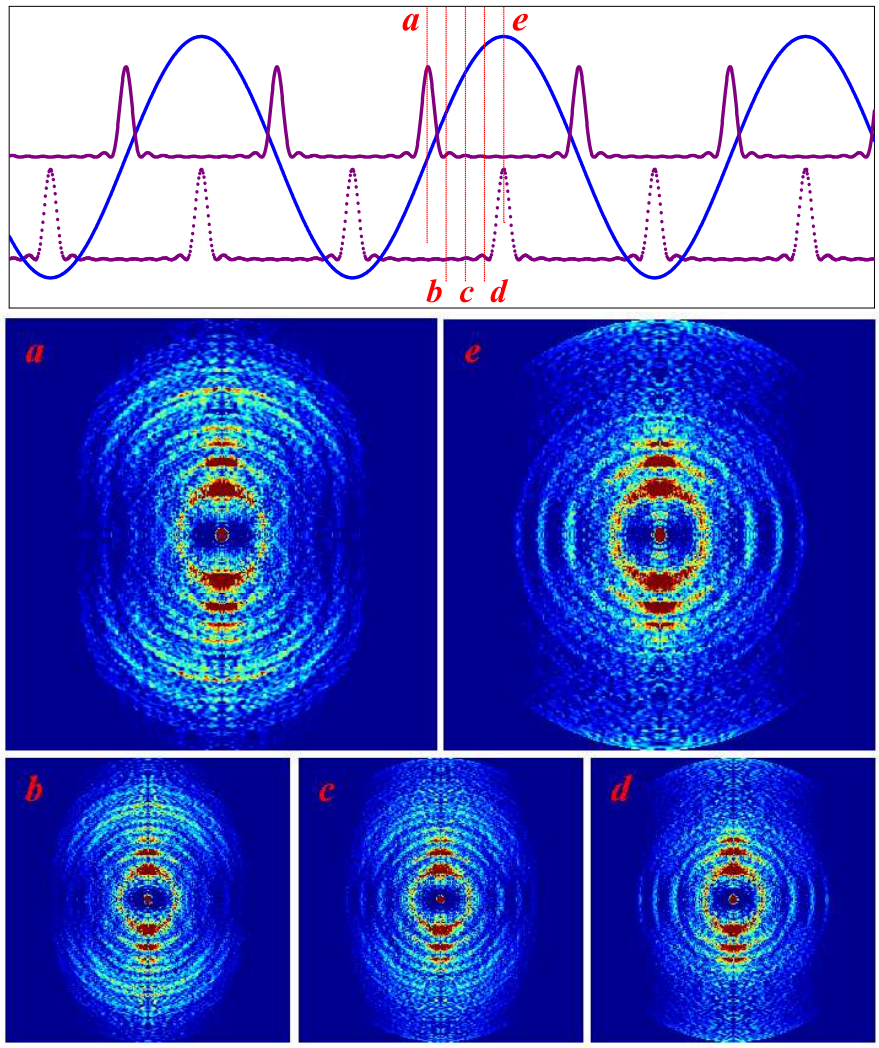

Figure 7.5: Vector potential of the infrared laser field and attosecond pulse trains are shown in the upper panel. Dotted curve shows a train of attosecond pulses that are delayed, with respect to the solid curve, by quarter of the infrared laser period $T_L/4$. 2D slice through the full 3D momentum distributions at five different delays, indicated by ***a*** to ***e***, are shown in the lower panel.

one sixteenth of the infrared laser period T_L ($T_L/16$). Compared to the calculations discussed above, an additional interference structure is observed. This interference pattern consists of circles centered at the origin, and results from the repetitive nature of the interference experiment over the length of the attosecond pulse train. These interference effects are very similar to those leading to electron peaks separated by $\hbar\omega$ in above-threshold ionization and express energy conservation

We now concentrate on the two extreme cases shown in Figure 7.5 ***a*** and ***e***, which correspond to two situations where electron wavepackets are created at a zero crossing and a maximum/minimum of the vector potential **A** of the infrared laser field.

We first discuss the situation where the attosecond pulse train coincides with a zero crossing of the vector potential. The interference structures correspond to this situation are shown in Figure 7.5 ***a***. This results should be compared with Figure 7.2, where a pair of attosecond XUV pulses coincide with the maxima and minima of the infrared laser field and the vector potential is zero. Complicated interferometric ring structures with broken lines are due to the fact that a train of attosecond pulse are used in the experiment, instead of a pair of attosecond pulses as we discussed in section 7.2.

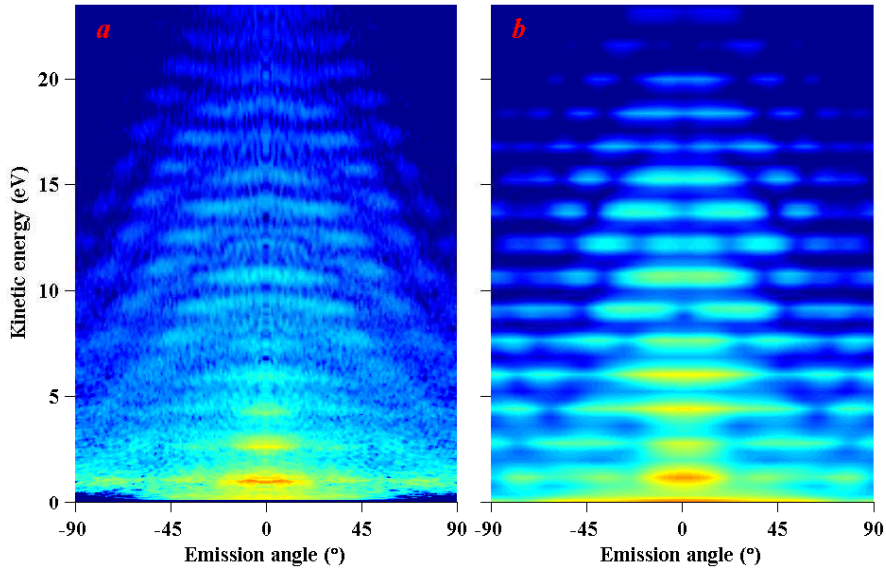

Figure 7.6: Contour plots of the momentum distribution of emitted electrons as a function of their kinetic energy and their emission angles, when the attosecond pulses coincide with the zeros of the vector potential of the infrared laser field. Experimental results are shown in ***a***, calculations for Argon by numerically integrating the time-dependent Schrödinger equation are shown in ***b***.

In order to understand in more details the interference effects, the momentum distributions were calculated by solving numerically the time dependent schrödinger equation in three dimensions for Argon within the single-active electron approximation. Shown in Figure 7.6 are contour plots of the momentum distributions of the electrons as a function of the kinetic energy and the emis-

sion angle $tg^{-1}(p_x/p_y)$ for both experiments and calculations. The experimental results of Figure 7.6 ***a*** compare very well with the theoretical calculations of Figure 7.6 ***b***. Energy conservation leads to horizontal fringes while the interference of consecutive electron wavepackets can be observed as ridge-like structures falling away on either side of the $\Theta = 0$ axis, allowing us to determine the intensity of the infrared laser field.

This interference should be compared to the interference structures that have been discussed in Chapter 5, see Figure 5.6 in Chapter 5. In that experiment an interference occurs between electron wavepackets that are mainly created through tunneling when the intense infrared laser field reaches a maximum or minimum, namely directly by infrared laser field itself. Electrons created by this manner have almost zero initial kinetic energy and they may be driven back and recollide with their parent ionic cores. While in current experiment, electrons normally have initial kinetic energy from a few to tens of eV due to the short wavelengths of the XUV laser pulses. These electrons will leave the parent ions after oscillatory motion in the infrared laser field, thus no recollisions are involved.

Next, we discuss the situation where the attosecond pulse trains coincides with a minimum/maximum crossing of the vector potential. Figure 7.5 ***e*** shows pronounced interference fringes at 90 degree with respect to the laser polarization. This result should be compared with Figure 7.3, where a pair of attosecond XUV pulses coincide with the zero crossings of the infrared laser field. Because of the limitation on the highest voltages that we can apply on the electrodes to accelerate electrons, the higher energy electrons that appear in the upmost and downmost region in Figure 7.2 (b) are not seen in Figure 7.5 ***e***. However, these electrons do exist and they are just out of our detector, because there is a significant momentum transfer from the laser field to the electron along the polarization axis. The highest electron energy at this time delay is about $25eV$.

Figure 7.7 shows the interference fringes observed at 90 degree for both the experimental results and the theoretical results. If the final wave function is symmetric with respect to the (p_x, p_z) plane, then according to Equation 7.13 the maxima of the interference fringes at 90 degrees should appear when $W = (2n+1)\hbar\omega$, where again we use $W = I_p + U_p + (\mathbf{p_x^2} + \mathbf{p_y^2})/2m$. If the final wave function is anti-symmetric, a dipole phase of π is introduced; then the interference criteria becomes $W = 2n\hbar\omega$.

Since Argon has three different initial states $3p, m = 0, \pm 1$, several final states with s or d symmetry are possible. Theoretical results for $m = 0$ and $m = 1$ are separately shown in Figure 7.7 ***b***. Since the $m = 0$ ground state of Argon is anti-symmetric with respect to the (p_x, p_z) plane, photoionization produces a continuum electron wavepacket that is symmetric with respect to this plane, while

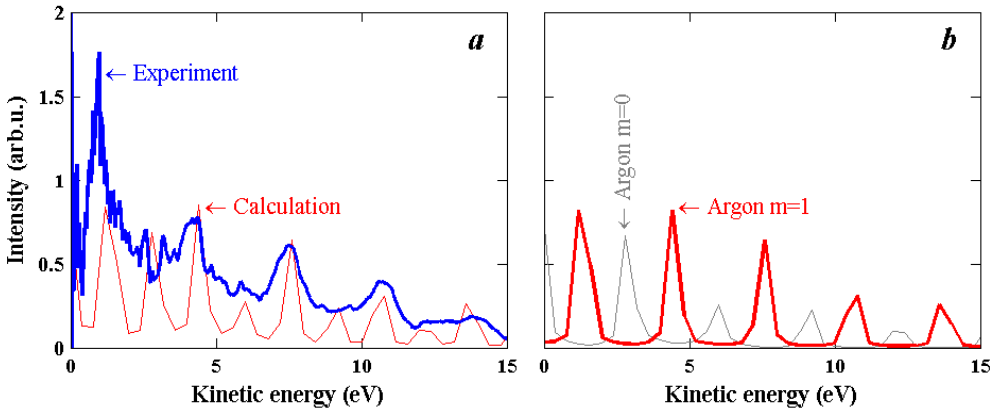

Figure 7.7: Interference fringes at 90 degrees when the attosecond pulses coincide with the maxima/minima of the vector potential of the infrared laser field. Figure ***a*** shows that the experimental observation(thick blue curve) compares well with theoretical prediction(thin red curve) obtained by assuming a small experimental temporal jitter (of $\pm 50as$). The fringe positions depend on the symmetry properties of the initial wave function with respect to the plane perpendicular to the laser polarization, as shown in Figure ***b*** for Argon $m = 0$(thin gray curve) and $m = \pm 1$(thick red curve) initial states.

for $m = 1$ the opposite applies. In our experiment, $U_p = \hbar\omega$, while $I_p \approx 10\hbar\omega$, so that the observed fringes appearing at odd multiples of the infrared photon energy fulfill the criteria $W = 2n\hbar\omega$. This tells us in the case investigated here, photoionization is dominated by the transition from the $m = \pm 1$ states in the direction perpendicular to the laser polarization axis.

7.4 Conclusion

We have successfully implemented an attosecond electron wavepacket interferometer. This technique allows us to retrieve phase information of the atomic wave function in momentum space. By examining the position of the fringes in a larger overlap region, the range of electron momenta where the phase of the electron wave function can be determined will be significantly extended. This can be done by changing the laser intensity, by varying the delay while taking into account the added accumulated phase due to the interaction with the infrared field, or alternatively by using different states of polarizations for the XUV and infrared light fields combined with a polarization-independent detection technique. The use of algorithms similar to those developed in the optical domain will enable re-

trieval of the phase of the wave functions in momentum space, and consequently in real space. This opens exciting possibilities for mapping out the ground state electronic wave functions of complex, chemically relevant molecules.

Appendix A

Projection of a 3D distribution onto a 2D surface

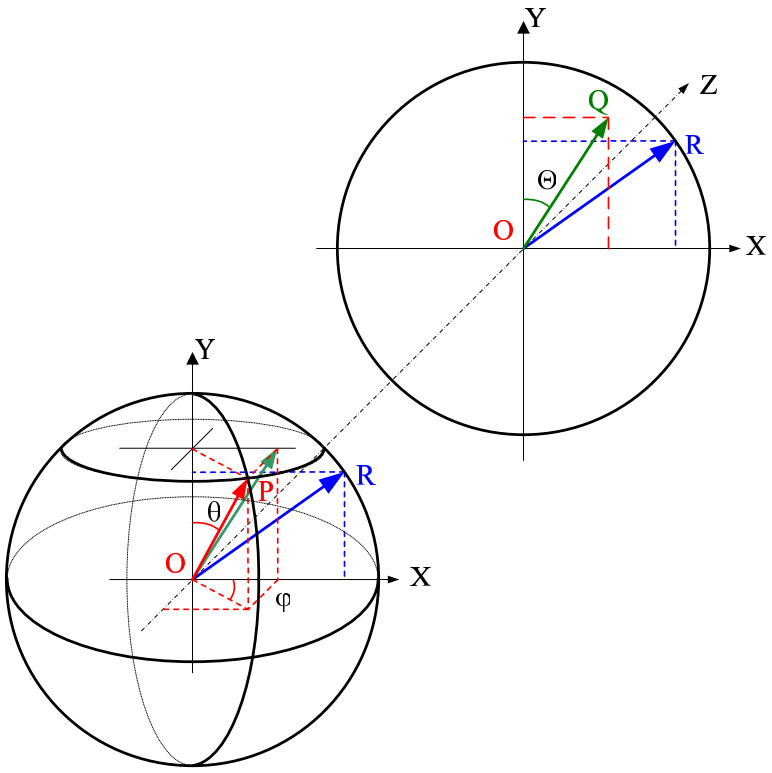

The coordinate systems are chosen such that the laser polarization is always parallel to the Y axis. A 3D distribution can be discribed as $f(x, y, z)$ in a cartesian coordinate system, or as $f(\rho, \theta, \varphi)$ in a spherical coordinate system. Its 2D projection can be discribed as $f(x, y)$ in a cartesian coordiante system, or as

$f(r, \Theta)$ in a polar coordinate system. In the figure shown above, $\overrightarrow{OQ}$ in the 2D plane is a projection of vector $\overrightarrow{OP}$ in 3D space. For reasons of consistency we choose a definiton in which the polar angle $\theta \in [0, \pi]$ or $\Theta \in [0, \pi]$ starts from the Y axis[1], and the azimuthal angle $\varphi \in [0, 2\pi)$ rotates around Y axis in XZ plane. In a spherical coordinate system, we have $x = \rho sin\theta cos\varphi,\ y = \rho cos\theta,\ z = \rho sin\theta sin\varphi$. The 3D distributions in cartesian and spherical coordinate systems are related as

$$\iiint f(x, y, z)dxdydz = \iiint f(\rho, \theta, \varphi)\rho^2 sin\theta d\rho d\theta d\varphi.$$

In a polar coordinate system, we have $x = rsin\Theta,\ y = rcos\Theta$, the 2D distributions in cartesian and polar coordinate systems are related as

$$\iint f(x, y)dxdy = \iint f(r, \Theta)\ rdrd\Theta.$$

[1]Note that in mathematics $\theta \in [0, 2\pi)$ is normally defined as the azimuthal angle around the Z axis in the XY plane, and $\varphi \in [0, \pi]$ is defined as polar angle from the Z axis.

Appendix B

Some physical constants

Quantity (1 a.u.)	Physical quantity	SI unit	Alternative
Length	Bohr radius a_0	$5.29 \times 10^{-11} m$	$0.529 \mathring{A}$
Mass	Electron rest mass m_e	$9.1 \times 10^{-31} kg$	
Charge	Elementary charge e	$1.6 \times 10^{-19} C$	
Angular momentum	Dirac constant $\hbar$	$1.0546 \times 10^{-34} Js$	
	Planck constant h	$6.626 \times 10^{-34} Js$	
Energy	Hartree energy E_h	$4.36 \times 10^{-18} J$	$27.2eV$
Time	$\frac{\hbar}{E_h}$	$2.42 \times 10^{-17} s$	$24.2as$
Velocity	$\frac{a_0 E_h}{\hbar}$	$2.1877 \times 10^{6} m/s$	
Electric field		$5.14 \times 10^{11} V/m$	

Energy =	$1eV$
	$1.6 \times 10^{-19} J$
	$8065.541 cm^{-1}$
	$1239.84nm$
	$2.418 \times 10^{14} Hz$
Wavenumber =	$1cm^{-1} = 100m^{-1}$
	$1.23984 \times 10^{-4} eV$
	$2.998 \times 10^{10} Hz$

Bibliography

[1] M. Protopapas, C. Keitel, and P. Knight, Rep. Prog. Phys. **60**, 389 (1997).

[2] J. Posthumus, Rep. Prog. Phys. **67**, 623 (2004).

[3] J. H. Eberly, J. Javanainen, and K. Rzazewski, Phys. Rep. **204**, 331 (1991).

[4] B. Sheehy and L. F. DiMauro, Annu. Rev. Phys. Chem. **47**, 463 (1996).

[5] T. Brabec and F. Krausz, Rev. Mod. Phys. **72**, 545 (2000).

[6] N. B. Delone and V. P. Krainov, *Multiphoton Processes in Atoms*, Springer-Verlag, 1994.

[7] G. Mainfray and C. Manus, Rep. Prog. Phys. **54**, 1333 (1991).

[8] P. Agostini, F. Fabre, G. Mainfray, and G. Petite, Phys. Rev. Lett. **42**, 1127 (1979).

[9] Y. Gontier and M. Trahin, J. Phys. B: At. Mol. Opt. Phys. **13**, 4383 (1980).

[10] L. V. Keldysh, Sov. Phys. JETP **20**, 1307 (1965).

[11] F. Faisal, J. Phys. B: At. Mol. Opt. Phys. **6**, L89 (1973).

[12] H. R. Reiss, Phys. Rev. A **22**, 1786 (1980).

[13] M. V. Ammosov, N. B. Delone, and V. P. Krainov, Sov. Phys. JETP **64**, 1191 (1986).

[14] S. Augst, D. D. Meyerhofer, D. Strickland, and S. L. Chin, J. Opt. Soc. Am. B **8**, 858 (1991).

[15] E. Mevel et al., Phys. Rev. Lett. **70**, 406 (1993).

[16] A. L'Huillier, P. Balcou, S. Candel, K. Schafer, and K. Kulander, Phys. Rev. A **46**, 2778 (1992).

[17] D. Fittinghoff, P. Bolton, B. Chang, and K. Kulander, Phys. Rev. Lett. **69**, 2642 (1992).

[18] B. Walker et al., Phys. Rev. Lett. **73**, 1227 (1994).

[19] T. Weber et al., Phys. Rev. Lett. **84**, 443 (2000).

[20] T. Weber et al., Nature **405**, 658 (2000).

[21] P. Corkum, Phys. Rev. Lett. **71**, 1994 (1993).

[22] K. C. Kulander, K. J. Schafer, and J. L. Krause, in *Super-intense laser-atom physics(SILAP III)*, edited by B. Piraux, volume 316, page 95, NATO, Plenum Press, New York, 1993.

[23] H. B. Van Linden van den Heuvell and H. G. Muller, in *Multiphoton Processes*, edited by S. J. Smith and P. L. Knight, page 25, Cambridge University Press, 1988.

[24] P. Kruit, J. Kimman, H. G. Muller, and M. J. van der Wiel, Phys. Rev. A **28**, 248 (1983).

[25] H. G. Muller, A. Tip, and M. J. van der Wiel, J. Phys. B: At. Mol. Opt. Phys. **16**, L679 (1983).

[26] R. R. Freeman et al., Phys. Rev. Lett. **59**, 1092 (1987).

[27] G. Paulus, W. Nicklich, H. Xu, P. Lambropoulos, and H. Walther, Phys. Rev. Lett. **72**, 2851 (1994).

[28] B. Yang et al., Phys. Rev. Lett. **71**, 3770 (1993).

[29] G. Paulus, W. Nicklich, and H. Walther, Eur. Phys. Lett. **27**, 267 (1994).

[30] G. Paulus, W. Becker, W. Nicklich, and H. Walther, J. Phys. B: At. Mol. Opt. Phys. **27**, L703 (1994).

[31] B. Walker et al., Phys. Rev. Lett. **77**, 203 (1996).

[32] P. Hansch, M. Walker, and L. VanWoerkom, Phys. Rev. A **55**, R2535 (1997).

[33] M. Hertlein, P. Bucksbaum, and H. Muller, J. Phys. B: At. Mol. Opt. Phys. **30**, L197 (1997).

[34] M. Nandor, M. Walker, L. Van Woerkom, and H. Muller, Phys. Rev. A **60**, R1771 (1999).

[35] H. Muller and F. Kooiman, Phys. Rev. Lett. **81**, 1207 (1998).

[36] H. Muller, Phys. Rev. Lett. **83**, 3158 (1999).

[37] H. Muller, Opt. Expr. **8**, 44 (2001).

[38] R. Kopold and W. Becker, J. Phys. B: At. Mol. Opt. Phys. **32**, L419 (1999).

[39] G. Paulus, F. Grasbon, and H. Walther, Physica Scripta **68**, C118 (2003).

[40] G. Paulus, F. Grasbon, and H. Walther, J. Mod. Opt. **50**, 343 (2003).

[41] F. Grasbon et al., Phys. Rev. Lett. **91**, 173003 (2003).

[42] P. Salieres, A. L'Huillier, and M. Lewenstein, Phys. Rev. Lett. **74**, 3776 (1995).

[43] P. Salieres, T. Ditmire, M. Perry, A. LHuillier, and M. Lewenstein, J. Phys. B: At. Mol. Opt. Phys. **29**, 4771 (1996).

[44] M. Bellini et al., Phys. Rev. Lett. **81**, 297 (1998).

[45] D. Descamps et al., Opt. Lett. **25**, 135 (2000).

[46] K. Lee, Y. Cha, M. Shin, B. Kim, and D. Kim, Phys. Rev. E **67**, 026502 (2003).

[47] Y. Tamaki, J. Itatani, M. Obara, and K. Midorikawa, Phys. Rev. A **6206**, 063802 (2000).

[48] S. Kazamias et al., Eur. Phys. J. D **21**, 353 (2002).

[49] M. Nisoli et al., Appl. Phys. B **74**, S11 (2002).

[50] C. Altucci et al., Phys. Rev. A **68**, 033806 (2003).

[51] J. Hergott et al., Phys. Rev. A **66**, 021801 (2002).

[52] E. Takahashi, Y. Nabekawa, and K. Midorikawa, Opt. Lett. **27**, 1920 (2002).

[53] E. Takahashi, Y. Nabekawa, T. Otsuka, M. Obara, and K. Midorikawa, Phys. Rev. A **66**, 021802 (2002).

[54] E. Seres, J. Seres, F. Krausz, and C. Spielmann, Phys. Rev. Lett. **92**, 163002 (2004).

[55] J. Seres et al., Nature **433**, 596 (2005).

[56] C. Durfee, S. Backus, H. Kapteyn, and M. Murnane, Opt. Lett. **24**, 697 (1999).

[57] A. Rundquist et al., Science **280**, 1412 (1998).

[58] R. Bartels et al., Science **297**, 376 (2002).

[59] A. Paul et al., Nature **421**, 51 (2003).

[60] E. Gibson et al., Science **302**, 95 (2003).

[61] S. Kazamias et al., Eur. Phys. J. D **26**, 47 (2003).

[62] E. Constant et al., Phys. Rev. Lett. **82**, 1668 (1999).

[63] R. Bartels et al., Nature **406**, 164 (2000).

[64] X. Chu and S. Chu, Phys. Rev. A **64**, 021403 (2001).

[65] I. Christov, J. Opt. Soc. Am. B **18**, 1877 (2001).

[66] D. Reitze et al., Opt. Lett. **29**, 86 (2004).

[67] B. Sheehy et al., Phys. Rev. Lett. **83**, 5270 (1999).

[68] B. Shan, A. Cavalieri, and Z. Chang, Appl. Phys. B **74**, S23 (2002).

[69] B. Shan and Z. Chang, Phys. Rev. A **65**, 011804 (2002).

[70] L. Nugent-Glandorf et al., Phys. Rev. Lett. **8719**, 193002 (2001).

[71] M. Wieland et al., Appl. Phys. Lett. **81**, 2520 (2002).

[72] B. Schenkel et al., Opt. Lett. **28**, 1987 (2003).

[73] G. Farkas and C. Toth, Phys. Lett. A **168**, 447 (1992).

[74] S. Harris, J. Macklin, and T. Hansch, Opt. Commun. **100**, 487 (1993).

[75] P. Antoine, A. L'Huillier, and M. Lewenstein, Phys. Rev. Lett. **77**, 1234 (1996).

[76] M. Gaarde et al., Phys. Rev. A **59**, 1367 (1999).

[77] C. Lynga et al., Phys. Rev. A **60**, 4823 (1999).

[78] D. Lee, J. Kim, K. Hong, and C. Nam, Phys. Rev. Lett. **8724**, 243902 (2001).

[79] M. Ivanov, P. Corkum, T. Zuo, and A. Bandrauk, Phys. Rev. Lett. **74**, 2933 (1995).

[80] P. Antoine et al., Phys. Rev. A **56**, 4960 (1997).

[81] D. Lappas and A. L'Huillier, Phys. Rev. A **58**, 4140 (1998).

[82] P. Antoine et al., Annales de Physique **22**, 45 (1997).

[83] O. Tcherbakoff, E. Mevel, D. Descamps, J. Plumridge, and E. Constant, Phys. Rev. A **68**, 043804 (2003).

[84] Z. Chang, Phys. Rev. A **70**, 043802 (2004).

[85] R. Lopez-Martens et al., Appl. Phys. B **78**, 835 (2004).

[86] K. Schafer and K. Kulander, Phys. Rev. Lett. **78**, 638 (1997).

[87] I. Christov, H. Kapteyn, and M. Murnane, Opt. Lett. **22**, 1882 (1997).

[88] M. Drescher et al., Science **291**, 1923 (2001).

[89] M. Hentschel et al., Nature **414**, 509 (2001).

[90] A. Baltuska et al., Nature **421**, 611 (2003).

[91] N. Papadogiannis, P. Loukakos, and S. Moustaizis, Opt. Commun. **166**, 133 (1999).

[92] P. Tzallas, D. Charalambidis, N. Papadogiannis, K. Witte, and G. Tsakiris, Nature **426**, 267 (2003).

[93] T. Sekikawa, A. Kosuge, T. Kanai, and S. Watanabe, Nature **432**, 605 (2004).

[94] H. Muller, Phys. Rev. A **65**, 055402 (2002).

[95] P. Paul et al., Science **292**, 1689 (2001).

[96] L. Dinu et al., Phys. Rev. Lett. **91**, 063901 (2003).

[97] Y. Mairesse et al., Science **302**, 1540 (2003).

[98] R. Lopez-Martens et al., Phys. Rev. Lett. **94**, 033001 (2005).

[99] J. Norin et al., Phys. Rev. Lett. **88**, 193901 (2002).

[100] T. Sekikawa, T. Kanai, and S. Watanabe, Phys. Rev. Lett. **91**, 103902 (2003).

[101] S. Aseyev, Y. Ni, L. Frasinski, H. Muller, and M. Vrakking, Phys. Rev. Lett. **91**, 223902 (2003).

[102] J. Itatani et al., Phys. Rev. Lett. **88**, 173903 (2002).

[103] R. Kienberger et al., Appl. Phys. B **74**, S3 (2002).

[104] F. Quere, J. Itatani, G. Yudin, and P. Corkum, Phys. Rev. Lett. **90**, 073902 (2003).

[105] J. Mauritsson, R. Lopez-Martens, and A. L'Huillier, Opt. Lett. **28**, 2393 (2003).

[106] E. Cormier et al., Phys. Rev. Lett. **94**, 033905 (2005).

[107] Y. Mairesse and F. Quere, Phys. Rev. A **71**, 011401 (2005).

[108] F. Quere, Y. Mairesse, and J. Itatani, J. Mod. Opt. **52**, 339 (2005).

[109] E. Goulielmakis et al., Science **305**, 1267 (2004).

[110] D. Strickland and G. Mourou, Opt. Commun. **56**, 219 (1985).

[111] M. Perry and G. Mourou, Science **264**, 917 (1994).

[112] J. A. Salehi, A. M. Weiner, and J. P. Heritage, J. Lightwave Technol. **8**, 478 (1990).

[113] X. Liu, D. Du, and G. Mourou, IEEE J. Quant. Electron. **33**, 1706 (1997).

[114] A. F. Fercher, W. Drexler, C. K. Hitzenberger, and T. Lasser, Rep. Prog. Phys. **66**, 239 (2003).

[115] S. Backus, C. Durfee, M. Murnane, and H. Kapteyn, Rev. Sci. Instr. **69**, 1207 (1998).

[116] F. Rosca-Pruna, *Alignment of diatomic molecules induced by intense laser fields*, PhD thesis, FOM-AMOLF, 2001.

[117] A. Öffner, U.S. patent , 3,748,015 (1971).

[118] M. Nisoli, S. DeSilvestri, and O. Svelto, Appl. Phys. Lett. **68**, 2793 (1996).

[119] J. Seres et al., Opt. Lett. **28**, 1832 (2003).

[120] C. Hauri et al., Appl. Phys. B **79**, 673 (2004).

[121] G. Paulus, F. Grasbon, H. Walther, R. Kopold, and W. Becker, Phys. Rev. A **64**, 021401 (2001).

[122] http://www.mpq.mpg.de.

[123] J. Reichert, R. Holzwarth, T. Udem, and T. Hansch, Opt. Commun. **172**, 59 (1999).

[124] S. Cundiff and J. Ye, J. Mod. Opt. **52**, 201 (2005).

[125] R. Trebino et al., Rev. Sci. Instr. **68**, 3277 (1997).

[126] C. Iaconis and I. Walmsley, Opt. Lett. **23**, 792 (1998).

[127] C. Iaconis and I. Walmsley, IEEE J. Quant. Electron. **35**, 501 (1999).

[128] L. Gallmann et al., Opt. Lett. **24**, 1314 (1999).

[129] A. Weiner, Rev. Sci. Instr. **71**, 1929 (2000).

[130] S. Zamith et al., Phys. Rev. A **70**, 011201 (2004).

[131] A. J. R. Heck and D. W. Chandler, Annu. Rev. Phys. Chem. **46**, 335 (1995).

[132] H. Helm, N. Bjerre, M. Dyer, D. Huestis, and M. Saeed, Phys. Rev. Lett. **70**, 3221 (1993).

[133] H. Helm and M. Dyer, Phys. Rev. A **49**, 2726 (1994).

[134] A. Eppink and D. Parker, Rev. Sci. Instr. **68**, 3477 (1997).

[135] M. Vrakking, Rev. Sci. Instr. **72**, 4084 (2001).

[136] E. Constant, H. Stapelfeldt, and P. Corkum, Phys. Rev. Lett. **76**, 4140 (1996).

[137] L. F. DiMauro and P. Agostini, *Ionization dynamics in strong laser fields*, volume 35, page 79, Academic Press, Inc., 1995.

[138] M. Lewenstein, P. Balcou, M. Ivanov, A. L'Huillier, and P. Corkum, Phys. Rev. A **49**, 2117 (1994).

[139] A. Baltuska et al., IEEE J. Sel. Top. Quant. Electron. **9**, 972 (2003).

[140] J. E. Bayfield and P. M. Koch, Phys. Rev. Lett. **33**, 258 (1974).

[141] T. F. Gallagher, *Rydberg atoms*, Cambridge university press, 1994.

[142] D. Kleppner, M. G. Littman, and M. L. Zimmerman, *Rydberg states of atoms and molecules*, chapter Rydberg atoms in strong fields, Cambridge University Press, 1983.

[143] A. Gürtler, F. Robicheaux, W. van der Zande, and L. Noordam, Phys. Rev. Lett. **92**, 033002 (2004).

[144] R. Lopez-Martens et al., Phys. Rev. A **69**, 053811 (2004).

[145] C. Siedschlag, H. G. Muller, and M. J. J. Vrakking, Laser Physics **15**, 916 (2005).

[146] J. Itatani, F. Quere, G. Yudin, and P. Corkum, Laser Physics **14**, 344 (2004).

[147] H. Niikura et al., Nature **417**, 917 (2002).

[148] H. Niikura, P. Corkum, and D. Villeneuve, Phys. Rev. Lett. **90**, 203601 (2003).

[149] S. Chelkowski, P. Corkum, and A. Bandrauk, Phys. Rev. Lett. **82**, 3416 (1999).

[150] http://www.rijnh.nl.

[151] V. Schyja, T. Lang, and H. Helm, Phys. Rev. A **57**, 3692 (1998).

[152] D. G. Arbo, S. Yoshida, E. Persson, K. I. Dimitriou, and J. Burgdorfer, arXiv:quant-ph , 0507131 (2005).

[153] F. Lindner et al., Phys. Rev. Lett. **95**, 040401 (2005).

[154] C. Nicole et al., Phys. Rev. Lett. **85**, 4024 (2000).

[155] C. Nicole, H. Offerhaus, M. Vrakking, F. Lepine, and C. Bordas, Phys. Rev. Lett. **88**, 133001 (2002).

[156] B. Walker et al., Phys. Rev. Lett. **73**, 1227 (1994).

[157] G. Paulus et al., Phys. Rev. Lett. **91**, 253004 (2003).

[158] M. Nandor, M. Walker, and L. Van Woerkom, J. Phys. B: At. Mol. Opt. Phys. **31**, 4617 (1998).

[159] W. Becker et al., *Adv. At. Mol. Phys.*, volume 48, pages 35–98, Academic Press, Inc., 2002.

[160] K. Schafer and D. Milosevic, Private communications (2005).

[161] V. Veniard, R. Taieb, and A. Maquet, Phys. Rev. A **54**, 721 (1996).

[162] R. Lopez-Martens, J. Mauritsson, A. Johansson, J. Norin, and A. L'Huillier, Eur. Phys. J. D **26**, 105 (2003).

[163] P. Lambropoulos, *Adv. At. Mol. Phys.*, volume 12, page 87, Academic Press, Inc., 1976.

[164] S. J. Smith and G. Leuchs, *Adv. At. Mol. Phys.*, volume 24, page 157, Academic Press, Inc., 1988.

[165] E. Toma and H. Muller, J. Phys. B: At. Mol. Opt. Phys. **35**, 3435 (2002).

[166] M. Gaarde and K. Schafer, Phys. Rev. Lett. **89**, 213901 (2002).

[167] W. J. Bates, Proc. Roy. Phys. Soc. **59**, 940 (1947).

[168] P. Johnsson et al., Phys. Rev. Lett. **95**, 013001 (2005).

Summary

This thesis describes selected experimental studies on the interaction of ultrashort electromagnetic pulses with atoms, particularly on strong field ionization of atoms and the generation of attosecond laser pulses. The thesis is divided into three parts.

The first part of this thesis, consisting of Chapter 1 and 2, is an introduction of the background physics and experimental tools.

Chapter 1 introduces the general physics of light-matter interactions, in particular, the interaction of ultrashort intense laser with atoms. An overview on the current status of the generation and characterization of attosecond laser pulses is also given in this chapter.

Chapter 2 introduces the principle of the generation, characterization and manipulation of ultrashort intense laser technology and a powerful velocity-map imaging setup which has been used to study the electron dynamics in many of the experiments discussed in this thesis.

The second part, consisting of Chapter 3, 4 and 5, is devoted to the study of ionization dynamics with different electromagnetic radiation sources, ranging from radio frequency fields and terahertz/far-infrared pulses to near-infrared laser pulses.

Chapter 3 discusses an experiment where Rydberg atoms in an external radio frequency field were used as a model system to study strong field ionization dynamics with sub-cycle time resolution. We demonstrated that the ionization dynamics can be dramatically influenced by manipulating the carrier-envelope phase of the ionizing pulses and by the use of two-color few-cycle pulses, both leading to a subtle reshaping of the field oscillation. Based on the understanding from this experiment, we also showed the possibility of creating isolated attosecond pulses from many-cycle driving pulses by an appropriate tuning of the two laser frequencies, which results in control of the ionization and the recollision dynamics of the electronic wavepacket.

Chapter 4 discusses above-threshold ionization of low-lying Xenon Rydberg states with far-infrared free electron laser pulses over a wide range of different

laser wavelengths, pulse durations and starting from different initial Rydberg states. This variation of the experimental parameters allows to perform measurements both in the tunnelling/over-the-barrier regime and in the multi-photon regime. For example, when moving towards longer wavelengths, the experiments move into the multi-photon regime due to the fast drop of the focused peak laser intensity that is wavelength dependent. The emission of the photoelectrons was observed to be preferentially aligned along the laser polarization axis when the free electron laser pulses were made as short and intense as possible. Furthermore, measurements over a series of initial s and d Rydberg states showed a consistent difference in the photoelectron angular distribution between s and d states. We also observed that electrons with very low kinetic energy may come back and rescatter off their parents ionic cores, leading to an extra peak in the photoelectron kinetic energy spectra. This experiment constitutes another model system for better understanding the mechanism of strong field ionization in the optical domain. The low (terahertz) frequencies of these laser pulses can (in the future) allow us to probe sub-cycle electron dynamics with readily available femtosecond laser pulses.

Chapter 5 discusses above-threshold ionization of atoms with carrier-envelope-phase-stabilized few-cycle laser pulses. With the help of a velocity-map imaging photoelectron spectrometer, we performed, for the first time, measurements of the full photoelectron angular distribution in the whole photoelectron kinetic energy range. The asymmetry along the laser polarization in the electron emission in above-threshold ionization of rare gas atoms can be used to measure the carrier-envelope phase. Because of the high collection efficiency, close to 100%, it may also allow a real-time single-shot measurement of the carrier-envelope phase. We also observed interference structures in above-threshold ionization in Xenon, Argon and Krypton, which can be explained by interference between electron wavepackets which are created in successive half-cycles of the laser field. In particular, we observed electrons emitted around 60^o and 30^o with respect to the laser polarization, that were not previously reported.

The third part, consisting of Chapter 6 and 7, describes experiments on the generation and characterization of a train of attosecond laser pulses, and its novel application in electron wave-packet interferometry.

Chapter 6 discusses experiments on the characterization of a train of attosecond laser pulses, using mixed-color (XUV+IR) atomic two-photon ionization and detection of the resulting photoelectrons with a velocity-map imaging detector. We demonstrated that the relative phases of different XUV frequency components obtained by means of high-order harmonic generation are not only encoded in the dependence of the photoelectron yield on the XUV-IR time delay, but

also in the angular distribution of the ejected photoelectrons, thus making our technique suitable for the detection of single attosecond laser pulses. A striking dependence of the timing of the attosecond XUV bursts on the harmonic generation gas was observed. XUV bursts appear earlier in Xenon than in Argon and Krypton. This can be attributed to the fact that high-order harmonic generation in Xenon occurs in the multi-photon ionization regime, while it occurs in the tunneling ionization regime in Argon and Krypton. Another possible explanation is the selection of the short or long trajectories that the recolliding electron wavepackets experienced during the ionization processes.

Chapter 7 discusses an attosecond electron wavepacket interferometric experiment, where Argon atoms were ionized by a sequence of attosecond XUV pulses in the presence of an infrared laser field that induces a momentum shear between consecutive electron wavepacket replicas. Through the momentum shear, electron wavepackets with different initial momenta were made to overlap and the resulting interferogram contains information on the variation of the phase of the electron wavefunction in momentum space, and consequently on that of the ground-state wave function. The use of algorithms similar to those developed in the optical domain will enable retrieval of the phase of the wave functions in momentum space, and consequently in real space. This opens exciting possibilities for mapping out the ground state electronic wave functions of complex, chemically relevant molecules.

Samenvatting

Dit proefschrijft beschrijft een aantal experimenten op het gebied van de interactie van ultrakorte electromagnetische pulsen met atomen, met name de ionisatie van atomen in sterke laservelden en de generatie van attoseconde laser pulsen. Het proefschrift bestaat uit drie onderdelen.

Het eerste deel van het proefschrift (hoofdstukken 1 en 2) zijn een algemene inleiding op de achterliggende fysica en de gebruikte experimentele methoden.

Hoofdstuk 1 bevat een algemene inleiding tot de interactie van licht met materie, met name de interactie van intense, ultrakorte laser pulsen met atomen. Een overzicht wordt tevens gegeven van de huidige status van de generatie en karakterisatie van attoseconde laser pulsen.

Hoofdstuk 2 introduceert de generatie, karakterisatie en manipulatie van intense, ultrakorte laser pulsen, alsmede de zogenaamde *velocity-map imaging* techniek, waarmee de drie-dimensionale snelheids verdeling van geioniseerde electronen bepaald kan worden. In de meeste experimenten in dit proefschrift is gebruik gemaakt van deze methode om inzicht te krijgen in de dynamica van de electronen.

Het tweede deel van het proefschrift (hoofdstukken 3 tot 5) is gewijd aan een studie van ionisatie dynamica in verschillende golflengte gebieden. Hierbij is gebruik gemaakt van radio-frequente (RF) straling, Terahertz/ver-infrarode straling en nabij-infrarode laser pulsen.

Hoofdstuk 3 beschrijft experimenten waarbij de ionisatie van Rydberg atomen in een radio-frequent veld gebruikt worden als model systeem om ionisatie in een sterk oscillarend electrisch veld met sub-optische cyclus tijds-resolutie te bestuderen. Er wordt aangetoond dat de ionisatie dynamica sterk afhangt van de zogenaamde *carrier-envelope phase* van de pulsen. Voorts worden experimenten beschreven waar de ionisatie geschied door middel van een twee-kleuren veld, waarbij de ionisatie dynamica beinvloed wordt door subtiele wijzigingen in de vorm van de oscillaties van het electrisch veld. Op basis van het begrip dat in deze experimenten verkregen werd, is vervolgens aangetoond dat een twee-kleuren laser veld bestaande uit vele optische perioden gebruikt kan worden om de gen-

eratie van één geisoleerde attoseconde puls te bewerkstelligen. Hierbij beinvloedt het gebruik van een twee-kleuren laser veld zowel de ionisatie dynamica als de dynamica van de electron-ion botsing gedurende welke de attoseconde puls gevormd wordt.

Hoofdstuk 4 beschrijft experimenten waarbij laag-liggende Xenon Rydberg atomen geioniseerd worden met behulp van een breed verstembare ver-infrarode vrije electronen laser, waarvan tevens de pulsduur en de intensiteit gevarieerd worden. Afhankelijk van de experimentele parameters, begeeft dit experiment zich in het zogenaamde *multi-foton* regime of het *tunnelling* regime, waarin de ionisatie voornamelijk bepaald wordt door de frequentie respectievelijk amplitude van de optische pulsen. De gevormde foto-electronen zijn sterk gepiekt langs de polarisatie-as van de laser, met name bij de ionisatie van Xe atomen in een *s*-orbitaal met korte laser pulsen met een korte golflengte. De fotoelectron hoekverdelingen verschillen sterk voor Xe atomen die zich aanvankelijk in een *s*- respectievelijk *d*-orbitaal bevinden. Verder is waargenomen dat electronen die ioniseren met een kleine kinetische energie een botsing met het Xe^+ ion kunnen ondergaan, die aanleiding geeft tot een separate ring in de gemeten experimentele snelheidsverdelingen. Net als hoofdstuk 3 maken de in dit hoofdstuk gepresenteerde experimenten een beter begrip van ionisatie processen in het optische domein mogelijk. In de toekomst kan gepoogd worden om de electron dynamica binnen de optische cyclus van de THz straling te bestuderen met behulp van een femtoseconde laser.

Hoofdstuk 5 beschrijft experimenten aan de ionisatie van atomen met ultrakorte laser pulsen bestaande uit slechts enkele optische perioden, waarvan bovendien de *carrier-envelope phase* constant is. Met behulp van een *velocity-map imaging* spectrometer is de drie-dimensionale snelheidsverdeling van de uitgeworpen electronen gemeten. De asymmetry in deze verdeling langs de polarisatie richting van de laser kan gebruikt worden om de *carrier-envelope phase* te bepalen. Op basis van de hoge collectie efficienctie van de electronen (nabij 100%) is het wellicht mogelijk om deze bepaling te doen voor individuele laser pulsen. Voorts zijn experimenten verricht aan de ionisatie van Xenon, Krypton en Argon atomen, waarin interferentie structuren zijn waargenomen, die veroorzaakt worden door het feit dat de ionisatie twee keer per optische cyclus plaatsvindt. Electron emissie is waargenomen bij hoeken van 60^o en 30^o ten opzichte van de polarisatie as. Deze structuren worden tentatief toegeschreven aan interferentie tussen electron golf pakketten en botsingen van de electronen met het ion.

Het derde deel van het proefschrift (hoofdstukken 6 en 7) beschrijft experimenten aan de generatie en karakterisatie van een trein van attoseconde laser pulsen, alsmede hun gebruik in een nieuw interferometrisch experiment.

Hoofdstuk 6 beschrijft experimenten waarin een trein van attoseconde laser pulsen gekarakteriseerd wordt via twee-kleuren (XUV+IR) atomaire fotoionisatie en de detectie van de resulterende fotoelectronen met behulp van een *velocity-map imaging* spectrometer. Er wordt aangetoond dat de relatieve fase van de XUV frequentie componenten (die gegenereerd worden via hoge harmonische generatie) niet alleen verkregen kunnen worden uit de fotoelectronen opbrengst als functie van de vertraging tussen de XUV en IR bundel, maar tevens uit de hoekverdeling van de electronen. Dit betekent dat de methode geschikt is voor de detectie van geisoleerde attoseconde pulsen. Een opvallende afhankelijkheid van het moment van de attoseconde puls emissie ten aanzien van het gebruikte gas is waargenomen. Attoseconde pulsen worden in Xenon op een ander tijdstip binnen de optische cyclus van de nabij-infrarode laser gevormd, dan in het geval van Krypton en Argon. Een mogelijke verklaring is dat in het geval van Xenon de harmonische generatie geschiedt in het *multi-foton* regime, terwijl deze in geval van Krypton en Argon in het zogenaamde *tunnelling* regime plaatsvindt.

Hoofdstuk 7 beschrijft een experiment waarin Argon atomen worden geioniseerd door een combinatie van een attoseconde puls trein en een sterk infrarood laser veld, dat de snelheid van de electronen na ionisatie beinvloedt. Een interferentie is waargenomen tussen electron golfpakketten die door opeenvolgende attoseconde pulsen worden uitgezonden, en die onder invloed van het infrarode laser veld een tegenovergestelde snelheidsverschuiving ondergaan. Het resulterende interferogram bevat informatie over de fase van de continuum electronische golffunctie (in de momentum representatie) en dientengevolge over de golffunctie van het atoom in de grondtoestand. Gebruikmakend van algorithmen die vergelijkbaar zijn met de algorithmen die gebruikt worden voor de interferometrische karakterisatie van optische pulsen biedt dit perspectieven voor de bepaling van golffuncties van complexe, chemisch relevante moleculen.

Acknowledgements

This thesis not only represents my participation in all the experiments discussed, but also reflects the contributions from many others. Now it is the time to express my gratitude to those who have made this thesis possible.

First I would like to thank my supervisor, Prof. Marc J.J. Vrakking, a great hard-working scientist who always has great new ideas. Thanks for taking me, an engineering student, to his fundamental physics research group. Thanks for giving me the great chance to work in the frontier field of attosecond laser physics. Thanks for instructing me through all the steps in my study. I have benefited a lot and will still benefit in the future of my life from his enthusiastic, optimistic and critical view to both research and life.

I would also like to thank Prof. Guoguang Yang from the department of optical engineering of Zhejiang University for encouraging me in the very beginning to study abroad and Prof. Kejiang Zhou from the same department for sharing his life experience with me through the years.

I was very lucky to have been working with very talented members in the XUV physics group. Dr. Sergey Aseyev patiently taught me physics and guided me in the lab during my first year at AMOLF. He was willing to answer all my silly questions. Dr. Sebastien Zamith and Dr. Franck Lépine showed me how hard French could work, and helped me a lot in various experiments through the years. Dr. Christian Siedschlag, the theoretician in our group, always answered my simple theoretical questions in a even simpler and clear way. I also learned from Dr. Matthias Kling how persistent a good scientist should be. Fellow PhD students in the XUV physics group: Tatiana Martchenko, Jafar Khan and Omair Ghafur not only helped in the lab but also shared many cheerful and upset moments both in and outside the lab.

People from other AMOLF groups also helped in different ways. Prof. Harm-Geert Muller was willing to discuss about my very preliminary experimental findings and to answer my small technical questions. Dr. Andreas Gürtler generously shared with me not only his experimental setup and code for Rydberg atoms but also his experience as a PhD student. Dr. Anouk Wetzels shared her dye laser

at FELIX. The technicians at AMOLF are the greatest I've ever seen. They can easily transform a simple description into a fancy device which is exactly what we need in the experiment. It seems they never learned to say NO. I would like to thank Rob Kemper, Hinco Schoenmaker, Ad de Snaijer, and Anton Buijserd for their daily help on all the lab facilities. Especially I would like to thank Rob and Ad for driving me and our experimental setup by a truck to and back from Lund, the journey was fantastic! All other AMOLFers, from reception desk, personnel office, library to electronics department, have made AMOLF a really comfortable place to work. Bedankt!

During the four years in the XUV physics group, I had the privilege to work with many other great scientists from other institutions in different countries. Dr. Giel Berden from the FOM Institute for Plasma Physics helped not only operating the free electron lasers but also arranging nice dinners for us for the many late nights. I have been working with and learned a lot from Prof. Pierre Agostini from the French Atomic Energy Commission in Saclay when he was the Joop Los research fellow in our group for a period of half year. I would also like to thank Dr. Bertrand Carré and Dr. Pascal Salieres from the French Atomic Energy commission in Saclay for hosting me for the two-photon XUV ionization experiment. Thanks also go to Prof. Mauro Nisoli from Politecnico de Milano for hosting me to learn their hollow-core fiber compression technique and Prof. Howard Reiss and Dr. Wilhelm Becker for inviting me to visit the Max-Born Institute in Berlin. I also enjoyed working with Dr. Igor Yu. Kiyan, Boris Bergues and Dr. Zunaira Ansari from Freiburg University, thank you for your hospitality and the many nights we spent together in the lab. The movie nights and music nights in the physics department building were really unique, without these all the long nights in the lab would not be possible. Working in Prof. Anne L'Huillier's group at Lund Institute of Technology was also a great successful experience. The many late nights in the lab with Dr. Katalin Varjú, Per Johnson, Thomas Remetter, Eric Gustafson and Dr. Rodrigo López-Martens turned out to be very productive. Again, this would not be possible without the dinners that we had in the mysterious French restaurant in the city center. I would like to express my special thanks to Boris for lending me his ski suit and Katalin and Eric for teaching me ski during the attosecond and high-field physics conference in Obergurgl. Aart-Jan Verhoef from Prof. Ferenc Krausz's group at Max-Planck Institute for Quantum Optics helped a lot in operating the carrier-envelope phase stabilized high power $6fs$ laser system. Thank you all!

The environment created by the Chinese friends in Amsterdam has reduced my homesickness to the minimum and led to a joyful experience. It is hard to imagine the life without them. They are, to mention a few of them, Dr. Wenbing

Hu, Dr. Liangbin Li, Dr. Xinhua Guo, and Dr. Zunjing Wang from AMOLF and their families, Yuting Bai from NIKHEF, Dr. Jun Pang and Dr. Yingwei Zhan from CWI and their families, Dr. Zhisheng Huang, Dr. Wenhua Wu from VU and their families, Dr. Zhiming Zhao, Dr. Xulin Jiang and Dr. Lian Zhang from UvA and their families, Ting Li and Hailiang Mei, Ka Fai Lee and his family and many others.

My parents deserve my highest respect and deepest gratitude for their constant support and encouragement in all the steps that I have taken over the years. My gratitudes also go to my younger sister Yongmei and her husband for taking care of our parents.

Finally I would like to thank my wife Qun for her endless love and accompaniment.

About the author

The author was born in 10 November 1976, but documentarily in 15 July 1976, in Jingjiang, Jiangsu province, China. He was raised in a small village nearby the Yangtze river. He attended both primary (1982∼1987) and secondary school (1987∼1993) in the same village. From September 1993 to June 1997, he studied in the department of optical-electric and scientific instrument engineering at Zhejiang University in Hangzhou, Zhejiang province. He obtained his bachelor degree in engineering with a specialty in optical technology and photoelectric instrument in 1997. His undergraduate thesis was on the digital signal processing of fiber-optical gyroscope. Exempted from national graduate school entrance examination, he continued his study and research in a combined master-doctoral program in the same department, which was by then renamed to department of optical engineering. From August 1998 to August 1999, he was a visiting student in the ultrafast optics group at the central research laboratory of Hamamatsu Photonics K.K. in Japan, where he started to learn about femtosecond laser systems and ultrafast optical science. In 2001, after a long time serious consideration, he decided to quit his study in optical engineering from Zhejiang University. And from December 2001 to December 2005, he worked as a PhD student in the XUV physics group at the FOM Institute for Atomic and Molecular Physics in Amsterdam, the Netherlands. His main research topics during this period were attosecond laser pulses and strong field laser physics. Since January 2006, he has been working as a research scientist in the biomedical photonics group at Philips Research Laboratories in Eindhoven.